

Copyright Undertaking

This thesis is protected by copyright, with all rights reserved.

By reading and using the thesis, the reader understands and agrees to the following terms:

1. The reader will abide by the rules and legal ordinances governing copyright regarding the use of the thesis.
2. The reader will use the thesis for the purpose of research or private study only and not for distribution or further reproduction or any other purpose.
3. The reader agrees to indemnify and hold the University harmless from and against any loss, damage, cost, liability or expenses arising from copyright infringement or unauthorized usage.

If you have reasons to believe that any materials in this thesis are deemed not suitable to be distributed in this form, or a copyright owner having difficulty with the material being included in our database, please contact lbsys@polyu.edu.hk providing details. The Library will look into your claim and consider taking remedial action upon receipt of the written requests.

STRUCTURE AND ELECTROCHROMIC PROPERTIES OF TUNGSTEN OXIDE FILMS

AARON H.Y. WONG

M. PHIL.

THE HONG KONG POLYTECHNIC UNIVERSITY

2000



Pao Yue-Kong Library
PolyU • Hong Kong

STRUCTURE AND ELECTROCHROMIC
PROPERTIES OF TUNGSTEN OXIDE FILMS

BY
AARON H.Y. WONG

A THESIS SUBMITTED FOR THE DEGREE
OF MASTER OF PHILOSOPHY IN PHYSICS

THE HONG KONG POLYTECHNIC UNIVERSITY

AUGUST 1999

Acknowledgments

I would like to acknowledge Dr. C.W. Ong, my chief supervisor, for his invaluable advice and his close supervision in my study period. I would also like to thank Dr. K.F. Chan and Mr. Martin N.M. Ng, for their experience sharing and supporting.

I am grateful to thank Dr. Raymund W.M. Kwok and Dr. K.W. Wong of the Chinese University of Hong Kong for his assist in performing the XPS analyses, Dr. Geoffery K.H. Pang of the Department of Applied Physics of HKPU for his assist in operating the atomic-force-microscope and Dr. F.T. Cheng and Miss Manliza W.M. Chan for their generosity for sharing the use and experience of the instruments for electrochemical measurements. Thanks are also due to Mr. K.C. Lam for preparing part of the samples using thermal evaporation and the help in setting up the electrochromic measurement system, and Varitronix Limited and Dr. Y.K. Fung of Varitronix Limited for providing ITO coated glass substrates.

I would like to extend my special thanks to all technical staff of the Department of Applied Physics for their technical support.

This study was financially supported by the Hong Kong Polytechnic University under Code Nos. G-V 546.

Abstract

The aim of this project is to investigate the composition, structure, mechanical and electrochromic properties, and their correlations of tungsten oxide (WO_3) films deposited by magnetron sputtering and thermal evaporation at various conditions.

Tungsten oxide films with a broad spectrum of structures, ranging from porous, amorphous and polycrystalline states were fabricated using the two techniques. For thermally evaporated films deposited at high oxygen partial pressure (P_{O_2}), the film structure is amorphous and highly porous (40% porosity). The density is as low as 4.5 g cm^{-3} which is just 60% of that of the crystalline WO_3 . The oxygen-to-tungsten ratio is close to three. This indicates that the atoms in the films are arranged to form a porous of WO_3 -like network. When P_{O_2} drops, the film structure becomes less porous, and the density rises to 6.9 g cm^{-3} .

For magnetron-sputtered samples, the deposition process proceeded in atomic scale, so that the film was less porous and the density is high. Without any substrate heating, the film density was drastically risen to 7.7 g cm^{-3} . Under the observation of atomic force microscope, the topological image of the film surface was found to be smoother compared to the thermally evaporated film. When substrate temperature was further increased to 300°C , X-ray diffraction data showed that the film starts to crystallize, and the grain size grew with increasing substrate temperature.

With the structure change mentioned above, it was found that after 10000 coloring/bleaching cycles, the magnetron-sputtered film worked very well. However, the electrochromic properties of the thermally evaporated film degraded quickly after 1000 cycles. The coloration efficiency of the former was at least two times larger than that of the later. Since the structure of the thermally evaporated sample contained more pores, such that it was less stable under the actions of intercalation and deintercalation of ions. As a result, that the durability of the performance of electrochromism of the thermally evaporated film was inferior to that of magnetron sputtered film.

Associated with the structural change, the hardness of the thermally evaporated film deposited at P_{O_2} of 10 mTorr is as low as 0.96 GPa. When P_{O_2} decreases to the high vacuum background pressure, the hardness rises to 2.94 GPa, where the film structure still remains to be amorphous, but contains fewer pores. For the sputtered film on unheated substrate with no crystallization, a great portion of defects are removed, and the hardness finally reaches 5.57 GPa. For further increase in substrate temperature, the film is crystallized. However, the crystallized structure does not contribute to the hardness of the film.

Another important finding is that ion sputtering in XPS depth profile analysis leads to preferential sputtering of oxygen from tungsten oxide films. This effect alters the original film composition, such that the O/W ratio drops significantly. Meanwhile, due to the knocking out of oxygen atoms the W^V , W^{IV} , W^{III} , W^{II} states and metallic tungsten state appear in the W 4f photoelectron spectrum. Results of angle-resolved (45° and normal) XPS analysis also show that after experiencing ion

irradiation the oxygen content near the sputtered surface is small, further supporting the conjecture that some oxygen is preferentially sputtered by the ion beam.

Table of Contents

	Page
Acknowledgments	i
Abstract	ii
Table of Contents	v
List of Tables	viii
List of Figures	x
Chapter 1 Introduction	1
1.1 Literature Review	1
<i>1.1.1 Crystal Structures of Tungsten Oxide and Ion Intercalated Tungsten Oxide</i>	<i>1</i>
<i>1.1.2 Electrochromism</i>	<i>2</i>
<i>1.1.3 Fabrication of Tungsten Oxide Films</i>	<i>3</i>
<i>1.1.4 Applications and Developments</i>	<i>5</i>
1.2 Scope of Study	8
Chapter 2 Sample Preparation	10
2.1 Reactive Magnetron Sputtering	10
2.2 Reactive Thermal Evaporation	12
2.3 Preparation Conditions	13
Chapter 3 Sample Characterization	15
3.1 Thickness Measurements	16
3.2 X-ray Photoelectron Spectroscopy	17
3.3 Fourier Transform Infrared Absorption Spectroscopy	20

3.4 X-ray Diffraction	21
3.5 Cyclic Voltammetry	23
3.6 Optical Transmission Measurements	25
3.7 Nanoindentation Measurements	26
Chapter 4 Composition Analysis by X-ray Photoelectron Spectroscopy	31
4.1 Effects of Oxygen-to-Argon Ratio on the Composition of Magnetron-Sputtered Films	32
4.2 Effects of Substrate Temperature on the Composition of Magnetron-Sputtered Films	38
4.3 Effects of Oxygen Partial Pressure on the Composition of Thermally Evaporated Films	43
4.4 XPS Analysis of WO₃ Films after Coloring/Bleaching Cycles	49
4.5 Preferential Sputtering of Oxygen by Ion Irradiation	58
<i>4.5.1 Effects of Ion Bombardment on Magnetron-Sputtered Films on Unheated Substrate</i>	<i>58</i>
<i>4.5.2 Effects of Ion Bombardment on Magnetron-Sputtered Films on Heated Substrate</i>	<i>62</i>
<i>4.5.3 Effects of Ion Bombardment on Thermally Evaporated Film on Unheated Substrate</i>	<i>64</i>
<i>4.5.4 Profiles of W, O and O/W Ratio with Increasing Sputtering Time</i>	<i>66</i>
<i>4.5.5 Angle-resolved XPS Analysis</i>	<i>69</i>
Chapter 5 Structural Analysis	70
5.1 Infrared Absorption Spectroscopy	70
<i>5.1.1 Effects of Oxygen-to-Argon Flow Ratio on the Structure of Magnetron-Sputtered Films</i>	<i>70</i>
<i>5.1.2 Effects of Substrate Temperature on the Structure of Magnetron-Sputtered Films</i>	<i>74</i>

5.1.3 <i>Effect of Oxygen Partial Pressure on the Structure of Thermally Evaporated Films</i>	76
5.2 X-ray Diffraction	78
Chapter 6 Electrochromic and Mechanical Properties	83
6.1 Electrochromic Properties	82
6.2 Mechanical Properties	92
6.2.1 <i>Mechanical Properties of Magnetron-Sputtered Tungsten Oxide Films</i>	92
6.2.2 <i>Mechanical Properties of Thermally Evaporated Tungsten Oxide Films</i>	102
Chapter 7 Conclusions	106
Publications	109
References	110

List of Tables

	Page
Table 2.1 Summary of the preparation parameters of the tungsten oxide film deposited by reactive dc magnetron sputtering.	14
Table 2.2 Summary of the preparation parameters of the tungsten oxide films deposited by reactive thermal evaporation.	14
Table 3.1 The XPS sensitivity factors of tungsten (W), oxygen (O), carbon (C), lithium (Li) and chlorine (Cl).	18
Table 3.2 The maximum loads used for the nanoindentation experiments.	30
Table 4.1(a) The fraction, peak energy and FWHM of W ¹ , W ² and W ³ components of the W 4f spectra; O ¹ and O ² components of the O 1s spectra; and C ¹ component of the C 1s spectra of the tungsten oxide films sputtered on unheated substrate at various R_p .	36
Table 4.1(b) The O/W ratio in the films made by magnetron sputtering at various R_p .	36
Table 4.2(a) The fraction, peak energy and FWHM of W ¹ and W ² components of the W 4f spectra; O ¹ and O ² components of the O 1s spectra; and C ¹ component of the C 1s spectra of the films deposited by magnetron sputtering at various T_s .	41
Table 4.2(b) The O/W ratio in the films deposited by magnetron sputtering at various T_s .	41
Table 4.3(a) The fractions, peak energies and FWHM of W ¹ and W ² components of W 4f spectra; O ¹ and O ² components of the O 1s spectra; and C ¹ component of the C 1s spectra of the films made by thermal evaporation at various O ₂ partial pressures.	47
Table 4.3(b) The O/W ratio of the films made by thermal evaporation at various O ₂ partial pressures.	47
Table 4.4 The fractions, peak energies and FWHM of W ¹ and W ² components of W 4f spectra; O ¹ , O ² and O ³ components of the O 1s spectra; C ¹ and C ² component of the C 1s spectra; Li ¹ components of Li 1s spectra; and Cl ¹ and Cl ² components of Cl 2p spectra of the magnetron sputtered films undergone various c/b cycles.	52

Table. 4.5	Atomic concentration of tungsten associated with the W ¹ , W ² , W ³ and W ⁴ components, and the oxygen atoms associated with the O ¹ and O ² components for the magnetron-sputtered tungsten oxide films deposited on unheated substrate at $R_f = 2$.	60
Table 4.6	Atomic concentration of tungsten atoms associated with the W ¹ , W ² , W ³ and W ⁴ components, and the oxygen atoms associated with the O ¹ and O ² components for the magnetron-sputtered tungsten oxide films deposited at $R_f = 2$ and $T_s = 500$ °C.	62
Table 4.7	Atomic concentration of tungsten atoms associated with the W ¹ , W ² , W ³ and W ⁴ components, and the oxygen atoms associated with the O ¹ and O ² components for the thermally evaporated tungsten oxide films deposited on unheated substrate at oxygen partial pressure = 6 mTorr.	64
Table 4.8	O/W ratio of tungsten oxide film obtained by angle-resolved XPS analysis.	69
Table 5.1	Summary of the IR peak positions of tungsten oxide films deposited by magnetron sputtering and thermal evaporation.	73
Table 5.2	Summary of the peak positions observed in the IR and Raman spectra of tungsten oxide film [1. Azen et al. 1995, 2. Salje 1975, 3. Shigesato 1988, 4. Yoshiike and Kondo 1983]. Some corresponding assignments are labeled.	73
Table 6.1	Parameters used in the cyclic voltammetry experiments for the magnetron-sputtered and thermally evaporated tungsten oxide films.	84
Table 6.2	Hardness and elastic modulus of samples made by reactive magnetron sputtering.	92
Table 6.3	Hardness and elastic modulus of samples made by thermal evaporation.	103

List of Figures

		Page
Fig. 1.1	Schematic illustration of a corner-sharing and edge-sharing arrangement of octahedra in a tungsten oxide crystal [Granqvist 1995]. ● Tungsten atoms • Oxygen atoms	1
Fig. 1.2	Schematic diagram of an electrochromic light modulator in transmittance mode (with a transparent counter electrode), indicating transport of positive ions, Li^+ , under the action of an electric field.	7
Fig. 2.1	Schematic diagram of the magnetron sputtering chamber (Front view).	11
Fig. 2.2	Schematic diagram of the thermal evaporation chamber (Front view).	13
Fig. 3.1	Thickness measurement by an α -step profiler.	16
Fig. 3.2	The schematic diagram of an XPS system.	19
Fig. 3.3	Schematic diagram of an IR absorption experiment.	20
Fig. 3.4	Schematic diagram of 2θ scanning mode of XRD experiment.	22
Fig. 3.5	Schematic presentation of the experimental setup for the measurement of electrochromic properties of the film, at $\lambda = 632.8 \text{ nm}$.	23
Fig. 3.6	A typical pattern of loading/unloading curves of a nanoindentation.	27
Fig. 3.7	Deformation generated during indentation. r is the radius of the contact circle [Oliver and Pharr 1992].	29
Fig. 4.1	XPS spectra of W 4f and O 1s photoelectrons of magnetron-sputtered tungsten oxide films deposited at R_f (a) 2, (b) 1.75 and (c) 1.36.	35
Fig. 4.2	The atomic % of W^1 , W^2 and W^3 components of the W 4f spectra; O^1 and O^2 components of the O 1s spectra; and C^1 component of the C 1s spectra of the tungsten oxide films sputtered on unheated substrate at various R_f .	37

Fig. 4.3	XPS spectra of W 4f and O 1s photoelectrons of magnetron-sputtered tungsten oxide films deposited at fixed $R_f = 2$, and various T_s , (a) 500 °C, (b) 300 °C and (c) 110 °C.	40
Fig. 4.4	The atomic % of W ¹ and W ² components of the W 4f spectra; O ¹ and O ² components of the O 1s spectra; and C ¹ component of the C 1s spectra of the films deposited by magnetron sputtering at various T_s .	42
Fig. 4.5	XPS spectra of W 4f and O 1s photoelectrons of thermally evaporated tungsten oxide films deposited on unheated substrates at various oxygen partial pressures: (a) Background pressure of 2×10^{-6} Torr, (b) 0.4, (c) 4, (d) 6 and (e) 10 mTorr.	45-46
Fig. 4.6	The atomic % of W ¹ and W ² components of W 4f spectra; O ¹ and O ² components of the O 1s spectra; and C ¹ component of the C 1s spectra of the films made by thermal evaporation at various O ₂ partial pressures.	48
Fig. 4.7	XPS spectra of W 4f and O1s photoelectrons of magnetron-sputtered samples experienced in various times of c/b cycles (a) MS11, before experiencing c/b process, (b) MSC1, experienced 1000 times c/b cycles, (c) MSC2, experienced 10000 times c/b cycles.	51
Fig. 4.8(a)	The measured W (■), O (●), C (▼), Li (▲) and Cl (◆) concentration as functions of sputtering time for sample MS11, before experiencing c/b cycles.	55
Fig. 4.8(b)	The measured W (■), O (●), C (▼), Li (▲) and Cl (◆) concentration as functions of sputtering time for sample MSC1, after experiencing 1000 c/b cycles.	56
Fig. 4.8(c)	The measured W (■), O (●), C (▼), Li (▲) and Cl (◆) concentration as functions of sputtering time for sample MSC2, after experiencing 10000 c/b cycles.	57
Fig. 4.9	The W 4f and O 1s photoelectron spectra of magnetron-sputtered tungsten oxide film deposited on unheated substrate at $R_f = 2$. (a) Before surface cleaning, (b) After surface cleaning by 200 eV Ar ⁺ ions for 10 minutes, (c) After surface cleaning by 2k eV Ar ⁺ ions for 30 minutes.	61
Fig. 4.10	The W 4f and O 1s photoelectron spectra of magnetron-sputtered tungsten oxide film deposited at $T_s = 500$ °C and at $R_f = 2$. (a) Before surface cleaning, (b) After surface cleaning by 200 eV Ar ⁺ ions for 10 minutes, (c) After surface cleaning by 2k eV Ar ⁺ ions for 30 minutes.	63

Fig. 4.11	The W 4f and O 1s photoelectron spectra of thermally evaporated tungsten oxide film deposited on unheated substrate at oxygen partial pressure = 6 mTorr. (a) Before surface cleaning, (b) After surface cleaning by 200 eV Ar ⁺ ions for 10 minutes, (c) After surface cleaning by 2k eV Ar ⁺ ions for 30 minutes.	65
Fig. 4.12	The atomic concentration of O and W concentration as functions of sputtering time. Inset: O to W ratio. ▲ Magnetron-sputtered tungsten oxide films deposited on unheated substrate at $R_f = 2$, as deposited. ▼ Magnetron-sputtered tungsten oxide films deposited on unheated substrate at $R_f = 2$, after experienced 1000 c/b cycles. ■ Magnetron-sputtered tungsten oxide films deposited on unheated substrate at $R_f = 2$, after experienced 10000 c/b cycles. ● Magnetron-sputtered tungsten oxide films deposited at $R_f = 2$ and $T_s = 500$ °C. ◆ Thermally evaporated tungsten oxide films deposited on unheated substrate at oxygen partial pressure = 6 mTorr	68
Fig. 5.1	FTIR spectra of the tungsten oxide films deposited by magnetron sputtering at various R_f .	72
Fig. 5.2	FTIR spectra of the tungsten oxide films deposited by magnetron sputtering at various T_s .	75
Fig. 5.3	FTIR spectra of the tungsten oxide films deposited by reactive thermal evaporation at different oxygen partial pressures.	77
Fig. 5.4	XRD spectra of magnetron-sputtered tungsten oxide films deposited in various R_f .	79
Fig. 5.5	XRD spectra of magnetron-sputtered tungsten oxide films deposited at fixed $R_f = 2$, and various substrate temperatures.	80
Fig. 5.6	XPS spectra of thermally evaporated tungsten oxide films deposited on unheated substrates at various oxygen partial pressures.	81
Fig. 6.1	Cyclic voltammograms of the tungsten oxide films deposited by (a) magnetron sputtering on unheated substrate at fixed $R_f = 2$, and (b) thermal evaporation on unheated substrate at O ₂ partial pressure of 6 mTorr. The voltage scan rate was set at 400 mV s ⁻¹ . Arrows indicate the direction of scan.	85
Fig. 6.2	A typical plot of optical transmittance during a coloring/bleaching cycle and the corresponding variation of current for a magnetron-sputtered sample.	86

Fig. 6.3	The volume density of Li^+ ions intercalated and deintercalated charge into the magnetron-sputtered film (■ colored, □ bleached) and thermally evaporated film (● colored, ○ bleached) for each cycle when coloring/bleaching experiment proceeds.	88
Fig. 6.4	The optical absorption coefficient of the magnetron-sputtered film (■ colored, □ bleached) and thermally evaporated film (● colored, ○ bleached).	89
Fig. 6.5	The change of coloration efficiency of the magnetron-sputtered film (□) and thermally evaporated film (●).	91
Fig. 6.6(a)	Hardness of films deposited by magnetron sputtering film against indentation depth. Films were deposited at fixed pressure =10 mTorr and on unheated substrates. The inset magnifies details below 100 nm. ▼: MS11, $R_f=2$, ○: MS12, $R_f=1.75$, ■: MS13, $R_f=1.36$.	96
Fig. 6.6(b)	Elastic modulus of films deposited by magnetron sputtering film against indentation depth. Films were deposited at fixed pressure =10 mTorr and on unheated substrates. The inset magnifies details below 100 nm. ▼: MS11, $R_f=2$, ○: MS12, $R_f=1.75$, ■: MS13, $R_f=1.36$.	97
Fig. 6.7(a)	MS11, magnetron sputtered sample deposited at $R_f = 2$ on unheated substrate with roughness of 2.08 nm in $(2 \times 2) \mu\text{m}^2$.	98
Fig. 6.7(b)	MS21, magnetron sputtered sample deposited at $R_f = 2$ and $T_s = 110^\circ\text{C}$ with roughness of 1.14 nm in $(2 \times 2) \mu\text{m}^2$.	98
Fig. 6.7(c)	MS23, magnetron sputtered sample deposited at $R_f = 2$ and $T_s = 500^\circ\text{C}$ with roughness of 5.57 nm in $(2 \times 2) \mu\text{m}^2$.	99
Fig. 6.7(d)	TE4, thermally evaporated sample deposited at O_2 partial pressure = 4 mTorr with roughness of 21.07 nm in $(2 \times 2) \mu\text{m}^2$.	99
Fig. 6.8(a)	Hardness of films deposited by magnetron sputtering against indentation depth. Films were deposited at fixed pressure =10 mTorr and $R_f = 2$. The inset magnifies details below 100 nm. ▲: MS21, $T_s = 110^\circ\text{C}$, ○: MS22, $T_s = 300^\circ\text{C}$, ■: MS23, $T_s = 500^\circ\text{C}$.	100

- Fig. 6.8(b) Elastic modulus of films deposited by magnetron sputtering against indentation depth. Films were deposited at fixed pressure = 10 mTorr and $R_f = 2$. The inset magnifies details below 100 nm. 101
- ▲: MS21, $T_s = 110^\circ\text{C}$,
 ○: MS22, $T_s = 300^\circ\text{C}$,
 ■: MS23, $T_s = 500^\circ\text{C}$.
- Fig. 6.9(a) Hardness of thermally evaporated films deposited at various oxygen partial pressures against indentation depth. The inset magnifies details below 100 nm. 104
- : TE1, background pressure of 2×10^{-6} Torr,
 ○: TE3, 4 mTorr,
 □: TE4, 6 mTorr,
 ●: TE5, 10 mTorr.
- Fig. 6.9(b) Elastic modulus of thermally evaporated films deposited at various oxygen partial pressures against indentation depth. The inset magnifies details below 100 nm. 105
- : TE1, background pressure of 2×10^{-6} Torr,
 ○: TE3, 4 mTorr,
 □: TE4, 6 mTorr,
 ●: TE5, 10 mTorr.

Chapter 1

Introduction

1.1 Literature Review

1.1.1 Crystal Structures of Tungsten Oxide and Ion Intercalated Tungsten Oxide

Tungsten oxide has a structure constructed of edge-sharing and corner-sharing WO_6 -octahedra (Fig. 1.1). Octahedral sites are available for ion intercalation. Tungsten oxide has a tendency to form with slight deficiency in oxygen. The formula of tungsten oxide can be expressed as WO_{3-z} with $z > 0$.

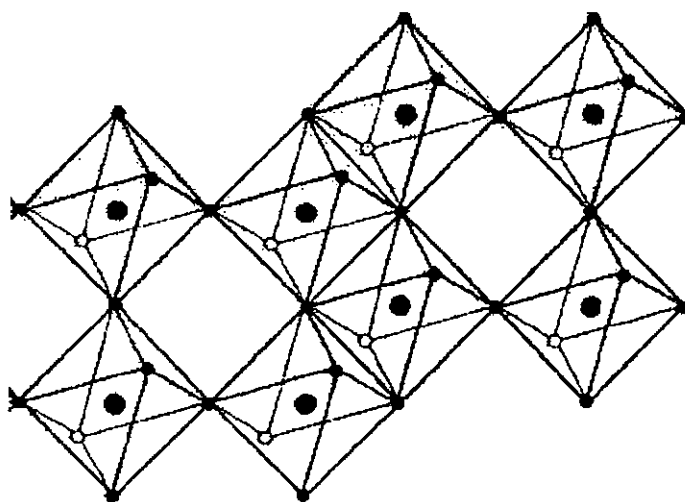


Fig. 1.1 Schematic illustration of a corner-sharing and edge-sharing arrangement of octahedra in a tungsten oxide crystal [Granqvist 1995].

- Tungsten atoms
- Oxygen atoms

Intercalation of ions causes the crystal structure of tungsten oxide to change. When ions of a group one element (M) in the Periodic Table are inserted into the structure, a tungsten bronze (M_xWO_3) structure is formed. Greenberg reported that for a M_xWO_3 structure with M being lithium (Li), the insertion coefficient x , lies between 0 and 0.5 [Greenberg 1994]. With increasing Li^+ content, the structure transforms according to the sequence of monoclinic, monoclinic/tetragonal (mixed phase), tetragonal, tetragonal/cubic and finally cubic structures. Deintercalation reverses the sequence of transformation, but the phase changes do not occur at precisely the same Li contents. The monoclinic structure is stable only for $x < 0.01$, and the tetragonal structure is found at $x \sim 0.1$ [Zhong *et al.* 1992^{a,b}].

1.1.2 Electrochromism

In 1969, Deb first discovered that the optical transmittance of tungsten oxide (WO_3) can be adjusted reversibly by injection of ions into, or extraction ions from the materials [Deb 1969]. Therefore, WO_3 became one of the most important inorganic electrochromic materials. WO_3 is changed from being transparent to be blue (absorbing) when ions of a group-one element (M) in the Periodic Table are inserted into the structure, such that a tungsten bronze (M_xWO_3) structure is formed [Dickens and Whittingham 1968, Faughnan *et al.* 1975]. To explain the electrochromic effect, it is found that tungsten atoms in the tungsten trioxide (WO_3) structure have a valence of +6 (W^{VI}). At this time, the material is transparent. When metal ions M^+ are incorporated, electrons would also be attracted for maintaining the charge neutrality. The electrons reduce the valence of some tungsten atoms to +5

(W^V). The chemical formula of the product is written as $M_x W_x^V W_{(1-x)}^{VI} O_3$, and the related reaction can be expressed by the chemical formula: $WO_3 + xe^- + xM^+ \Leftrightarrow M_x WO_3$ (absorbing) [Faughnan and Crandall 1980]. When a photon shines on $M_x W_x^V W_{(1-x)}^{VI} O_3$, it may be absorbed by an electron at a W^V site, and then excites the electron to transfer from a W^V site to an adjacent W^{VI} site. This causes the material to become optically absorbing. With this property, tungsten oxide is used as electrochromic devices (ECDs) for the applications of display, variable reflectance mirror, light modulator and variable emittance surface [Bani and Shay 1982, Faughan and Crandall 1980, Granqvist 1995].

1.1.3 Fabrication of Tungsten Oxide Films

Tungsten oxide films can be fabricated by various techniques. For the deposition of WO_3 films, different techniques, including thermal evaporation, sputtering, anodization, chemical vapour deposition and sol-gel techniques have been used. In thermal evaporation process, WO_3 powder is evaporated by a resistive evaporation boat or electron gun [Colton *et al.* 1978]. The relative density of evaporated WO_3 films varies strongly with the deposition conditions. A density 80 % of that of crystalline WO_3 was observed for a film deposited on unheated substrate in high vacuum ($\leq 10^{-5}$ Torr). Films made by evaporation are oxygen deficient. Therefore, O_2 gas is always admitted in order to retain the stoichiometry.

The deposition rate of tungsten oxide films by sputtering a W target with Ar and O_2 as reactant gases is lower than 0.1 nm s^{-1} , where oxidation of the target is

involved. The stoichiometry of the deposited films varies strongly with the ambient composition. [Akram *et al.* 1989]

Electrochemical and chemical techniques are commonly employed for preparing tungsten oxide films. Yamanaka explored the electrodeposition technique, in which aqueous peroxotungstic acid ($\text{H}_2[(\text{O}_2)_2\text{W}(\text{O})\text{O}(\text{O}_2)_2] \cdot n\text{H}_2\text{O}$) was used as the solution [Yamanaka 1987]. The properties of electrodeposited film are similar to that of evaporated films. Shen and Tseung reported that it is advantageous to add some alcohol into the solution. Post-annealing treatment around 180 °C for 1 hour was needed, giving the optimum electrochromic properties of the films [Shen and Tseung 1992].

Anodization is an electrochemical technique that is able to produce tungsten oxide films on metallic tungsten in sheet, rod, or thin film form. Anodization is conducted under potentiostatic, potentiodynamic, and galvanostatic conditions with anodizing voltage < 120 V. The crystallinity and thickness of film depend on the anodizing voltage [Delichere *et al.* 1988].

Bohnke *et al.*, Davazoglou and Donnadiou used chemical vapour deposition, in which pyrolysis of $\text{W}(\text{CO})_6$ occurred on substrate around 400 °C. The deposition process was conducted at atmosphere pressure and then annealed the deposits at 500 to 600 °C in oxidising or reducing atmosphere. This CVD-based technique led to electrochromic tungsten oxide films with different compositions. Their density lay in the range of 70 to 80 % of that of crystalline WO_3 [Bohnke *et al.* 1988, Davazoglou and Donnadiou 1987, Davazoglou and Donnadiou 1988].

Sol-gel-derived films can be made from colloidal solutions by dipping, spin-coating, or spraying. Chemseddine et al. reported that acidification was accomplished by passing a solution based on Na_2WO_4 or K_2WO_4 through a proton exchange resin. In the acidification process, the solution was applied to glass plates either directly by drops, spin coating, or spraying followed by spontaneous polymerization. After drying at elevated temperature, coatings with good electrochromism and optical anisotropy are obtained [Chemseddine *et al.* 1983].

1.1.4 Applications and Developments

ECDs can be designed to have different structures. Basically, a ECD contains a glass substrate, a transparent electron conducting electrode, an electrochromic film (e.g. WO_3), an ion conducting electrolyte (liquid or solid), and other transparent conducting top electrode (Fig. 1.2) [Granqvist 1992]. When a voltage is applied across the two electrodes, the device can be switched between a transparent (bleached) state and a colored state, according to the polarity of the applied voltage. The polarity determines the direction of the ion flow (Fig. 1.2). Some ECDs using tungsten oxide for optical switching are available in the market, such as electrochromic sun-glasses which transparency can be adjusted to cut down the light entering a room, office or car, and antidazzling electrochromic rear view mirrors for the use in vehicles [Monk *et al.* 1995].

Tungsten oxide should have potential market in optical modulation devices. However, the basic obstacle to widely open the market of ECDs comes from the long

switching time and unsatisfactory stability. The cost of production is also too high (USD 100 - 1000 per m²) [Bechinger *et al.* 1996]. Attempts have been made in improving the lifetime of the electrochromic properties of tungsten oxide under repetitive bleaching and coloring processes. For example, some electrolytes were selected to have less corrosion to the WO₃ film. Leakage of humidity in air into the liquid electrolyte was intentionally suppressed [Bohnke *et al.* 1982]. The porosity of the film material was intentionally decreased [Schlotter 1987] etc. Hashimoto *et al.* reported that the degradation mechanisms of tungsten oxide film in lithium salt electrolyte [Hashimoto *et al.* 1990] and the possibility of increasing the lifetime of the films by doping some titanium [Depero *et al.* 1996, Hashimoto and Matsuoka 1991]. Monk *et al.* demonstrated that the composition of WO₃ films could be tailored by doping of some metal oxides such as Ag, Co, Cr, Cu, Fe, Mo, Ni, Ru or Zn oxides, such that the structure is changed to enhance the lifetime. [Monk *et al.* 1993, Monk *et al.* 1994]. Azens *et al.* reported that improvement of surface texture by electron bombardment on the surface of tungsten oxide can enhance the stability of WO₃ films [Azens *et al.* 1995]. Recently, Bechinger *et al.* illustrated that, when the highly lithium ion conducting MgF₂ was used as ion conductor in electrochromic devices, the switching voltage can be decreased [Bechinger *et al.* 1996]. Furthermore, self-powered electrochromic windows have been developed, where a photovoltaic cell provides the power to activate an electrochromic system deposited on top of the solar cell in order to reduce the cost of power consumption of the device [Bechinger and Gregg 1998].

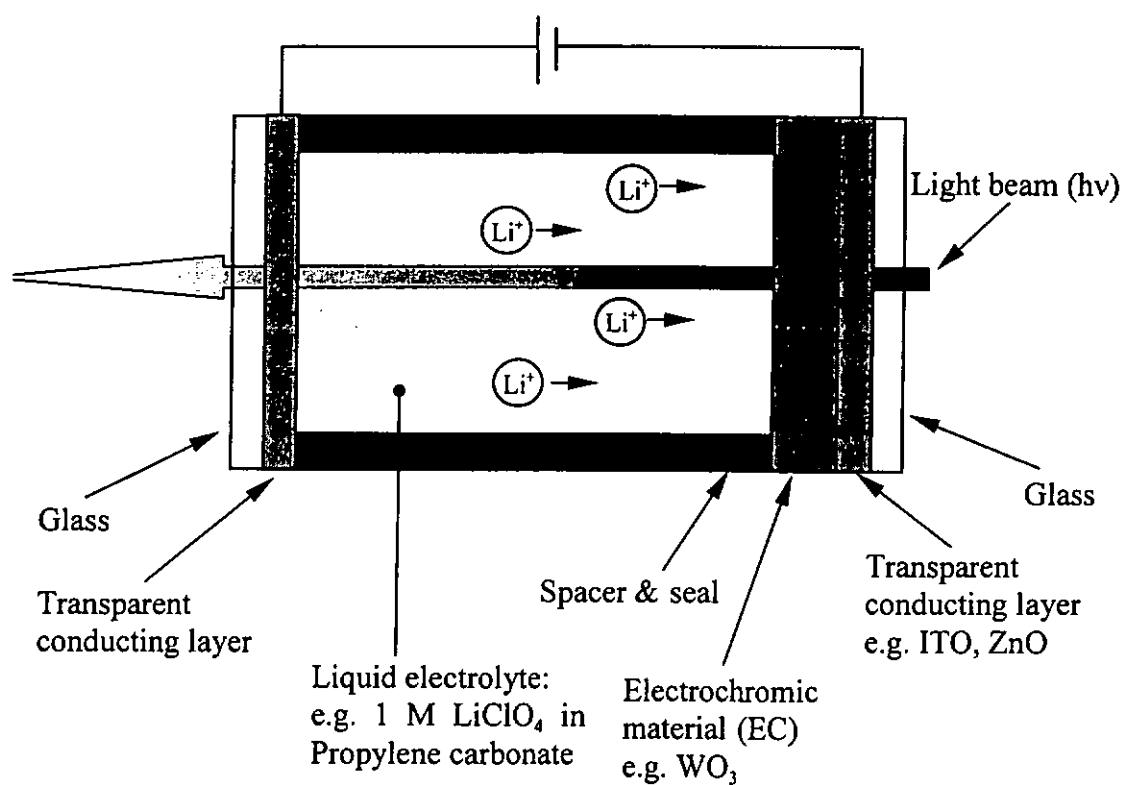


Fig. 1.2 Schematic diagram of an electrochromic light modulator in transmittance mode (with a transparent counter electrode), indicating transport of positive ions, Li⁺, under the action of an electric field.

1.2 Scope of Study

The purpose of this study is to find out the relationship among the structure, composition, mechanical and electrochromic properties of WO_3 films deposited by two different methods, namely thermal evaporation and magnetron sputtering at various preparation conditions. In the first part of the work, the preparation conditions were optimized, in order to obtain the W-to-O ratio in the films to be close to 1:3, namely the value to WO_3 crystal. This requirement is important in obtaining tungsten oxide films with the desired electrochromic properties.

In the second part of the work, the structure of the samples was examined. XRD was used to investigate the crystallinity of the samples. X-ray photoelectron spectroscopy (XPS) was used to examine the film composition and chemical structure, and Fourier transform infrared absorption spectroscopy (FTIR) was used to examine the bonding. The XPS data collected after each ion sputtering process during depth analysis were analyzed and discussed. Results show that depth analysis of tungsten oxide show that ion sputtering for depth profile analysis would cause preferential sputtering of O, induce some erroneous results in the XPS analysis.

Thirdly, cyclic voltammetry was used to investigate the electrochemical properties of the films. In a 1 M lithium perchlorate (LiClO_4) dissolved in propylene carbonate ($\text{C}_4\text{H}_6\text{O}_3$) liquid electrolyte, the conducting indium tin oxide layer in contact with the tungsten oxide film was used as the working electrode, so as to observe the stability and electrochromic response of the material. At the same time, the transmittance of the film is measured by detecting the change in the intensity

penetrating through the sample, such that the electrochromic properties of the samples can be evaluated.

Nanoindentation tests were carried out to determine the mechanical properties of the films. In addition, surface topography of the film was recorded by using an atomic force microscope (AFM). By correlating the mechanical properties, density and AFM image etc., the effects of varying the deposition parameters on the composition, structure, electrochromic and mechanical properties of the films were investigated and discussed.

Chapter 2

Sample Preparation

Two different techniques were used for sample preparation. They are reactive dc magnetron sputtering and reactive thermal evaporation.

The preparation system has two chambers, which share the same vacuum system. One chamber is for magnetron sputtering while the other is for thermal evaporation. The vacuum system consists of an oil diffusion pump (Edwards, Diffstak MK2 160/700C 760 l s⁻¹) equipped with an oil rotary pump (Edwards, E2M12F 24 l s⁻¹), which can pump down the chamber to a background pressure of 2×10^{-6} Torr. In this chapter, the features of the two techniques are described and the preparation conditions are tabulated for future reference.

2.1 Reactive Magnetron Sputtering

The magnetron-sputtering chamber (Fig. 2.1) contains three Ø50.8 mm magnetron sputtering guns (Kurt J. Lesker, TORUS 2C). For this study, only one DC powered sputtering gun was used. The maximum power rating of the DC power supply (Advanced Energy MDX 1K Magnetron Drive) is 1 kW (1 A, 1000 V). A metal tungsten (W) disc (Kurt J. Lesker, purity 99.95 %) 50.8 mm in diameter and 3 mm thick, was used as the sputtering target. The DC magnetron gun was mounted,

such that its axis makes an angle of 10° with the substrate normal. Silicon, fuse silica and $\text{In}_2\text{O}_3:\text{Sn}$ (ITO) coated glass were used as substrates. The ITO coating is 30 nm thick and a sheet resistance of $100 \Omega/\square$. The substrate was mounted on a holder 16 cm apart from the target, and was rotated during deposition to ensure the film has a uniform thickness.

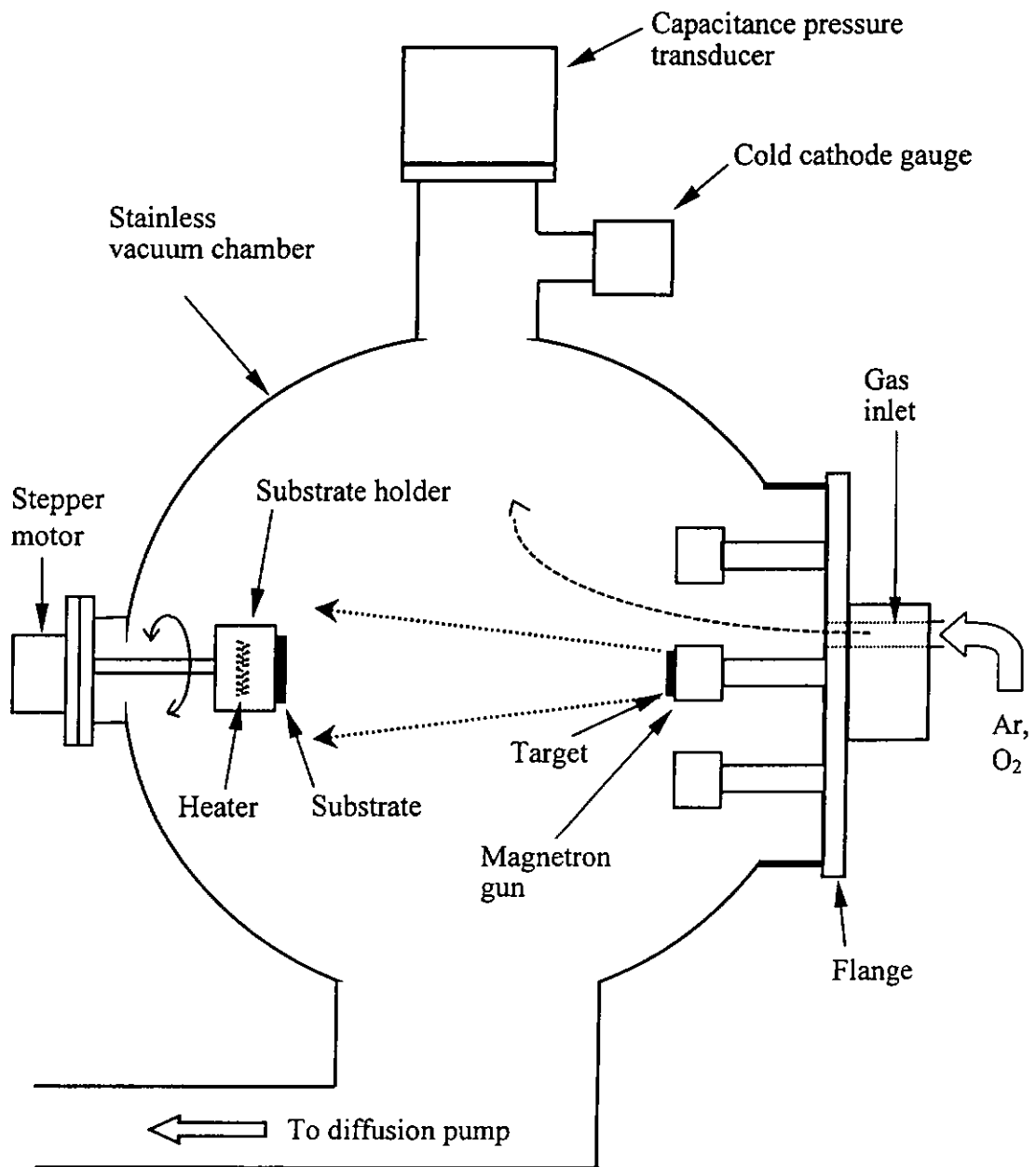


Fig. 2.1 Schematic diagram of the magnetron sputtering chamber (Front view).

Argon (Ar) and oxygen (O₂) gases were admitted into the chamber. The flow rate of the gases, denoted by [Ar] and [O₂], was controlled by using two mass flow controllers (MKS Model 1259 and 1359) independently. The pressure in the stainless steel chamber was monitored by a capacitance pressure transducer (MKS, Model 122B) in the range of 20×10^{-3} to 1×10^{-3} Torr and a cold cathode gauge tube (HPS, 941) in high vacuum range.

Electrons are confined by the magnetic field in front of the sputtering target. [Chapman and Mangano 1988]. The electrons collide frequently with the reactant gas molecules, such that the molecules are ionized and react with the sputtered metal species to form the oxide films [Fraser and Westwood 1990].

2.2 Reactive Thermal Evaporation

Reactive thermal evaporation was carried out in a glass bell jar (Fig. 2.2). Tungsten trioxide powder (WO₃) (Kurt J. Lesker, purity 99.99 %) was evaporated from a tungsten boat. The tungsten boat was heated by passing a current with a power supply (Kurt J. Lesker EPS-2000). The substrate was placed 20 cm above the evaporation boat. It is because WO₃ powder may be decomposed when heated, causing deficit in oxygen content in the deposits, therefore, additional oxygen gas (O₂) is released to the bell jar during deposition through a leak valve for compensation [Deshpandey and Bunshah 1990].

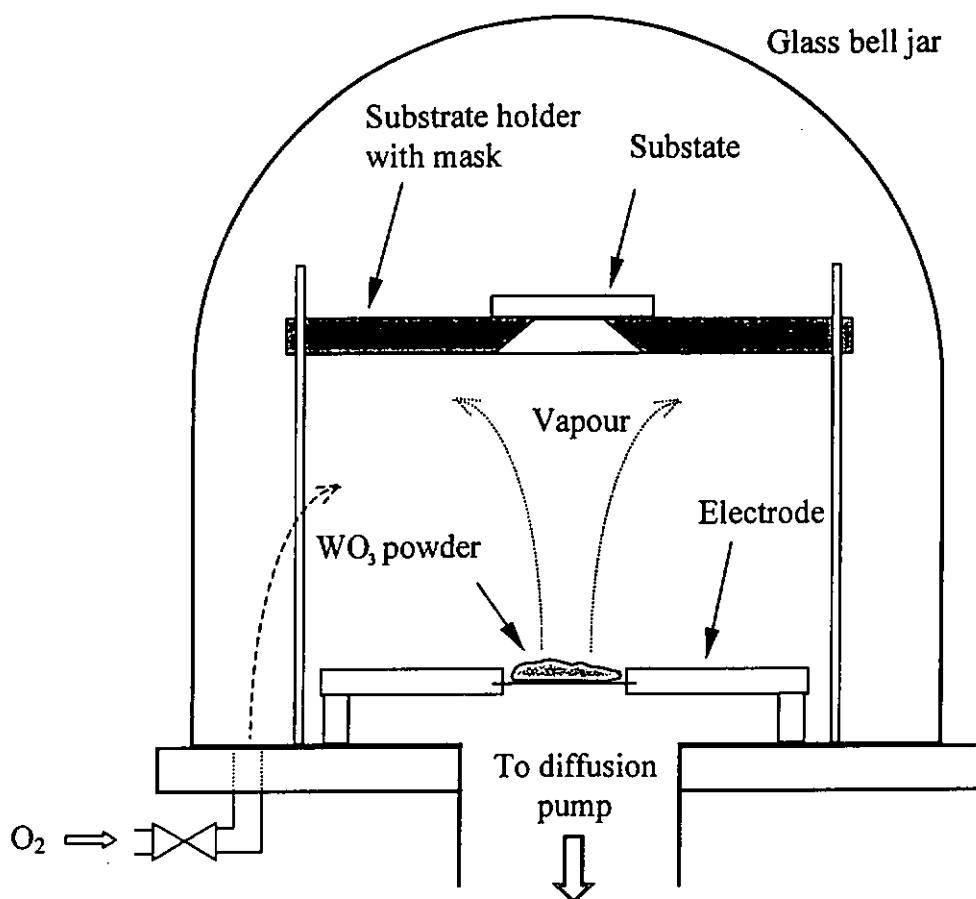


Fig. 2.2 Schematic diagram of the thermal evaporation chamber (Front view).

2.3 Preparation Conditions

For reactive magnetron sputtering, the reactant gas ratio, substrate temperature and working pressure are varied as preparation parameters (Table 2.1). For all runs of deposition, the target was firstly pre-sputtered by operating the magnetron gun at 20 mTorr of Ar with a power density of 4 W cm^{-2} for 5 minutes. This process removed the oxide layer on the target surface. The overall total flow rate of the admixture of reactant gases was fixed at 3.3 sccm.

Sample	R_f	Substrate temperature (°C)	Total pressure (mTorr)	Total gas flow rate (sccm)	Power density (W cm ⁻²)
MS11	2	Unheated	10	3.3	4
MS12	1.75				
MS13	1.36				
MS21	2	110	10	3.3	4
MS22		300			
MS23		500			
MSP1	2	Unheated	10	3.3	4.2
MSP2			15		
MSP3			20		

Table 2.1 Summary of the preparation parameters of the tungsten oxide film deposited by reactive dc magnetron sputtering.

For reactive thermal evaporation, the oxygen partial pressure was varied as the preparation parameter (Table 2.2) [Morita and Washida 1984]. The current passing through the tungsten boat was varied from 250 to 320 A. The substrate was not intentionally heated.

Sample	O ₂ Partial Pressure (mTorr)	Current (A)	Substrate temperature (°C)
TE1	Background (2 × 10 ⁻⁶ Torr)	250 - 320	Unheated
TE2	0.4		
TE3	4		
TE4	6		
TE5	10		

Table 2.2 Summary of the preparation parameters of the tungsten oxide films deposited by reactive thermal evaporation.

Chapter 3

Sample Characterization

In this chapter, the methods for characterizing the structure, chemical composition, electrochromic properties as well as the mechanical properties of the tungsten oxide films will be given.

The compositional and structural analyses of the films are important, since they ultimately affect the electrochromic properties of the samples. The film thickness was measured by an Alpha-Step[®] surface profiler. X-ray photoelectron spectroscopy (XPS) were used to investigate the elemental composition. The depth profiles of the composition were also revealed. In particular the data of XPS analyses also provide information on the chemical structure of the films. Fourier transform infrared absorption spectroscopy (FTIR) was used to explore the chemical bonds between the atoms. X-ray diffraction (XRD) was employed to investigate the crystallinity of the films. Finally, an atomic force microscopy (AFM) was used to investigate the surface topology of the samples.

The electrochromic properties were characterized by a potentiostat as well as an optical transmittance measurement set up. Potentiostat operated in the mode of cyclic voltammetry, such that the cyclic voltammogram and the optical transmittance, during coloring/bleaching cycles were recorded simultaneously.

The mechanical properties of the films, including the hardness (H) and elastic modulus (E), were evaluated using a nanoindenter so as to find out the change in the mechanical properties of the films prepared by different methods at different deposition conditions.

We describe these techniques and the related equipment in the following section.

3.1 Thickness Measurements

A Tencor 500 Alpha-Step[®] surface profiler was used to measure the film thickness. The vertical displacement resolution of the machine is 1 nm. During measurement, a diamond stylus is driven to scan across the film edge. The vertical displacement of the stylus is recorded and converted to represent the real physical displacement (Fig. 3.1), from which film thickness t is determined.

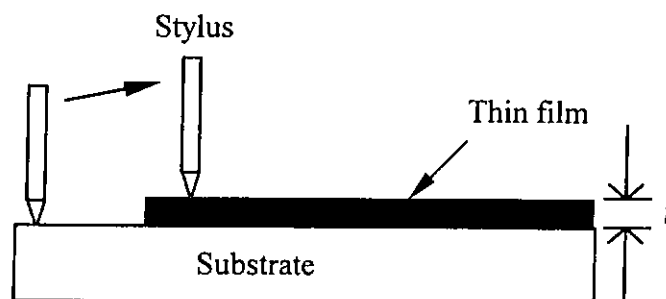


Fig. 3.1 Thickness measurement by an α -step profiler.

3.2 X-ray Photoelectron Spectroscopy

A Phi Quantum 2000 X-ray photoelectron spectroscopy (XPS) was used to determine the composition and the chemical structure of the films. The system was kept at base pressure of 2×10^{-9} Torr. X-rays were generated by bombarding an Al anode with 10 keV electrons as shown in Fig. 3.2. X-ray photons ($h\nu = 1486.6$ eV) hit and knock out the core electrons of the atoms in the sample. The kinetic energy of a core electron is $E_K = h\nu - E_B$, where E_B is the binding energy of the electron. To determine E_B , E_K was measured by a hemispherical electron energy analyzer and the relative intensity of the electron flux was counted by an electron detector [Feldman and Mayer 1986]. Indeed, E_B of the photoelectron is:

$$E_B = h\nu - E_K - \phi_{\text{spec}}, \quad (3.1)$$

where ϕ_{spec} is the work function of the machine, which could be obtained by some calibration procedures. From the characteristic values of E_K of the photoelectrons emitted from different kinds of elements in the sample, the composition of the sample can be determined.

To determine the composition of a sample, the photoelectron spectrum of each element was recorded before and after surface cleaning with an Ar^+ ion beam. The relative content of a specific element, denoted as F_i for instance, can be calculated from the integrated areas of the spectra of all the elements after removing the Shirley background, according to the following formula [Shirley 1972]:

$$F_i = \frac{A_i / f_i}{\sum_j (A_j / f_j)} \times 100 \text{ at.}\%, \quad (3.2)$$

where A_j and f_j are the area of the spectrum and sensitivity factor of the j th kind of element. The sensitivity factors, f_j , of the elements involved in this study are tabulated in Table 3.1.

f_{W4f}	f_{O1s}	f_{C1s}	f_{Li1s}	f_{Cl2p}
3.863	0.733	0.314	0.028	0.954

Table 3.1 The XPS sensitivity factors of tungsten (W), oxygen (O), carbon (C), lithium (Li) and chlorine (Cl).

In addition, it is because the peak position of a photoelectron spectrum is influenced by the chemical environment of the atoms, so that by observing the peak shifts of the spectra, one may examine the chemical structure of the film. Due to the charge accumulation on the surface of insulating samples, the peak of a spectrum may be erroneously shifted without relating any structural information. This shift can be reduced by turning on a charge neutralizer which imposes some electrons to the sample to compensate the loss of negative charge due to the emission of photoelectrons. Furthermore, graphite C 1s peak is quite usually to appear at 284.5 eV, and can be used as a standard for correcting this systematic error.

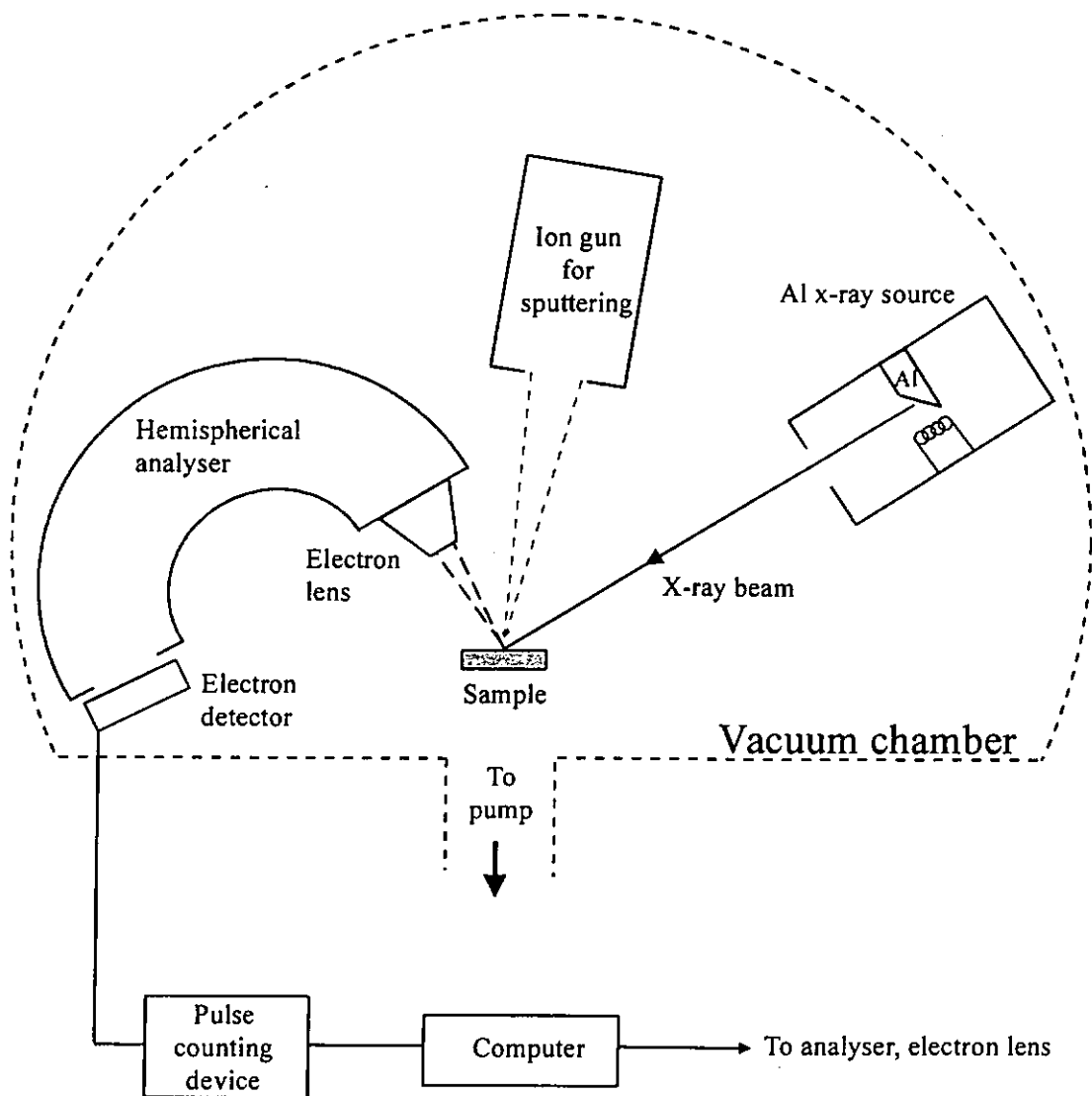


Fig. 3.2 The schematic diagram of an XPS system.

3.3 Fourier Transform Infrared Absorption Spectroscopy

A Nicolet's, Magna-TR™ system 760 was used to investigate the IR absorption spectra of the films (Fig 3.3), with the wavenumber varying in the range of 400 to 4000 cm^{-1} . Each spectrum was obtained by averaging 32 identical scans.

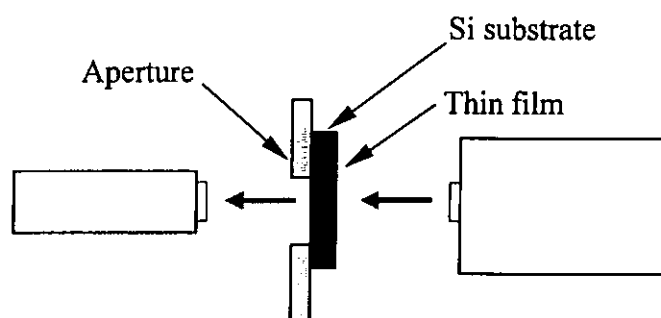


Fig. 3.3 Schematic diagram of an IR absorption experiment.

An absorption band occurs when the incident photons are absorbed by a solid to excite phonons. The frequency of the photon to be absorbed is equal to the vibration frequency of the phonons, and so is a characteristic information of the material structure. Furthermore, the relative intensities of the absorption bands can reflect the abundance of the structural phase associated to the characteristic vibration. For IR measurements, films on Si substrates were used. The background caused by the Si substrate was subtracted, such that the net absorption spectrum of the film was attained [Smith 1996].

3.4 X-ray Diffraction

A Philips X'PERT X-ray diffractometer with Cu K_α radiation source ($\lambda = 1.54 \text{ \AA}$) was used for exploring the crystallinity of the films (Fig. 3.4). The parallel beam optics for thin film geometry was employed. In this mode, the incident x-ray beam is directed to shine on the film surface with a small grazing angle of 0.65° , so as to increase the interaction path between the beam and the film material. The detector is driven to scan from $2\theta = 15^\circ$ to 70° . If there are grains in the samples having lattice planes with a separation of d , when the angles θ_1 and θ_2 shown in Fig. 3.4 are equal ($=\theta$), and the Bragg condition:

$$\lambda = 2d \sin \theta, \quad (3.3)$$

is satisfied consequently, constructive interference occurs and a strong diffraction peak is observed.

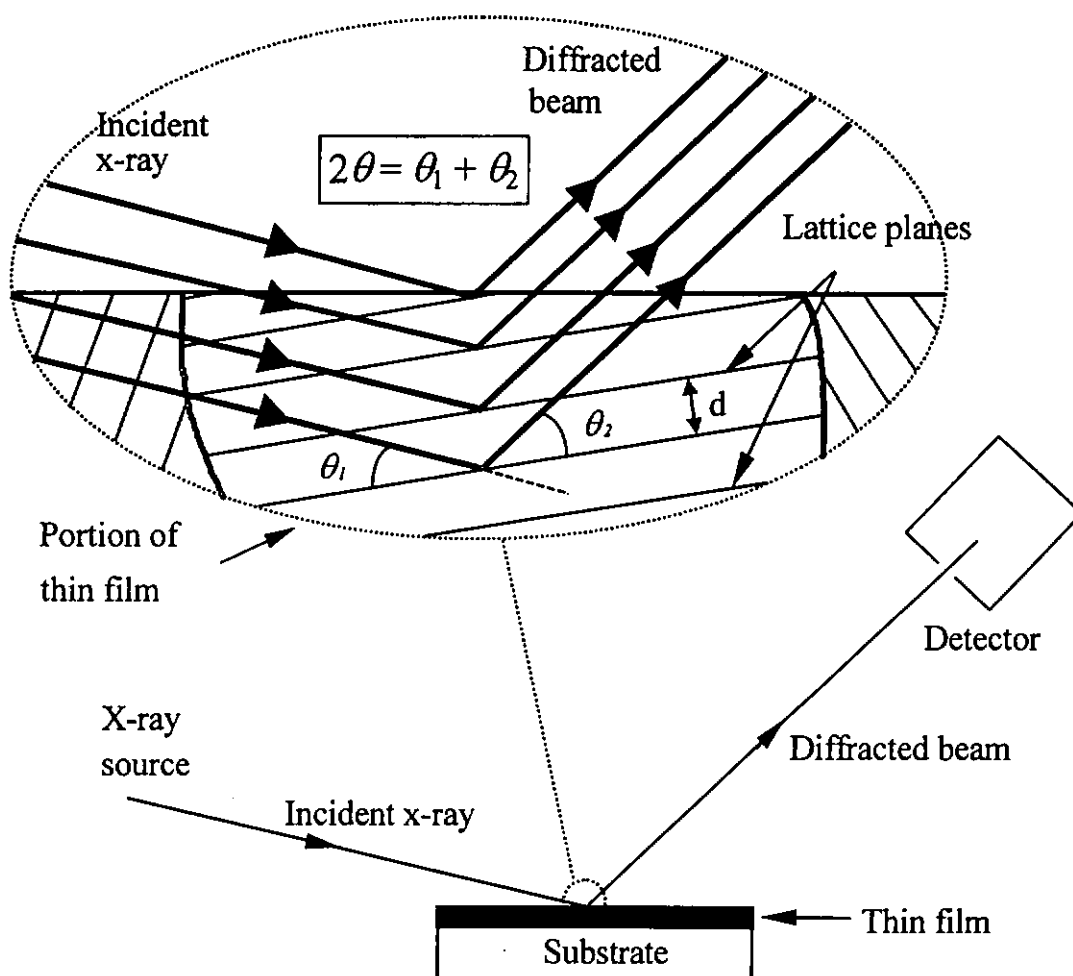


Fig. 3.4 Schematic diagram of 2θ scanning mode of XRD experiment.

3.5 Cyclic Voltammetry

The electrochemical measurements were made with a three-electrode system with a EG &G Model 273 (Fig.3.5). Potentiostat in which scanning potential was driven by the Electrochemical Analysis software, Model 270 of EG & G. The three-electrode configuration was used to contain a saturated calomel electrode (SCE) (+214 mV VS NHE), a working electrode which is the film itself, a counter electrode which is a Platinum (Pt) strip. The sample was immersed in a cuvette containing electrolyte which is 1 M lithium perchlorate (LiClO_4) dissolved in propylene carbonate ($\text{C}_4\text{H}_6\text{O}_3$).

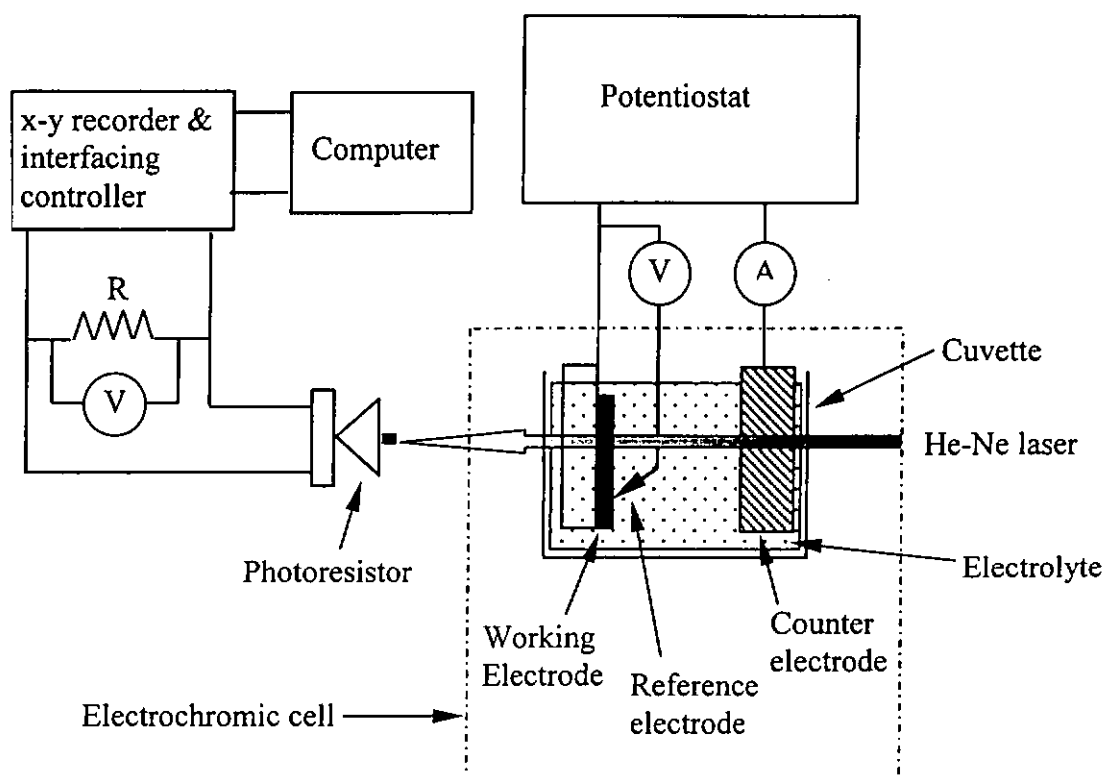


Fig. 3.5 Schematic presentation of the experimental setup for the measurement of electrochromic properties of the film, at $\lambda = 632.8 \text{ nm}$.

In a CV experiment, the potentiostat applies a reversible ramping potential scan between the working and reference electrodes. The potentiostat measures the instantaneous current induced by the applied potential during the scanning.

Cyclic voltammetry experiments were used qualitatively to characterize an electrochemical system. The cyclic voltammetry experiment is able to be operated in single CV mode, where only one cycle is carried out. Multiple CV experiments refer to the operations where many scanning cycles were carried out. CV measurements can identify whether the coloration process is reversible, the total amount of charge injected into or extracted from the sample in the oxidation or reduction processes, and the diffusion reaction associated with the motion of charge, as well as the stability of the samples. Multiple CV experiments were also used to see the chemical processes when time proceeds, observe reaction products formed at the surface of the sample, and quantitative determine the charge density accumulated in the film after certain number of the intercalation/deintercalation cycles have completed [Greef *et al.* 1985].

3.6 Optical Transmission Measurements

Electrochromic switching (coloring/bleaching) of tungsten oxide films were investigated by means of a setup shown in Fig. 3.5. In this system, a He-Ne laser was used as the light source. A photoresistor was used to detect the intensity of the light transmitting through the sample. The photoresistor is in series with a standard resistor and a dc power supply set at a voltage of 3 V. The voltage across the resistor was detected and recorded by a computer to show the change in the transmittance of film during the coloring/bleaching cycling. The response of the resistor under the illumination of different laser transmittance was first calibrated using a set of neutral density filters.

The He-Ne laser beam with a wavelength $\lambda = 632.8 \text{ nm}$ and intensity I_0 passes through the sample on ITO coated glass, and comes out with an intensity I . The optical absorption coefficient $\alpha_{(\lambda=632.8\text{nm})}$ can be determined by the following equation :

$$\alpha_{(\lambda)} = \frac{1}{t} \ln \left(\frac{I_{o(\lambda)}}{I_{(\lambda)}} \right), \quad (3.4)$$

where t is the film thickness.

3.7 Nanoindentation Measurements

The hardness (H) of a film is an important parameter to reflect the mechanical properties of a coating. However, a conventional indenter (Vicker hardness tester and Knoop hardness tester) is not accurate enough for measuring the hardness of thin film samples. This is because the load range of this kind of machines (10 - 2000 mgf) is too heavy, such that the diamond tip may penetrate through the film when performing indentation, and the influence of substrate deformation is significant.

The Nanoindenter[®] (Nano Instruments Inc., Model IIs) used for our hardness tests greatly reduce the substrate effect, since the minimum load of this instrument is 500 nN, and the resolution of the penetration depth is claimed to be as good as 0.04 nm. With such a low load range, the influence of substrate deformation in a hardness test of a film with a few hundred nanometer thick is practically negligible.

In principle, the nanoindenter has a Berkovich indenter head (a 3-sided pyramidal diamond tip). The normal load of the indenter is controlled by a current passing through a coil. A magnetic field is generated to interact with a permanent magnet, which is attached to the indenter shaft. The displacement of the indenter is converted to a voltage signal by a capacitance displacement gauge. The electrical signal from the gauge is then amplified and recorded by a computer.

We first followed the procedures proposed by [Oliver and Pharr 1992] to calibrate the area function $A(h_c)$ of the diamond tip and the load frame stiffness S of

the indenter. Indentation tests with different maximum loads were then made. Each indentation cycle consists of a loading curve and an unloading curve (Fig. 3.6), corresponding to adding or removing the normal load.

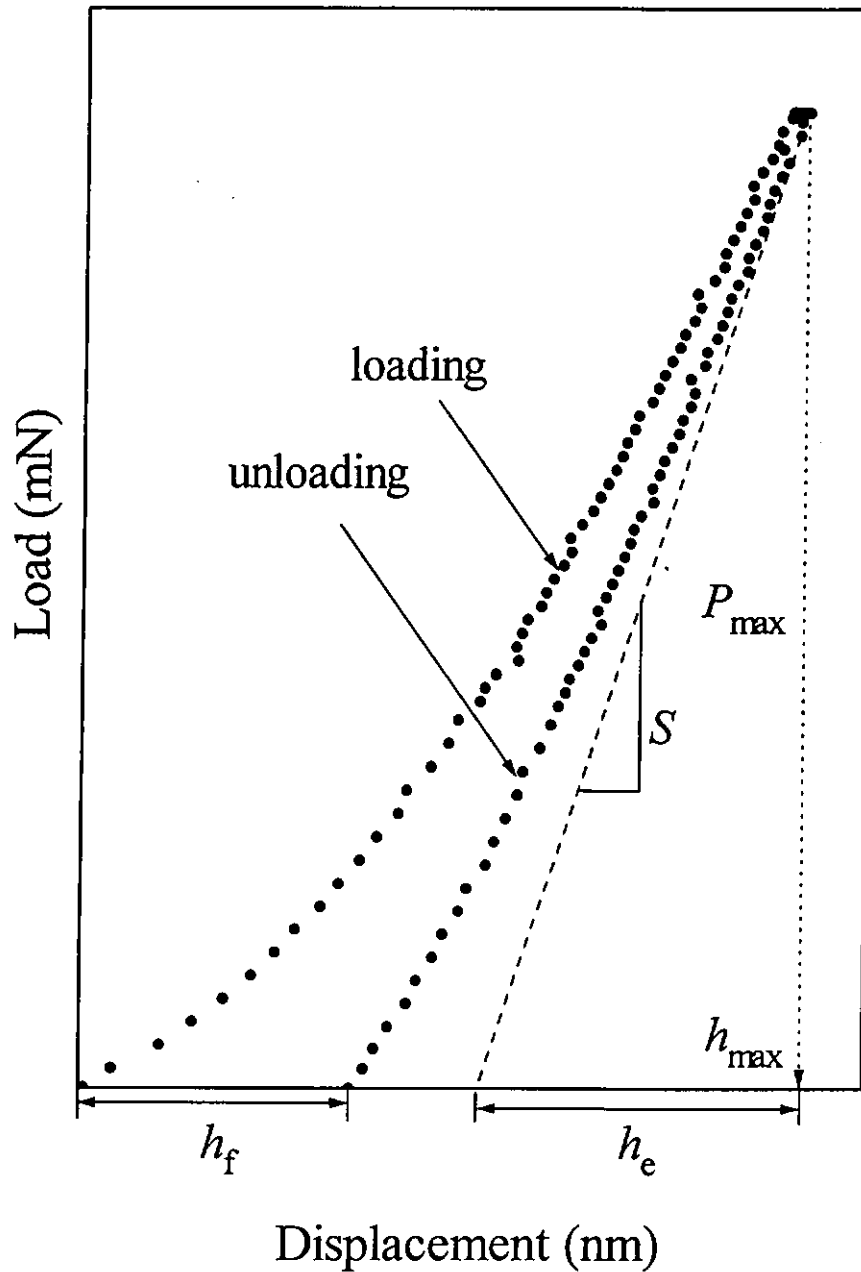


Fig. 3.6 A typical pattern of loading/unloading curves of a nanoindentation.

The unloading curve is then fitted using a power law function:

$$P_{max} = K (h_{max} - h_f)^m, \quad (3.5)$$

where P_{max} and h_{max} are the maximum applied normal load and displacement of the diamond tip, K and m are constants, and h_f is the depth of indent after the normal load is completely removed. K , h_f and m are determined from least-squares-fit 90 % of the data in the unloading curve is used for the fitting. It is assumed that during indentation, both elastic deformation and plastic deformation are generated. When the normal load is removed, the elastic deformation recovers first. The elastic deformation at the maximum load is then represented by a depth h_e as shown in Fig.3.7. Before determining the value of h_e , the stiffness S at load P_{max} is first attained, which is equal to the slope of the unloading curve at P_{max} (Fig.3.6). h_e is thus determined as:

$$h_e = \varepsilon \frac{P_{max}}{S}, \quad (3.6)$$

ε in equation (3.6) is set to be 0.75, assuming that the indenter head has a parabolic revolution geometry. The plastic displacement (contact depth) h_c at maximum load P_{max} is thus determined as:

$$h_c = h_{max} - h_e, \quad (3.7)$$

The contact area can be determined from h_c and the area function $A(h_c)$ which is needed to be calibrated separately at the beginning. The film hardness H is then calculated as:

$$H = \frac{P_{max}}{A(h_c)}. \quad (3.8)$$

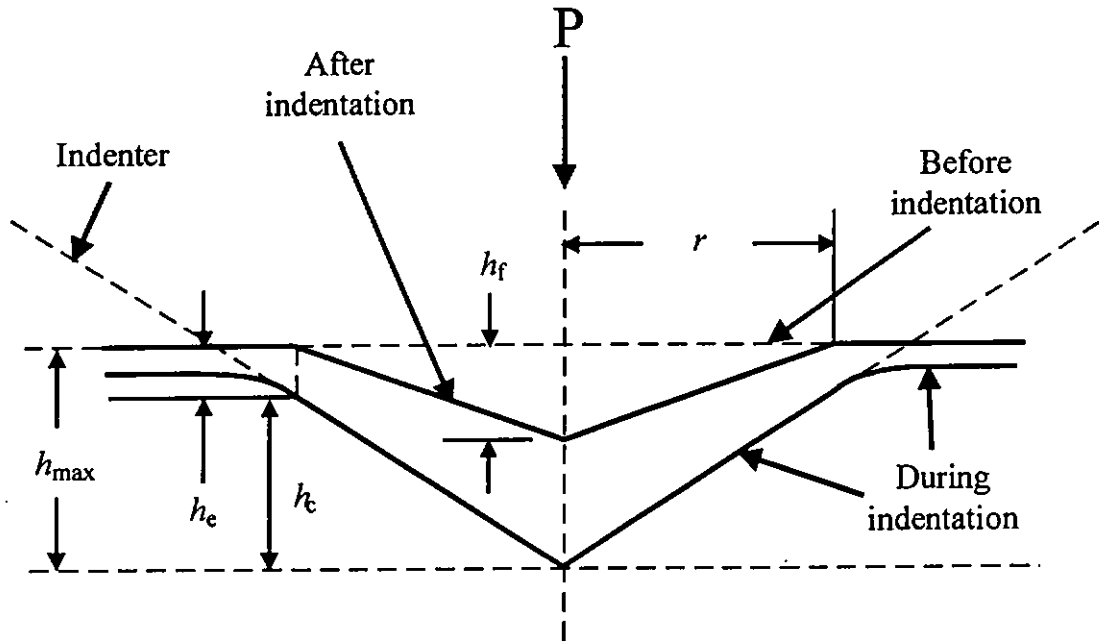


Fig. 3.7 Deformation generated during indentation. r is the radius of the contact circle [Oliver and Pharr 1992].

In addition, the reduced elastic modulus E_r is determined by the formula :

$$S = \frac{2}{\sqrt{\pi}} E_r \sqrt{A(h_c)}, \quad (3.9)$$

where E_r is given by :

$$\frac{1}{E_r} = \frac{1 - \nu_i^2}{E_i} + \frac{1 - \nu_s^2}{E} \quad (3.10)$$

In equation (3.10), ν_i ($= 0.07$) and E_i ($= 1141$ GPa) are the Poisson's ratio and elastic modulus of diamond, and ν_s represents the Poisson's ratio of the film and is assumed to be 0.25 for our samples [Oliver and Pharr 1992]. E , the elastic modulus of the film, can thus be calculated accordingly. The Poisson's ratio of the tungsten oxide films

cannot be determined in this experiment, and is assumed to be 0.25, a value by averaging those of various materials. This assumption is based on the fact that the Poisson's ratios of most materials only varies within a narrow range of 0.15 to 0.35, so that the percentage error of the calculated E is estimated to be confined below 6 %.

For each sample, 30 indentations were made at different fresh points in the form of a 5 by 6 matrix. Adjacent indentations were made with a separation of 75 μm . Detailed experimental conditions are described in Table 3.1. Each experiment performed at one point contained three loading segments with successively increasing maximum loads, such that three hardness data corresponding to three different depths are achieved. Each experiment was repeated four times for getting average values of H and E . Six experiments involving different maximum loads were carried out. The normal loads assigned to these experiments are broad enough for one to identify when the substrate effect becomes significant.

Experiment	Indentation	Maximum load (μN)		
1	1 – 5	300	1400	3300
2	6 – 10	150	500	2200
3	11 – 15	120	350	960
4	16 – 20	110	250	680
5	21 – 25	70	210	430
6	26 – 30	30000	60000	90000

Table 3.2 The maximum loads used for the nanoindentation experiments.

Chapter 4

Composition Analysis by X-ray Photoelectron Spectroscopy

In this chapter, we present the results of XPS analysis on the films prepared by magnetron sputtering, thermal evaporation, and the films after experiencing coloring/bleaching cycles for a number of times. Results of XPS depth profile analysis show that ion sputtering of tungsten oxide films induces substantial preferential sputtering of oxygen, such that the data obtained cannot reflect the real composition of the films. Ion accumulation in the films after repetitive coloring/bleaching cycles are discussed.

4.1 Effects of Oxygen-to-Argon Ratio on the Composition of Magnetron-Sputtered Films

The XPS spectra of W 4f, O 1s and C 1s photoelectrons emitted from the tungsten oxide films prepared by dc magnetron sputtering are investigated to reveal the composition and chemical structures of the material. The oxygen-to-argon ratio $[O_2]/[Ar]$, denoted as R_f , was varied as parameter. The total pressure was fixed at 10 mTorr, whereas the substrate was not heated.

Fig. 4.1 (a) to (c) show the W 4f and O 1s photoelectrons of the specimens deposited at $R_f = 2$ (MS11), 1.75 (MS12) and 1.36 (MS13). Consider the W 4f photoelectron spectra first (Fig. 4.1(a)). After subtracting the Shirley background (the dashed line), the spectrum (solid line) was fitted by components (dotted lines), each composed of 28% Lorentzian and 72% Gaussian constituents. From the figures, one sees that each component is a spin-orbit split containing two peaks associated with W 4f_{7/2} and W 4f_{5/2} the states of tungsten. The energy split between the two peaks is ~ 2.18 eV. A satellite W 5p, about 5.6 eV apart from the W 4f_{7/2} peak, is also attached. The peak energy of the W 4f_{7/2} line, and integrated area and full width at half maximum (FWHM) of the overall W 4f spectrum are obtained by least-squares-fit method, which are tabulated in Table 4.1(a) and Fig. 4.2.

For the sample MS11 and MS12, which were deposited by magnetron sputtering at $R_f = 2$ and 1.75, the spectra contain only one component, denoted as W^I, with the W 4f_{7/2} appears at 35.6 eV. This peak energy is close to that of tungsten trioxide phase (WO₃) corresponding to the tungsten atoms having a valence of six,

(W^{VI}). However, the sample (MS13), deposited at $R_f = 1.36$ exhibits an asymmetric feature, which can be a W 4f spectrum decomposed into three components, denoted as W^1 , W^2 and W^3 , respectively. The FWHM of the three deconvoluted components of the film with $R_f = 1.36$ are broad compared with those of the films with higher R_f . This is because the film with low R_f is deficient in oxygen, and the disorder in the film increases, so that the environment surrounding tungsten atoms varies considerably from atom to atom, resulting in the broadening of the components. The W 4f_{7/2} line of the W^1 peak is located at 35.5 eV and possibly be assigned to the largest fraction of tungsten atoms in the W^{VI} or W^V states [Sabbatini *et al.* 1983]. The peak of the W 4f_{7/2} line of the W^2 component is at 33.2 eV, which is attributed to the W^{III} state. The peak of W 4f_{7/2} line of the W^3 component is at 31.7 eV and should come from those tungsten atoms in metallic state. The appearance of the tungsten states with lower valences is due to the oxygen deficiency associated with the use of low R_f during deposition. The film is therefore dark brown in color.

Referring to the O 1s spectra, they do not show detailed features, but are slightly asymmetric, such that the lines are fitted by using two components, O^1 and O^2 . As summarized in Table 4.1(a), the peak position of the O^1 component of all the samples are close to 530.6 eV. The O^1 component is thus attributed to the oxygen atoms combining with tungsten analogous to these in the WO_3 structure [Moulder *et al.* 1992]. The O^2 component is weaker, having a maximum position lies between 531.7 and 532.5 eV. This component is assigned to the oxygen atoms in some WO_x atomic network in the films with x being smaller than 3. By taking the whole W and O components into account, the oxygen-to-tungsten ratio (O/W) combining together in the films MS11 and MS12 are 3.1 and 3.2, respectively. However, for sample

MS13, the O content is deficient, while the O/W ratio is 2.6, lower than that of the stoichiometric crystalline phase WO_3 (Table 4.1(b)).

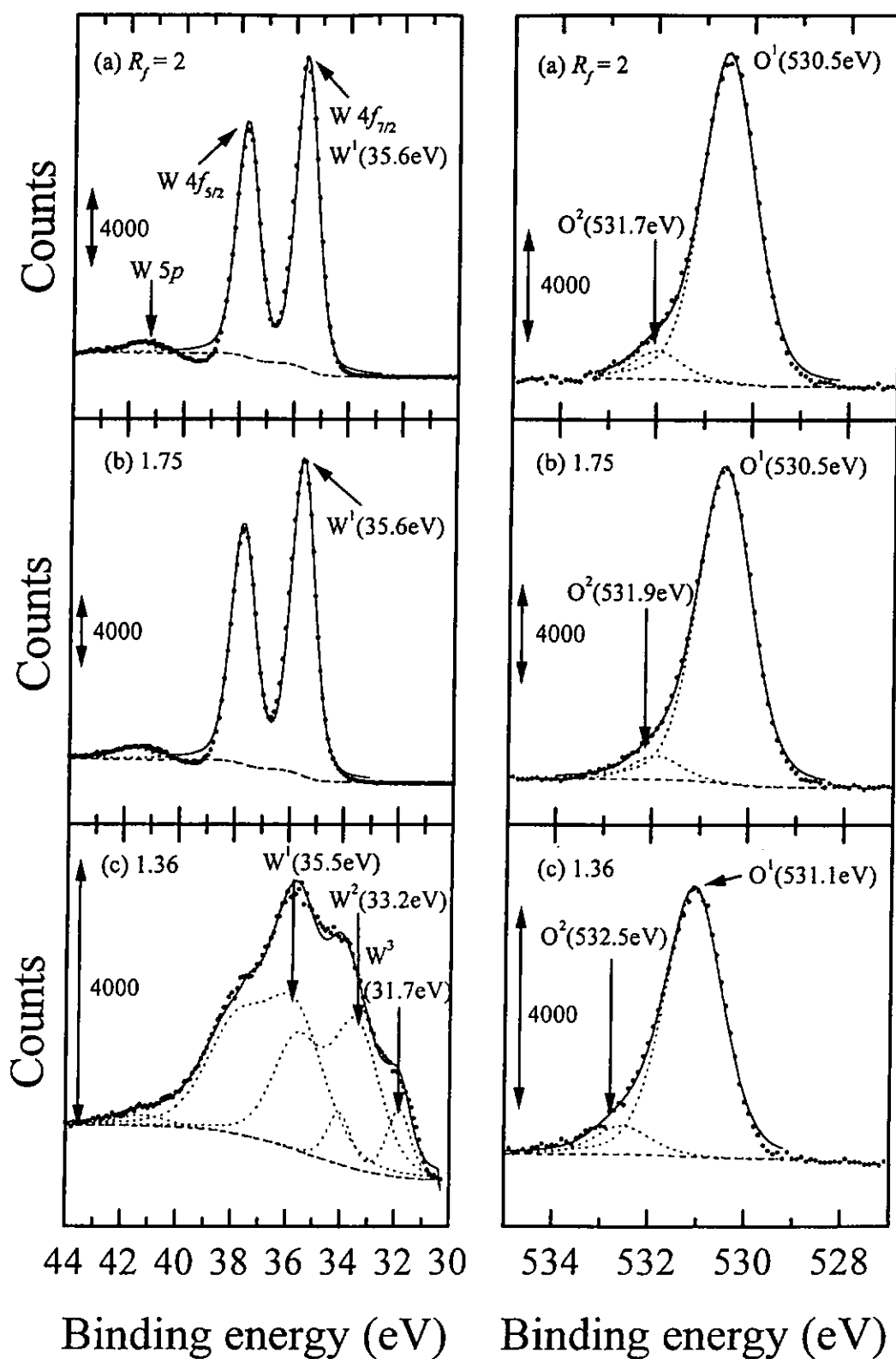


Fig. 4.1 XPS spectra of W 4f and O 1s photoelectrons of magnetron-sputtered tungsten oxide films deposited at R_f (a) 2, (b) 1.75 and (c) 1.36.

W 4f										
Sample	R_f	Atomic %	Energy (eV)	FWHM	Atomic %	Energy (eV)	FWHM	Atomic %	Energy (eV)	FWHM
MS11	2	16.9	35.6	0.95	---	---	---	---	---	---
MS12	1.75	17.3	35.6	1.038	---	---	---	---	---	---
MS13	1.36	12.8	35.5	2.56	10.8	33.2	2.01	2.6	31.7	1.04
O 1s										
Sample	R_f	Atomic %	Energy (eV)	FWHM	Atomic %	Energy (eV)	FWHM	Atomic %	Energy (eV)	FWHM
MS11	2	49.1	530.5	1.31	3.7	531.7	1.17	---	---	---
MS12	1.75	51.7	530.5	1.32	3.5	531.9	1.19	---	---	---
MS13	1.36	62.5	531.1	1.42	6.7	532.5	1.41	---	---	---
C 1s										
Sample	R_f	Atomic %	Energy (eV)	FWHM	Atomic %	Energy (eV)	FWHM	Atomic %	Energy (eV)	FWHM
MS11	2	30.4	284.5	1.614	---	---	---	---	---	---
MS12	1.75	27.4	284.5	1.894	---	---	---	---	---	---
MS13	1.36	4.6	284.5	1.894	---	---	---	---	---	---

Table 4.1 (a) The fraction, peak energy and FWHM of W^1 , W^2 and W^3 components of the W 4f spectra; O^1 and O^2 components of the O 1s spectra; and C^1 component of the C 1s spectra of the tungsten oxide films sputtered on unheated substrate at various R_f .

Sample	R_f	O/W
MS11	2	3.1
MS12	1.75	3.2
MS13	1.36	2.6

Table 4.1 (b) The O/W ratio in the films made by magnetron sputtering at various R_f .

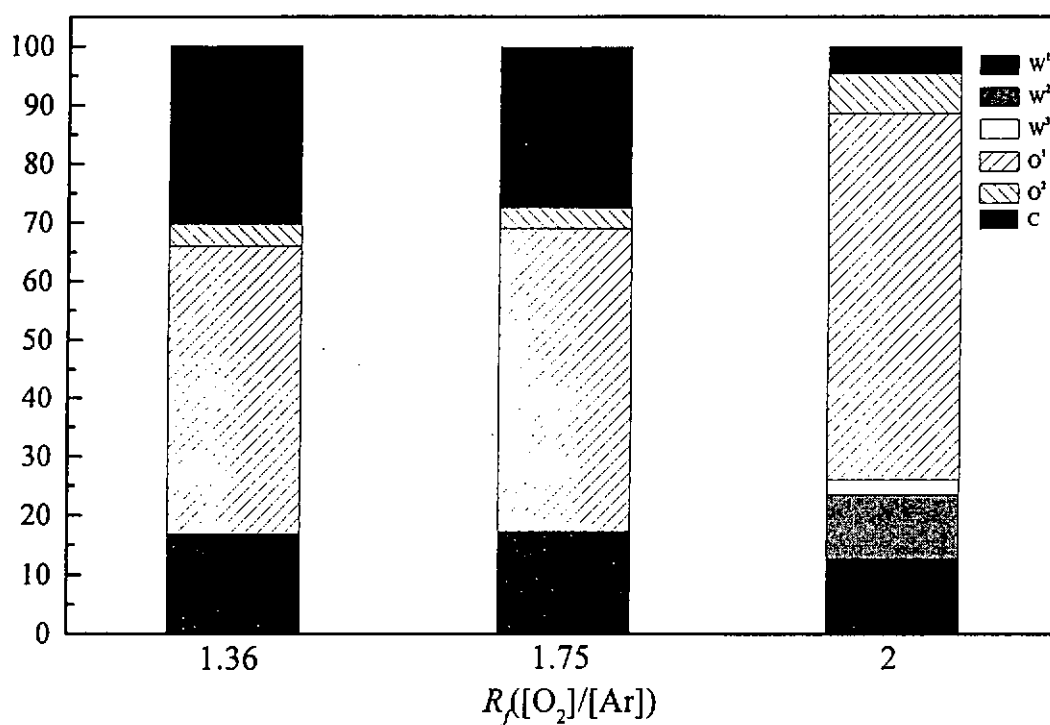


Fig. 4.2 The atomic % of W^1 , W^2 and W^3 components of the W 4f spectra; O^1 and O^2 components of the O 1s spectra; and C^1 component of the C 1s spectra of the tungsten oxide films sputtered on unheated substrate at various R_f .

4.2 Effects of Substrate Temperature on the Composition of Magnetron-Sputtered Films

The XPS spectra of W 4f and O 1s photoelectrons from the tungsten oxide films deposited at various substrate temperature are shown in Fig. 4.3. The total pressure was fixed at 10 mTorr. The spin-orbit split of the W 4f spectra of all the samples consist of mainly a W^I component. The peak position of the W 4f_{7/2} line of the W^I component is about 35.4 eV. A minor component, denoted as the W² component, is merely observable with a peak position of 34.1 - 34.3 eV. For the MS21 film ($T_s = 110$ °C), no W² component is observed. The position of the W^I and W² components, their relative fraction and FWHM are tabulated in Table 4.2(a) and Fig. 4.4.

The location of the W^I component is close to that of tungsten atoms in crystalline tungsten trioxide (WO₃), corresponding to tungsten atoms in the W^{VI} state. The W² peak could be assigned to the W atoms in an environment analogous to that in the structure of W₁₈O₄₉, in which the tungsten atoms having valence of W^{II} or W^{IV} [Sabbatini *et al.* 1983]. The reason for the W₁₈O₄₉-like structure to appears in the samples with $T_s \geq 300$ °C may be due to thermal desorption of W-O bonds and the subsequent escape of oxygen [Ageev and Ionov 1966]. The appearance of such a weak W² component implies that oxygen is slightly deficient in the films whereas the film structure is very close to that of crystalline WO₃.

The photoelectron spectra O 1s are fitted by two components, denoted as components O¹ and O². The peak position of O¹ component is close to 530.6 eV. The

O² component is a small, which peak position varies between 531.4 and 531.9 eV, and is attributed to the oxygen atoms in other WO_x structures, with $x < 3$.

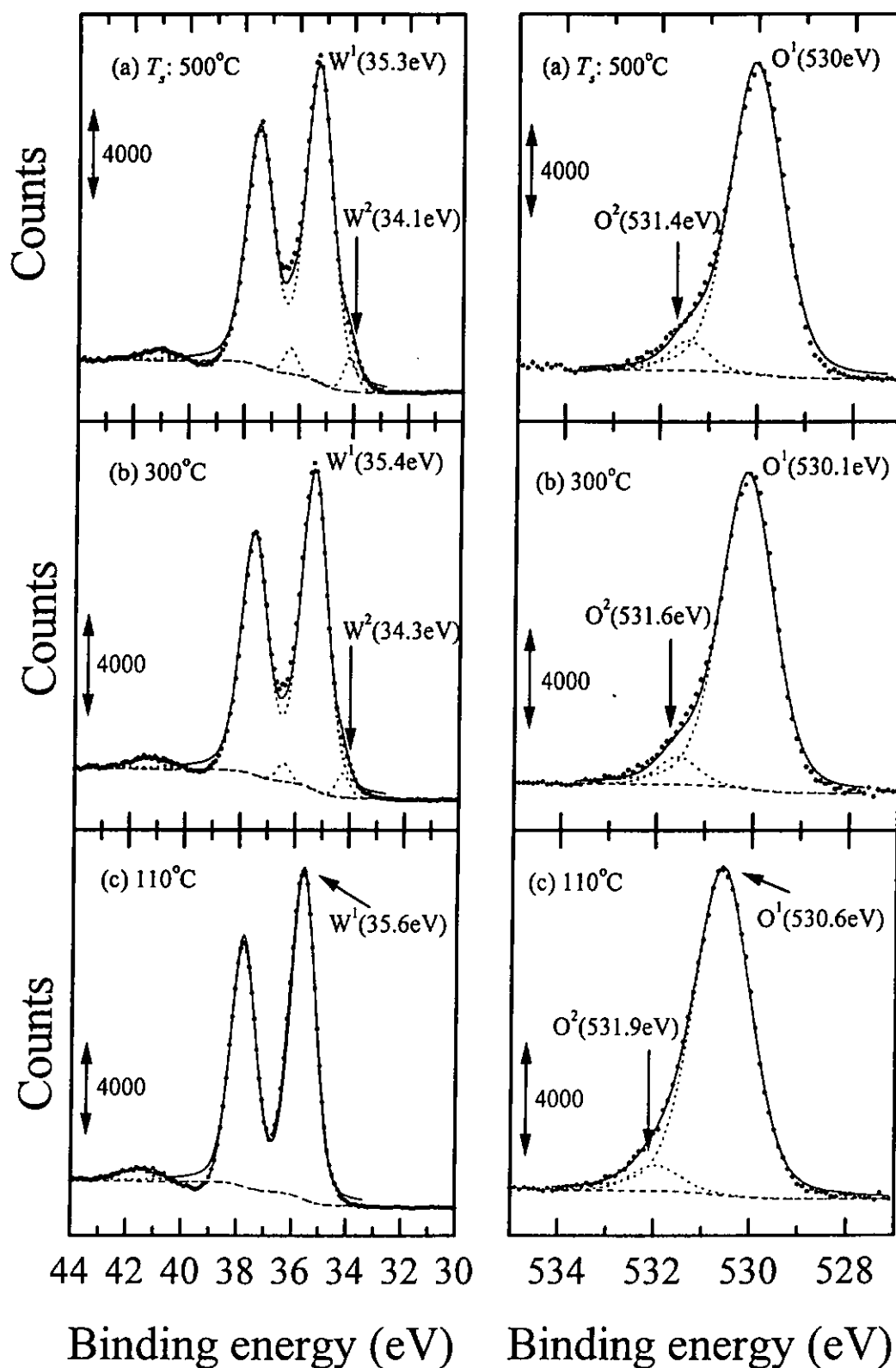


Fig. 4.3 XPS spectra of W 4f and O 1s photoelectrons of magnetron-sputtered tungsten oxide films deposited at fixed $R_f = 2$, and various T_s (a) 500 °C, (b) 300 °C and (c) 110 °C.

W 4f					W		
Sample	T_s (°C)	Atomic %	Energy (eV)	FWHM	Atomic %	Energy (eV)	FWHM
MS21	110	16.4	35.6	1.04	---	---	---
MS22	300	16.2	35.4	1.15	0.6	34.3	0.54
MS23	500	17.3	35.3	1.17	0.9	34.1	0.56
O 1s					O ²		
Sample	T_s (°C)	Atomic %	Energy (eV)	FWHM	Atomic %	Energy (eV)	FWHM
MS21	110	52.6	530.6	1.39	3.7	531.9	1.19
MS22	300	52.0	530.1	1.3	3.4	531.6	0.97
MS23	500	53.6	530	1.29	3.8	531.4	0.94
C 1s					---	---	---
Sample	T_s (°C)	Atomic %	Energy (eV)	FWHM	---	---	---
MS21	110	27.3	284.5	1.45	---	---	---
MS22	300	27.8	284.5	1.34	---	---	---
MS23	500	24.3	284.5	1.35	---	---	---

Table 4.2 (a) The fraction, peak energy and FWHM of W^1 and W^2 components of the W 4f spectra; O^1 and O^2 components of the O 1s spectra; and C^1 component of the C 1s spectra of the films deposited by magnetron sputtering at various T_s .

Sample	T_s (°C)	O/W
MS21	110	3.4
MS22	300	3.3
MS23	500	3.2

Table 4.2 (b) The O/W ratio in the films deposited by magnetron sputtering at various T_s .

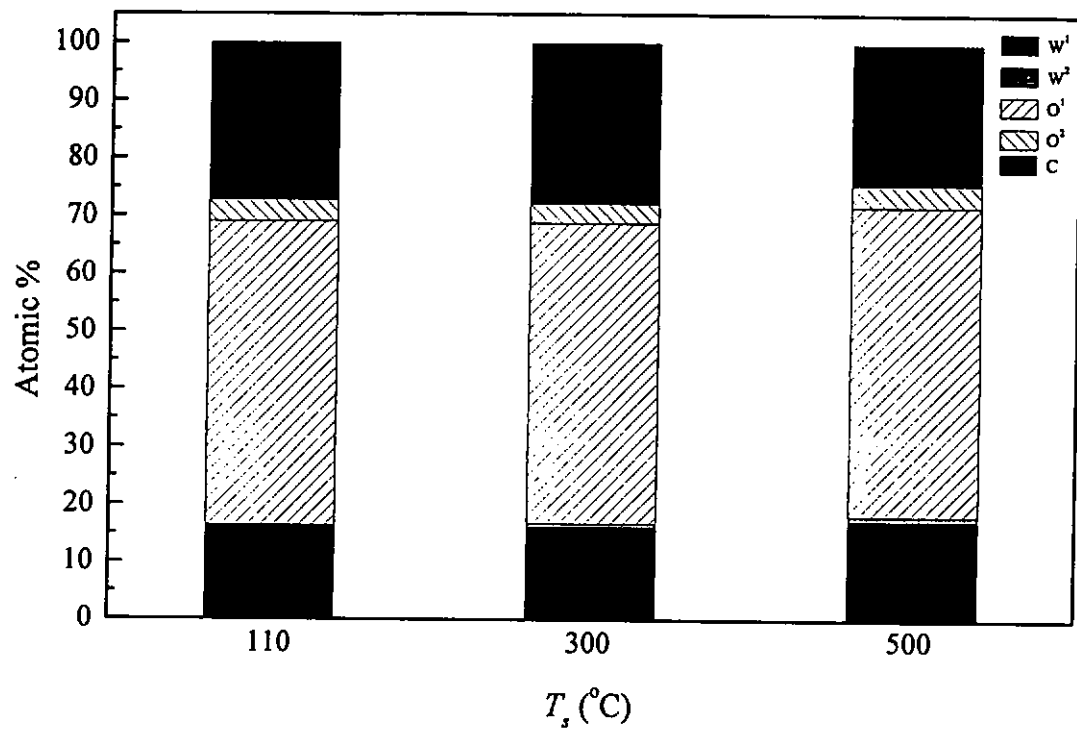


Fig. 4.4 The atomic % of W^1 and W^2 components of the $W 4f$ spectra; O^1 and O^2 components of the $O 1s$ spectra; and C^1 component of the $C 1s$ spectra of the films deposited by magnetron sputtering at various T_s .

4.3 Effects of Oxygen Partial Pressure on the Composition of Thermally Evaporated Films

The XPS spectra of W 4f, and O 1s photoelectrons from the tungsten oxide films deposited on unheated substrates at various oxygen partial pressure are shown in Fig. 4.5. The W 4f spectra of all the samples consist of a W¹ component and a W² component. The W¹ component strong, which is a doublet containing a W 4f_{7/2} line and W 4f_{5/2} line. The peak position of the W 4f_{7/2} line is about 35.5 eV. The W² component is weak, containing a W 4f_{7/2} peak located at 34.1 - 34.5 eV. The peak position of the W 4f_{7/2} lines of the W¹ and W² components, their relative fraction and FWHM are tabulated in Table 4.3(a) and Fig. 4.6.

The location of the W 4f_{7/2} peak of the W¹ component is close to that of tungsten atoms in crystalline tungsten trioxide (WO₃), which have a valence of +6 (W^{VI}). The W² component is assigned to those W atoms in the environment analogous to the structure of W₁₈O₄₉, in which the tungsten atoms have valence of W^{II} or W^{IV} [Sabbatini *et al.* 1983]. The appearance the W² component implies that oxygen is deficient in the films. It is possibly due to the oxidation of the tungsten boat [Ptushinskii and Chuikov 1961, Schissel and Trulson 1964]. The fraction of W² component is rather small, so that the oxygen deficiency is not significant.

The photoelectron spectra O 1s are fitted by two components, denoted as components O¹ and O². The peak position of O¹ component is close to 530.6 eV. The O² component is smaller, which peak position varies between 531.4 and 531.9 eV, and is attributed to the oxygen atoms incorporated into WO_x atomic network. The

atomic fraction of O² of the thermally evaporated samples is higher than that of magnetron-sputtered samples. The O to W ratio in the films is as high as 3.4 to 3.7. This is due to rough surface, which provides much large effective surface area for the surface sorption of more oxygen-containing species.

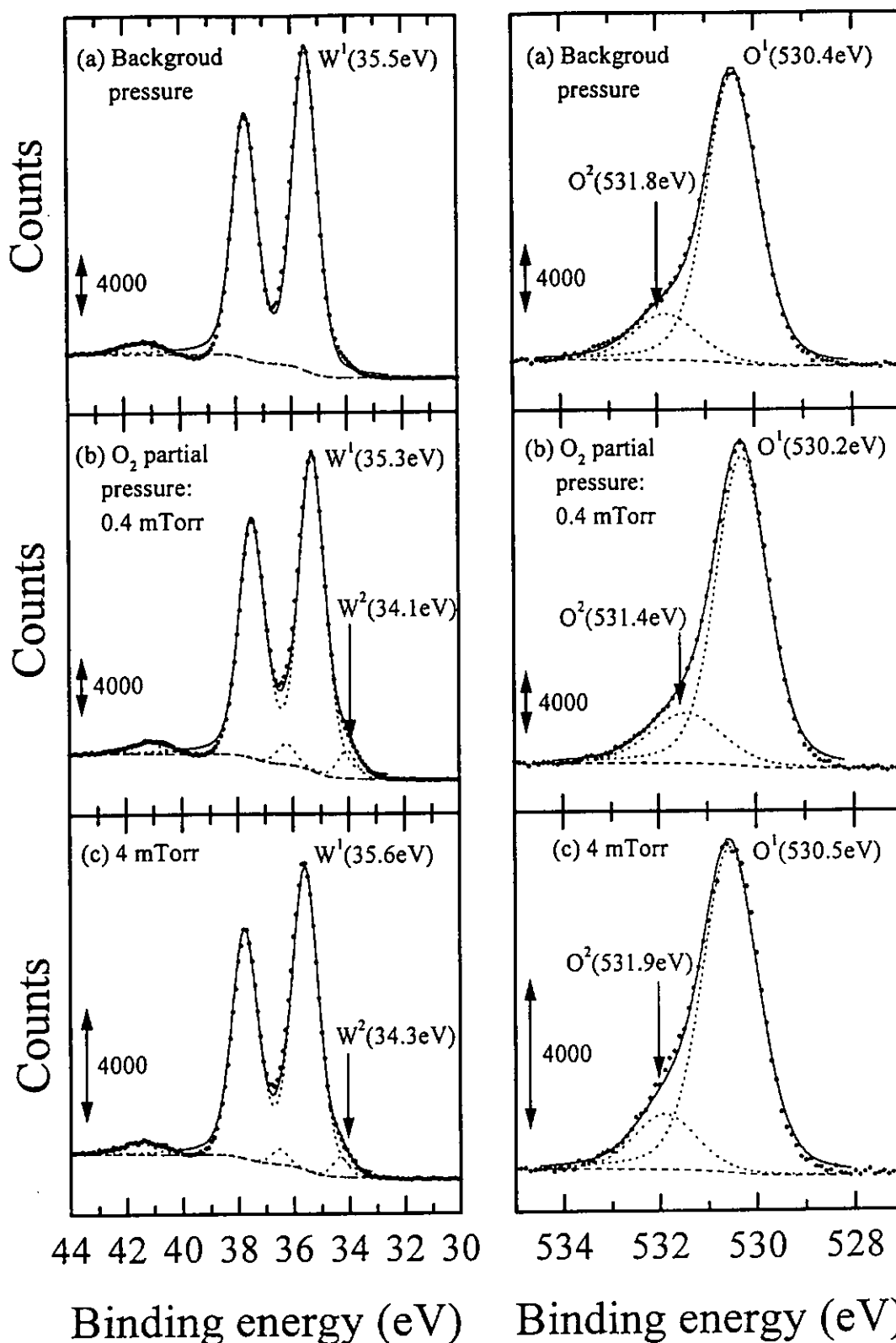


Fig. 4.5 XPS spectra of W 4f and O 1s photoelectrons of thermally evaporated tungsten oxide films deposited on unheated substrates at various oxygen partial pressures: (a) Background pressure of 2×10^{-6} Torr, (b) 0.4, (c) 4, (d) 6 and (e) 10 mTorr.

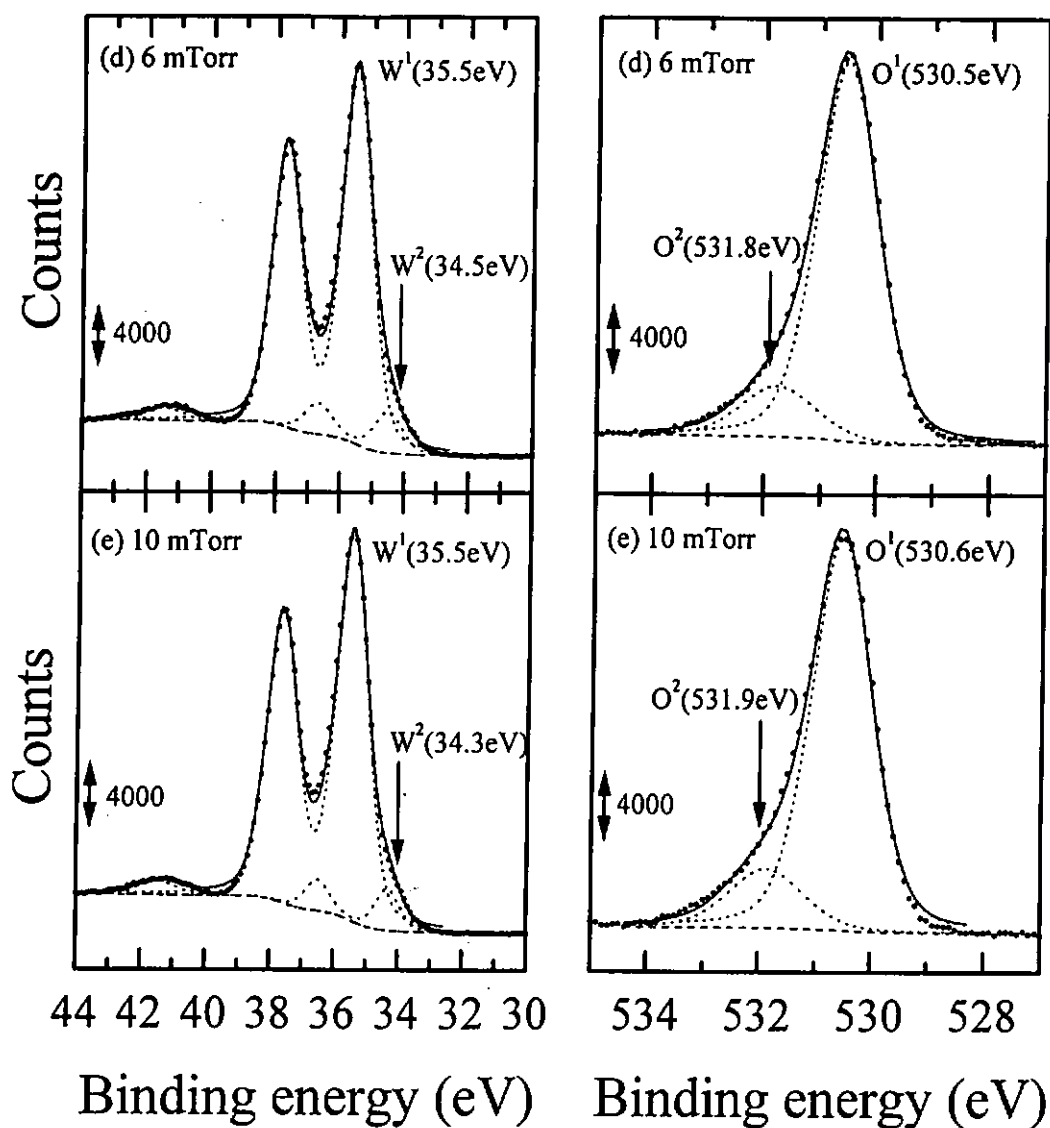


Fig. 4.5 XPS spectra of W 4f and O 1s photoelectrons of thermally evaporated tungsten oxide films deposited on unheated substrates at various oxygen partial pressures: (d) 6 and (e) 10 mTorr.

W 4f					W		
Sample	O ₂ partial pressure (mTorr)	Atomic %	Energy (eV)	FWHM	Atomic %	Energy (eV)	FWHM
TE1	Background Pressure 2×10 ⁻⁶ Torr	13.8	35.5	1.05	---	---	---
TE2	0.4	14.4	35.3	1.10	0.9	34.1	0.74
TE3	4	13.0	35.6	1.12	0.5	34.3	0.68
TE4	6	15.6	35.5	1.1	1.6	34.5	1.02
TE5	10	14.9	35.5	1.14	1.3	34.3	0.89

O 1s					O		
Sample	O ₂ partial pressure (mTorr)	Atomic %	Energy (eV)	FWHM	Atomic %	Energy (eV)	FWHM
TE1	Background Pressure 2×10 ⁻⁶ Torr	41.3	530.4	1.26	8.2	531.8	1.54
TE2	0.4	45.4	530.2	1.24	10.4	531.4	1.77
TE3	4	40.9	530.5	1.37	7.7	531.9	1.50
TE4	6	49.5	530.5	1.29	8.1	531.8	1.56
TE5	10	48.3	530.6	1.29	8.9	531.9	1.56

C 1s					C		
Sample	O ₂ partial pressure (mTorr)	Atomic %	Energy (eV)	FWHM	Atomic %	Energy (eV)	FWHM
TE1	Background Pressure 2×10 ⁻⁶ Torr	36.8	284.5	1.498	---	---	---
TE2	0.4	28.9	284.5	1.59	---	---	---
TE3	4	37.9	284.5	1.24	---	---	---
TE4	6	25.2	284.5	1.72	---	---	---
TE5	10	26.7	284.5	1.48	---	---	---

Table 4.3 (a) The fractions, peak energies and FWHM of W¹ and W² components of W 4f spectra; O¹ and O² components of the O 1s spectra; and C¹ component of the C 1s spectra of the films made by thermal evaporation at various O₂ partial pressures.

Sample (on ITO coated glass)	O ₂ pressure (mTorr)	O/W
TE1	Bkg.	3.6
TE2	0.4	3.7
TE3	4	3.6
TE4	6	3.4
TE5	10	3.5

Table 4.3 (b) The O/W ratio of the films made by thermal evaporation at various O₂ partial pressures.

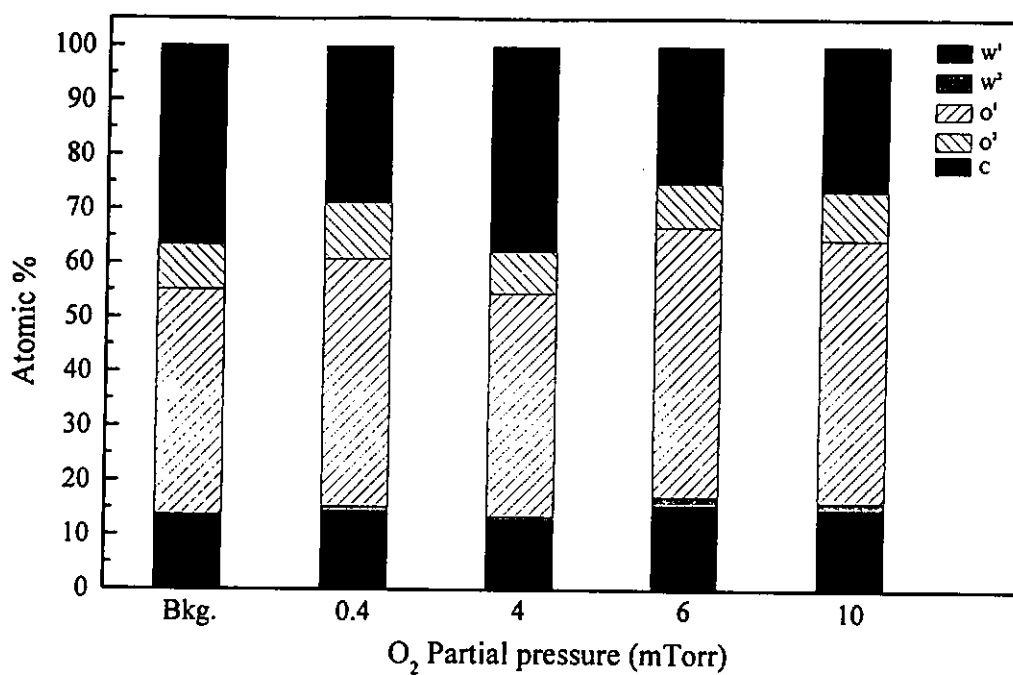


Fig. 4.6 The atomic % of W¹ and W² components of W 4f spectra; O¹ and O² components of the O 1s spectra; and C¹ component of the C 1s spectra of the films made by thermal evaporation at various O₂ partial pressures.

4.4 XPS Analysis of WO₃ Films after Coloring/Bleaching Cycles

Fig. 4.7(a), (b) and (c) show the W 4*f* and O 1*s* photoelectron spectra of magnetron sputtered samples prepared at $R_f = 2$ on unheated substrate, experienced no coloring/bleaching (c/b) cycles, 1000 and 10000 c/b cycles, respectively.

The W 4*f* spectrum of sample MS11 before coloring/bleaching has been discussed in Section 4.1, and the results are summarized briefly as follows for the convenience of comparison. As shown in Fig. 4.7(a), the W 4*f* spectrum of sample MS11 is mainly constructed of a single component, with the W 4*f*_{7/2} line having a peak energy at 35.6 eV. This corresponds to some tungsten atoms in the structure analogous to the crystalline WO₃ structure. Fig. 4.7(a) shows that the peak energy of the major component O^I is at 530.5 eV, consistent with the O atoms located in the crystalline structure.

Fig. 4.7(b) shows the W 4*f* and O 1*s* photoelectron spectra of sample MSC1 after experiencing 1000 c/b cycles. For sample MSC1, the spectrum contains only one component, denoted as W^I, with the W 4*f*_{7/2} appears at 35.3 eV. This peak energy is close to that of tungsten trioxide phase (WO₃) corresponding to the tungsten atoms having a valence of six, (W^{VI}). The film is at a nearly completely bleached state so only such a W^I component is found.

Fig. 4.7(c) shows the W 4*f* and O 1*s* photoelectron spectra of sample MSC2, after experiencing 10000 times of c/b cycles. The W 4*f* consists of two components, W^I and W². W^I component has a W 4*f*_{7/2} peak at 35.3 eV, the same as that of MSC1,

respectively those tungsten atoms in the WO_3 -like network. The $\text{W } 4f_{7/2}$ peak of the W^2 component is found to locate at 33.4 eV, and the component is more appropriate to the tungsten atoms in the W^{IV} state. Tungsten atoms at this reduced state are generated because film contains some Li^+ ions have been irreversibly accumulated in the films after quite a large number of c/b cycles.

The O 1s spectra of MSC1 and MSC2 are significantly difference from that of MS11. The O 1s spectra of MSC1 and MSC2 are asymmetric. Each of them are fitted by three components, O^1 , O^2 and O^3 . The peak position of the O^1 component is at 530.6 eV. The O^1 component is thus attributed to the oxygen atoms combining with tungsten atoms analogous to those in the WO_3 structure. The O^2 component is weaker, having a peak position at 531.1 - 531.7 eV, and is assigned to the oxygen atoms in the WO_x -like ($x < 3$) atomic structure in the films. The weaker O^3 component is ever weaker, with peak lying between 532.5 and 532.8 eV. Since the peak positions of O 1s electrons from LiClO_4 and H_2O molecules are close to 533.4 eV and 533.2 eV respectively, the O^3 component can be attributed to the oxygen atoms from these molecules. Obviously, the concentration of O^2 and O^3 increases with increasing number of coloring/bleaching cycles (Table 4.4).

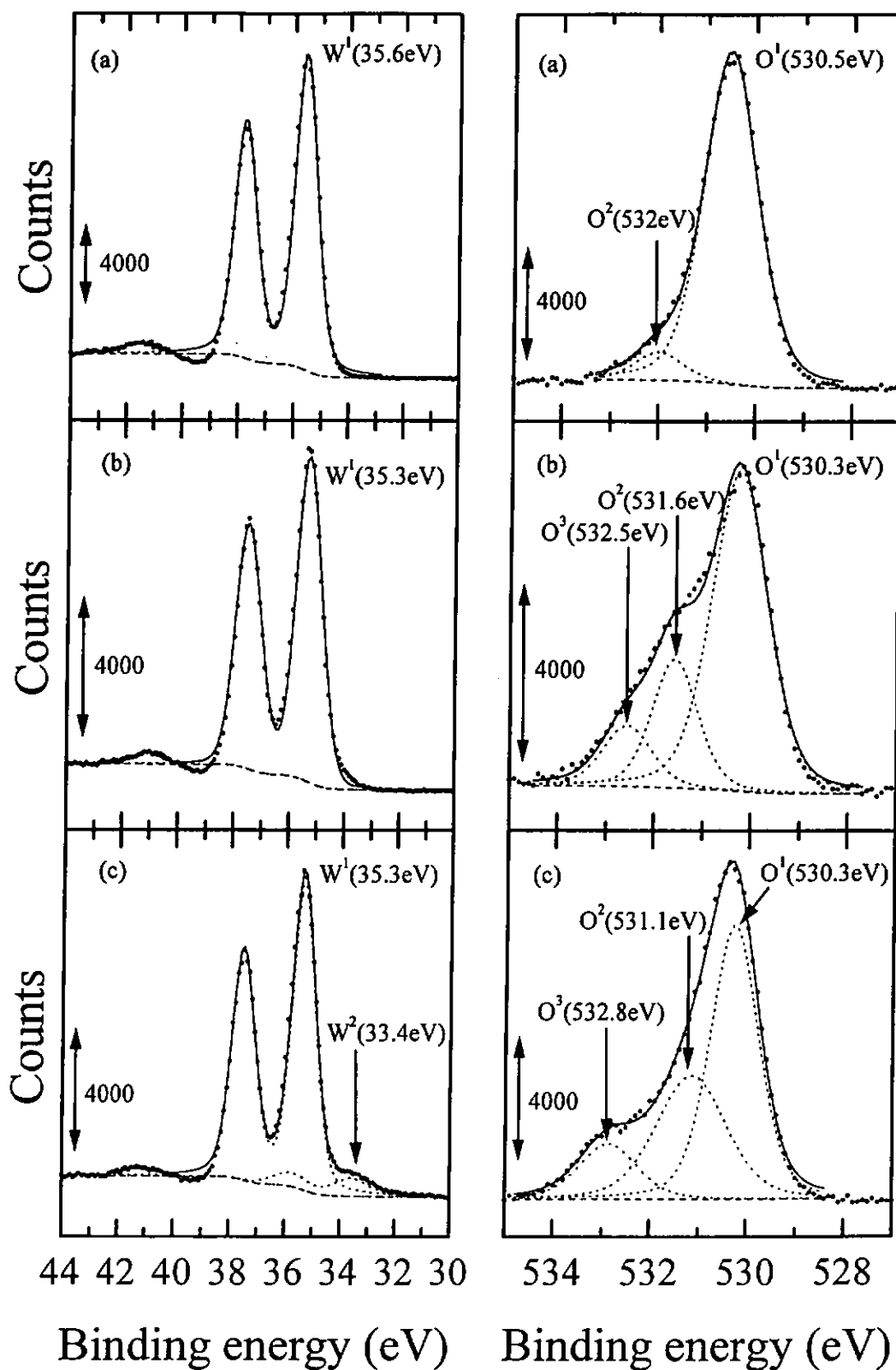


Fig. 4.7 XPS spectra of W 4f and O 1s photoelectrons of magnetron-sputtered samples experienced in various times of c/b cycles
 (a) MS11, before experiencing c/b process,
 (b) MSC1, experienced 1000 times c/b cycles,
 (c) MSC2, experienced 10000 times c/b cycles.

W 4f		W 4f			W 4f			W 4f		
Sample	c/b cycles	Atomic %	Energy (eV)	FWHM	Atomic %	Energy (eV)	FWHM	Atomic %	Energy (eV)	FWHM
MS11	ad	16.9	35.6	0.95	---	---	---	---	---	---
MSC1	1000	9.3	35.3	1.10	---	---	---	---	---	---
MSC2	10000	10.6	35.3	0.99	0.9	33.4	1.51	---	---	---
O 1s		O 1s			O 1s			O 1s		
Sample	c/b cycles	Atomic %	Energy (eV)	FWHM	Atomic %	Energy (eV)	FWHM	Atomic %	Energy (eV)	FWHM
MS11	ad	49.1	530.5	1.31	3.7	531.7	1.17	---	---	---
MSC1	1000	28.1	530.3	1.36	9.1	531.6	1.2	4.7	532.5	1.12
MSC2	10000	34.0	530.3	1.18	22.3	531.1	1.71	8.3	532.8	1.42
C 1s		C 1s			C 1s			C 1s		
Sample	c/b cycles	Atomic %	Energy (eV)	FWHM	Atomic %	Energy (eV)	FWHM	Atomic %	Energy (eV)	FWHM
MS11	ad	30.4	284.5	1.61	---	---	---	---	---	---
MSC1	1000	41.0	284.5	1.70	5.0	288.1	1.71	---	---	---
MSC2	10000	18.4	284.5	1.49	0.7	288.3	1.15	---	---	---
Li 1s		Li 1s			Li 1s			Li 1s		
Sample	c/b cycles	Atomic %	Energy (eV)	FWHM	Atomic %	Energy (eV)	FWHM	Atomic %	Energy (eV)	FWHM
MS11	ad	---	---	---	---	---	---	---	---	---
MSC1	1000	1.5	56.1	0.27	---	---	---	---	---	---
MSC2	10000	2.1	56.1	0.37	---	---	---	---	---	---
Cl 2p		Cl 2p			Cl 2p			Cl 2p		
Sample	c/b cycles	Atomic %	Energy (eV)	FWHM	Atomic %	Energy (eV)	FWHM	Atomic %	Energy (eV)	FWHM
MS11	ad	---	---	---	---	---	---	---	---	---
MSC1	1000	1.1	207.7	1.21	0.5	198.7	1.21	---	---	---
MSC2	10000	1.6	208.3	1.10	1.2	198.5	1.10	---	---	---

Table 4.4 The fractions, peak energies and FWHM of W¹ and W² components of W 4f spectra; O¹, O² and O³ components of the O 1s spectra; C¹ and C² component of the C 1s spectra; Li¹ components of Li 1s spectra; and Cl¹ and Cl² components of Cl 2p spectra of the magnetron-sputtered films undergone various c/b cycles.

XPS depth profile analysis of sample MS11, MSC1 and MSC2 before and after coloring/bleaching (c/b) cycles was carried out. Fig. 4.8(a) to (c) show the measured O, W, C, Li, and Cl concentrations as functions of sputtering time of an as-deposited (ad) sample before imposing coloring/bleaching (c/b) cycles, after 1000 and 10000 c/b cycles, respectively.

Fig. 4.8(a) shows the results of sample MS11, before experiencing c/b cycles. Before ion sputtering (zero sputtering time), the O/W ratio is 3.1, which is close to crystalline WO_3 phase. The atomic concentrations of O and W increase after sputtering by 200 eV Ar^+ ions for 5 min (the data points shown at sputtering time = 5 min), because of the removal of C sorbed at the film surface. With increasing sputtering time, by 2k eV Ar^+ ions and 10 min per step, the O/W concentration drops and finally stabilized at 1.5 (Fig. 4.12). This implies that oxygen in the film is preferentially sputtered by ion bombardment.

Fig. 4.8(b) and (c) show the XPS depth profiles of sample MSC1 and MSC2, after experiencing 1000 and 10000 times coloring/bleaching cycles respectively. In each cycle, Li^+ ions are forced into and extracted out of the film. It is therefore of interest to investigate whether there is irreversible accumulation of Li^+ ions such that the long-term stability of the electrochromic properties of the film could be affected. The O/W ratio behaves similarly with increasing sputtering time. First, a high O/W ratio and Li^+ concentration at the film surface before sputtering was observed. This value is as high as 5, exceeding that of the film before experiencing c/b cycles. This is because some LiClO_4 and $\text{C}_4\text{H}_6\text{O}_3$ molecules would adhere to the film surface after the film is removed from the electrolyte.

Li^+ ion accumulation are detected in samples MSC1 and MSC2 (Fig. 4.8(b) and (c)). Peak values of Li^+ concentration are recorded for MSC2 after sputtering times of 15 and 25 min.

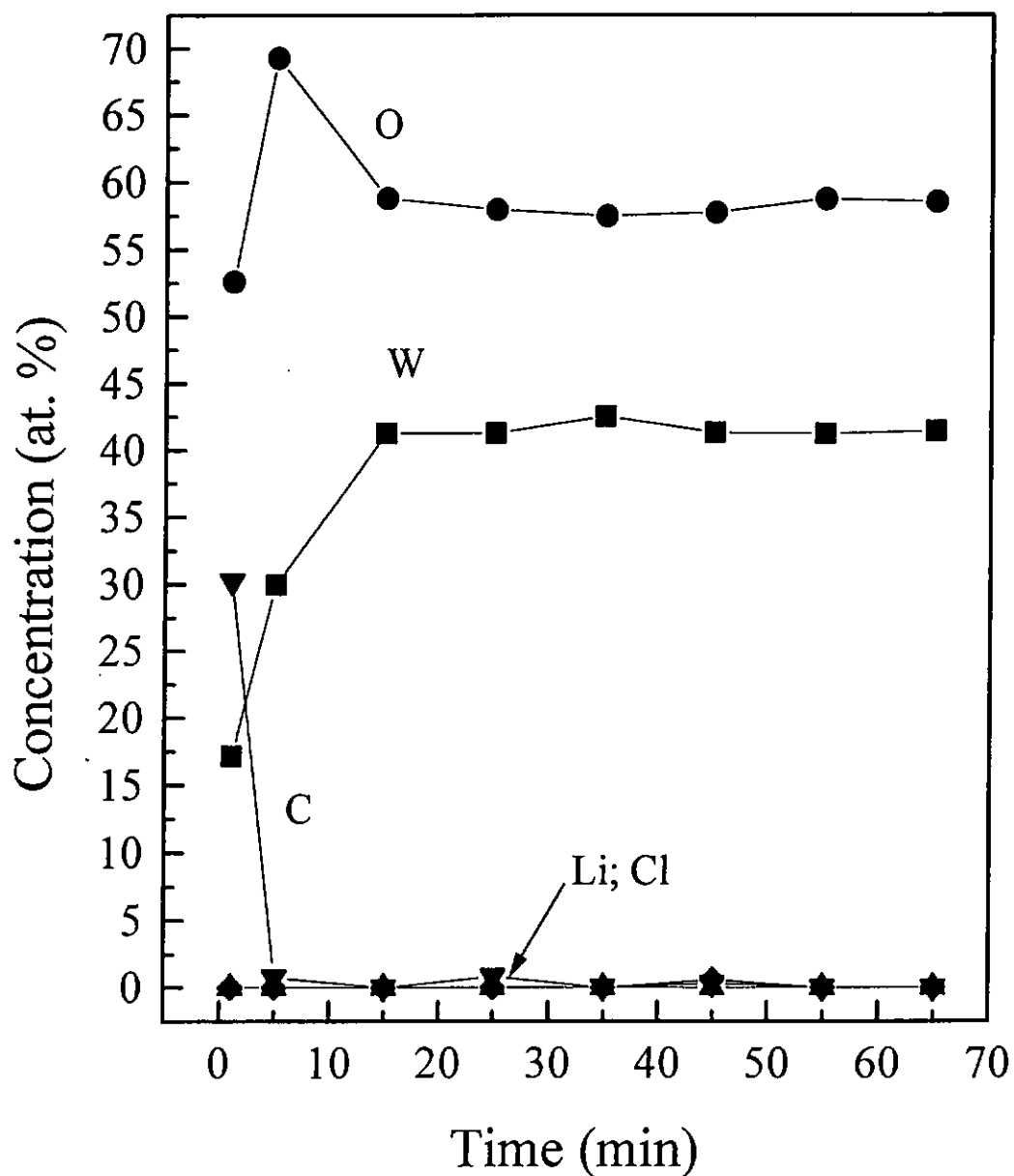


Fig. 4.8 (a) The measured W (■), O (●), C (▼), Li (▲) and Cl (◆) concentration as functions of sputtering time for sample MS11, before experiencing c/b cycles.

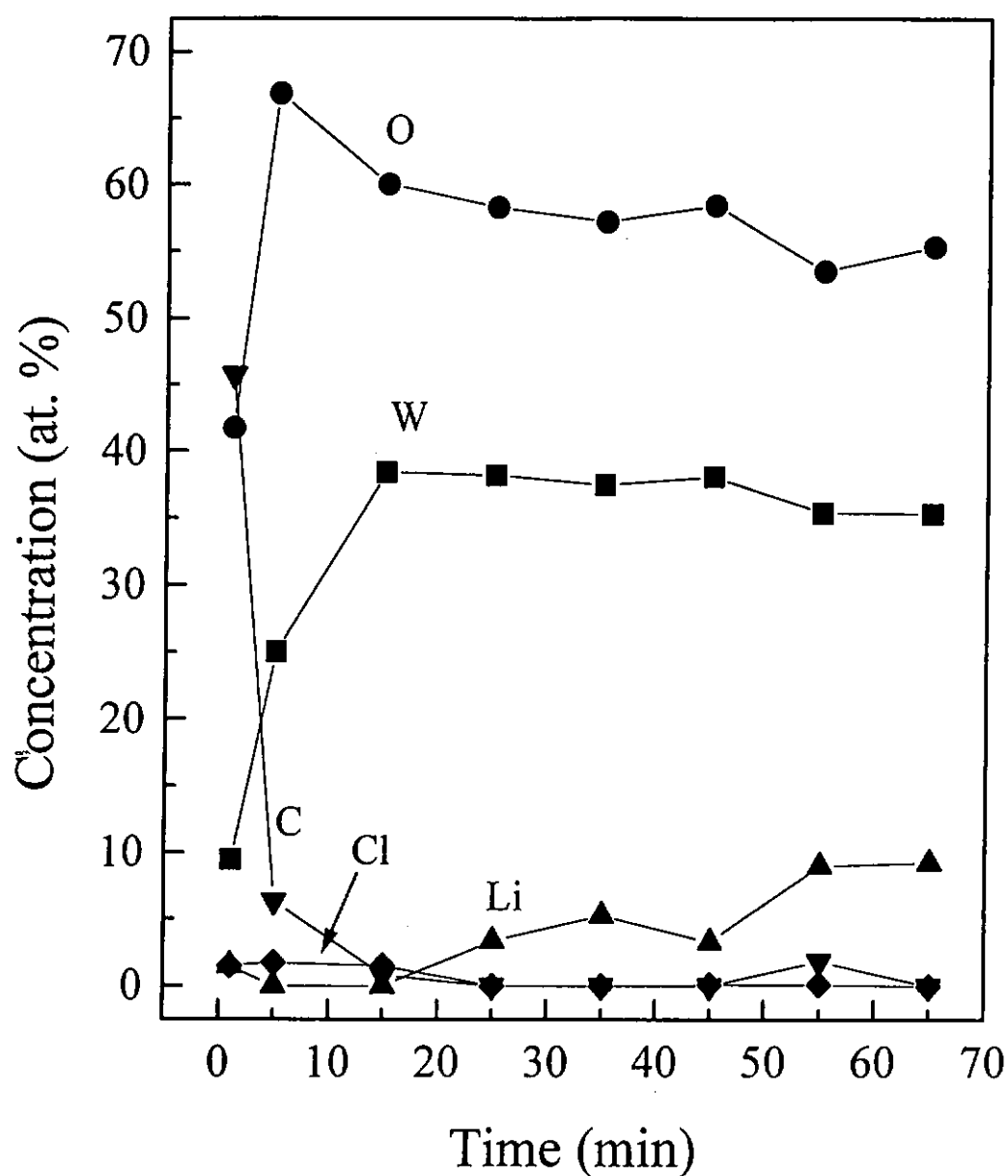


Fig. 4.8 (b) The measured W (■), O (●), C (▼), Li (▲) and Cl (◆) concentration as functions of sputtering time for sample MSC1, after experiencing 1000 c/b cycles.

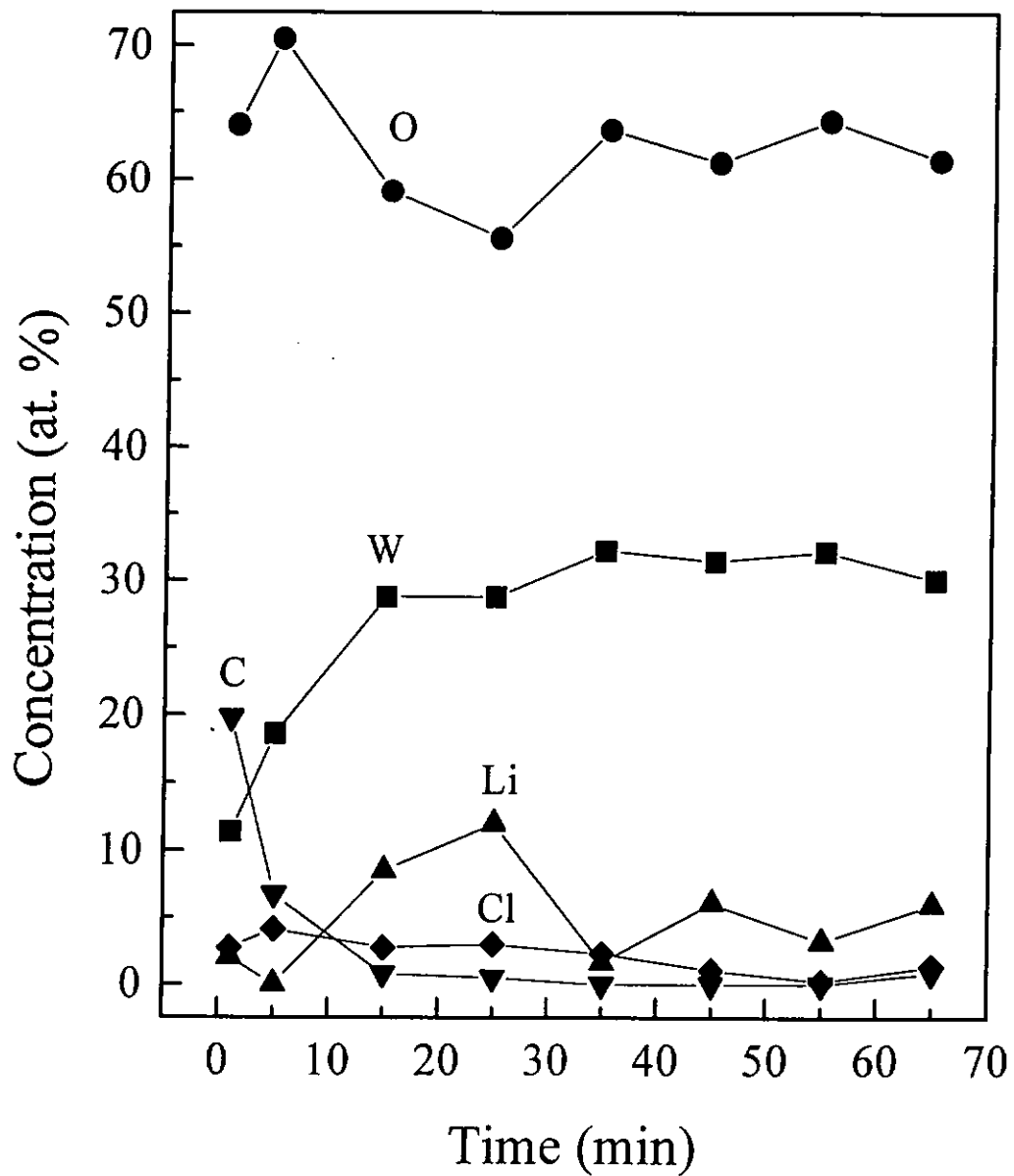


Fig. 4.8 (c) The measured W (■), O (●), C (▼), Li (▲) and Cl (◆) concentration as functions of sputtering time for sample MSC2, after experiencing 10000 c/b cycles.

4.5 Preferential Sputtering of Oxygen by Ion Irradiation

4.5.1 *Effects of Ion Bombardment on Magnetron-Sputtered Films on Unheated Substrate*

Discussions in Section 4.1 - 4.3 are based on the XPS data collected before cleaning the surface by ion beam. Therefore the C concentration seems to be large. In order to remove the surface contaminant and to get the depth profile of the film composition. An energetic ion beam was used to sputter the sample. However, this surface treatment may lead to preferential sputtering of some elements, such that the composition information extracted from these spectra may deviate from the real composition of the film. In this section, XPS data collected before surface cleaning and subsequential ion sputtering are presented and discussed. Results show some limitation on investigating the depth profiles of the composition of tungsten oxide films by using ion sputtering. Ion sputtering is usually used XPS analysis for removing surface contamination and sputtering for depth profile analysis.

Fig. 4.9(a) shows the W 4f and O 1s photoelectron spectra of a magnetron sputtered sample deposited on unheated substrate at $R_f = 2$, collected before surface cleaning. The spectrum consists mainly of a single component, with a W 4f_{7/2} peak at 35.6 eV, indicating at this moment the O to W ratio is about 3, and the two kinds of elements are combined in the form analogous to the WO₃ structure.

The film surface was then sputtered with 200 eV Ar⁺ for 5 min, with the attempt to remove the carbon-containing species absorbed on the film surface. The

low ion energy and short sputtering period were selected with the intention of minimizing preferential sputtering possibly induced. Fig. 4.9(b) shows the W 4f and O 1s spectra recorded after the sputtering process. One immediately finds that two new components, W² and W³, emerge. Their W 4f_{7/2} peaks are located at 34.3 and 35.8 eV, respectively, roughly falling into the range of that of tungsten atoms having valences of +4 and +2 (W^{IV} and W^{II} states) [Sabbatini *et al.* 1983]. This implies that the oxygen content at this level is less than that in the crystalline WO₃ structure, because tungsten atoms having some neighbouring oxygen vacancies are supposed to have valences lower than +6. The oxygen deficiency may be due to the nonuniformity of elemental distribution in the film along the substrate normal direction, or preferential sputtering of oxygen by ion beam bombardment during the sputtering process. The shortage of oxygen after sputtering is presented by a lower O/W ratio of 2.5 (Table 4.5).

The film was further sputtered by an additional sputtering process, in which Ar⁺ ions with a much higher energy of 2 keV was used. The sputtering process lasted for a layer period of 30 min. The W 4f spectrum shown in Fig. 4.9(c) shows that in addition to the presence of W² and W³ components, a new component W⁴ grows with a W 4f_{7/2} peak appearing at 31.2 eV, such that the W⁴ component is most reasonable to be assigned to metallic tungsten. This indicates that the oxygen deficiency detected after this sputtering process is even more remarkable. The O/W drops further to 1.5 (Table 4.5). The O² component almost disappears (Fig. 4.9(c)). It is noticed that for a tungsten oxide film with such a low oxygen content, the film should not be transparent. However, it is because the film is transparent just after it is fabricated, this leads one to believe that the low O/W ratio recorded after ion

bombardment should come from preferential sputtering of oxygen during the sputtering process. We thus conclude that ion beam sputtering is not a good technique to work with XPS analysis in probing the compositional depth profile of tungsten oxide films, as it addressed additional alternation of the original film composition via preferential removal of oxygen. For further confirmation of this viewpoint, we carried out some observations described in the following sections.

	W ¹ (at. %)	W ² (at. %)	W ³ (at. %)	W ⁴ (at. %)	O ¹ (at. %)	O ² (at. %)	C (at. %)	O/W (at. %)
As deposited	16.9	---	---	---	49.1	3.7	30.4	3.1
200 eV, for 5 min (5th min)	13.4	9.0	6.2	---	68.5	2.2	0.8	2.5
2 k eV, for 30 min (35th min)	12.9	10.4	8.8	8.1	57.5	2.3	---	1.5

Table. 4.5 Atomic concentration of tungsten associated with the W¹, W², W³ and W⁴ components, and the oxygen atoms associated with the O¹ and O² components for the magnetron-sputtered tungsten oxide films deposited on unheated substrate at $R_f = 2$.

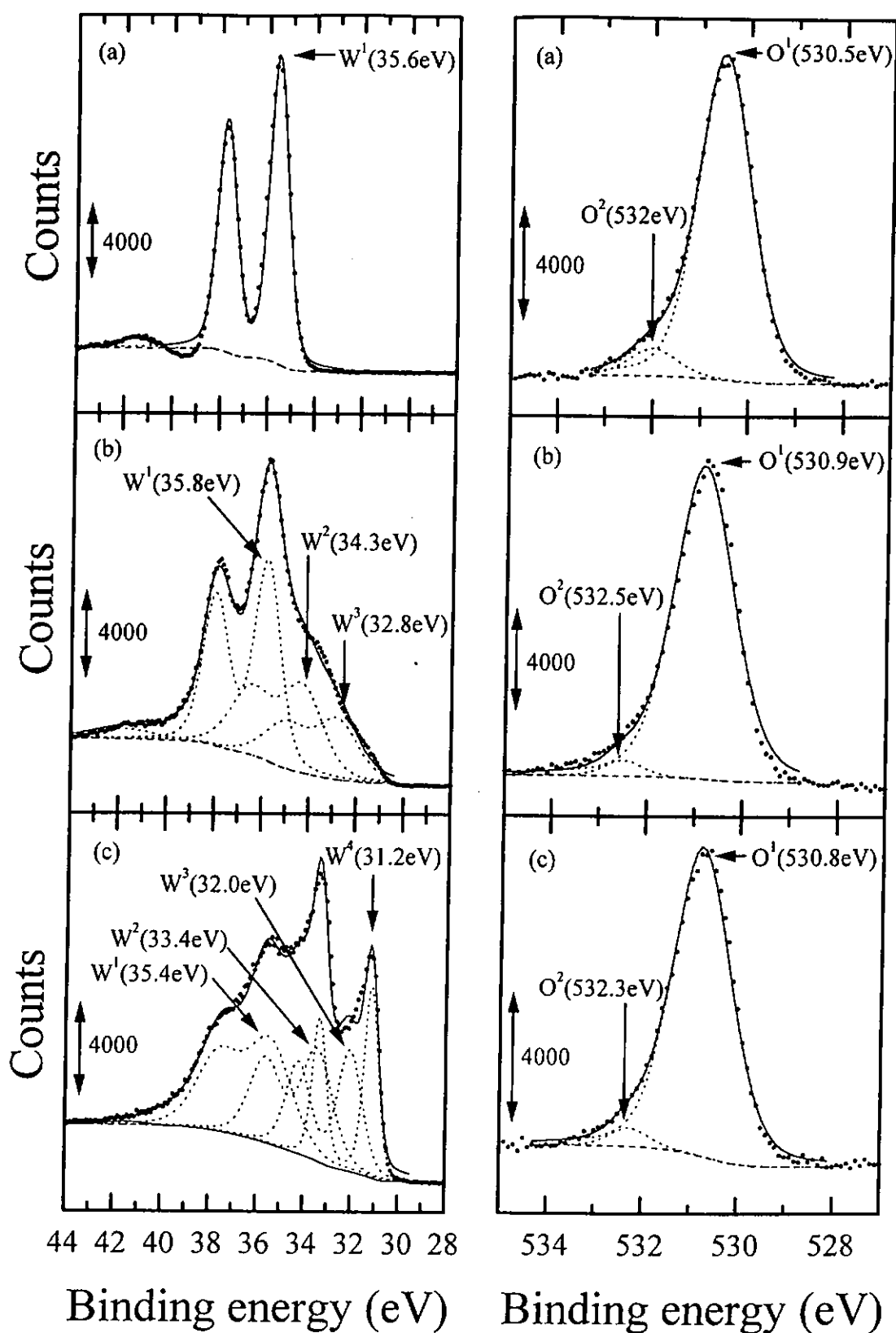


Fig. 4.9 The W 4f and O 1s photoelectron spectra of magnetron-sputtered tungsten oxide film deposited on unheated substrate at $R_f = 2$.
 (a) Before surface cleaning,
 (b) After surface cleaning by 200 eV Ar^+ ions for 5 minutes,
 (c) After surface cleaning by 2k eV Ar^+ ions for 30 minutes.

4.5.2 Effects of Ion Bombardment on Magnetron-Sputtered Films on Heated Substrate

Fig. 4.10(a) shows the W 4f and O 1s spectra from the as-deposited surface (before ion sputtering) of a magnetron-sputtered tungsten oxide film prepared at substrate temperature $T_s = 500\text{ }^{\circ}\text{C}$. X-ray diffraction data show that the film has been crystallized, and the results will be discussed in Section 5.2. The W 4f spectrum is mainly constructed of a single line associated with W^{VI} tungsten atoms. The O 1s spectrum contains mainly a O^{I} component, and a weak O^{II} component. The O/W ratio is 3.2, which is very close to 3 of the stoichiometric WO_3 phase. The surface contamination by carbon is still significant. After consecutive sputtering processes, the W^2 , W^3 and W^4 components appear. The intensity of any one of these components after 2k eV 30 min sputtering is higher than those obtained after 200 eV 10 min (Table 4.6) implying the presence of some tungsten atoms at the W^{VI} , W^{II} and metallic states (Fig. 4.10(b) to (c)). The C 1s spectrum disappear, and the O/W ratio drop accordingly to 1.4 (Table 4.6).

	W^{I} (at. %)	W^2 (at. %)	W^3 (at. %)	W^4 (at. %)	O^{I} (at. %)	O^2 (at. %)	C (at. %)	O/W (at. %)
As deposited	17.3	0.9	---	---	52.0	5.4	24.3	3.2
200 eV, for 10 min (10th min)	13.6	7.0	8.0	8.3	56.9	5.2	1.0	1.7
2 k eV, for 30 min (40th min)	11.8	8.5	9.8	11.4	54.5	4.0	---	1.4

Table 4.6 Atomic concentration of tungsten atoms associated with the W^{I} , W^2 , W^3 and W^4 components, and the oxygen atoms associated with the O^{I} and O^2 components for the magnetron-sputtered tungsten oxide films deposited at $R_f = 2$ and $T_s = 500\text{ }^{\circ}\text{C}$.

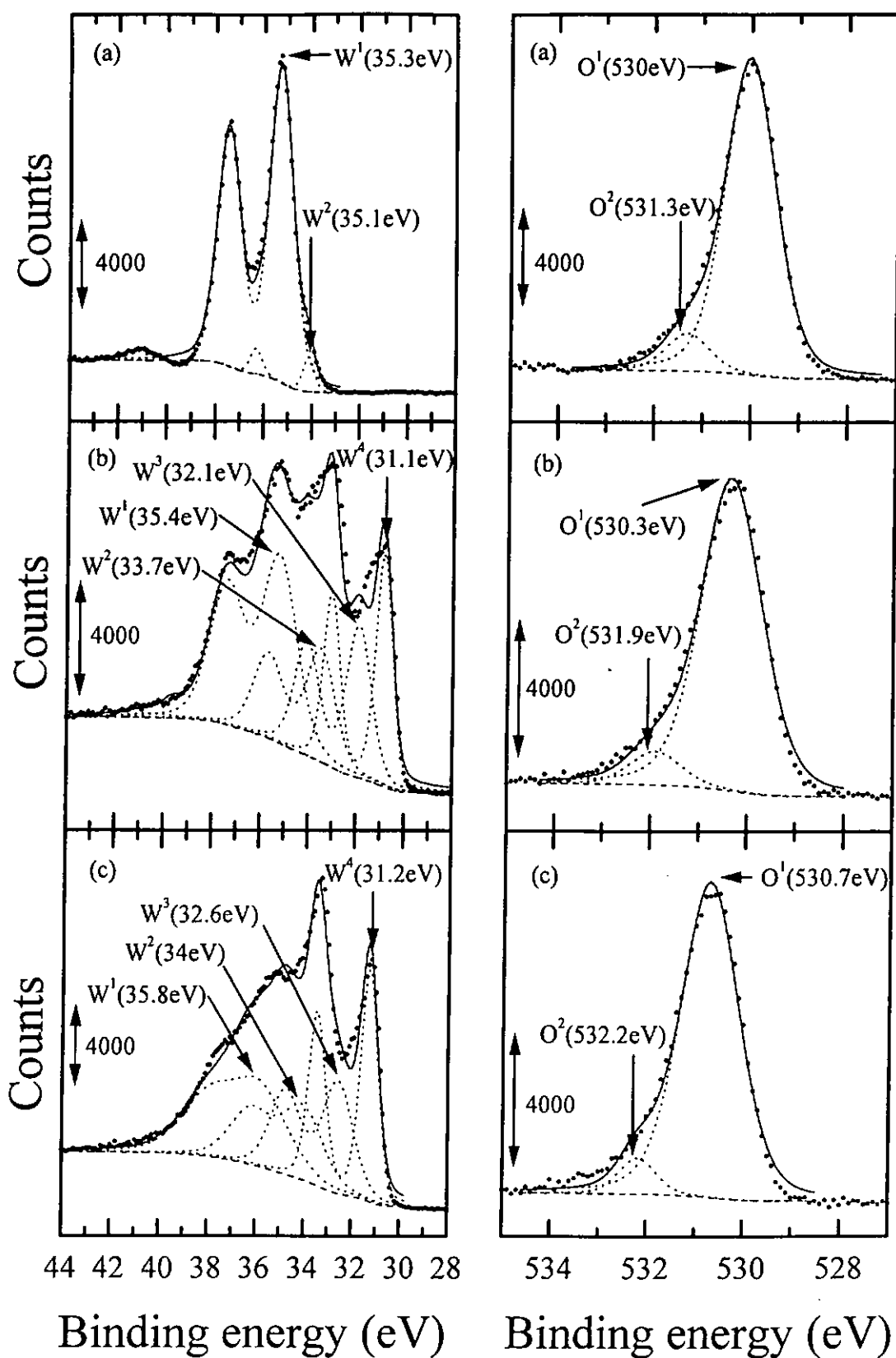


Fig. 4.10 The W 4f and O 1s photoelectron spectra of magnetron-sputtered tungsten oxide film deposited at $T_s = 500^\circ\text{C}$ and at $R_f = 2$.
 (a) Before surface cleaning,
 (b) After surface cleaning by 200 eV Ar^+ ions for 10 minutes,
 (c) After surface cleaning by 2k eV Ar^+ ions for 30 minutes.

4.5.3 Effects of Ion Bombardment on Thermally Evaporated Film on Unheated Substrate

Fig. 4.11 (a) shows the W 4f and O 1s spectra recorded from the as-deposited surface (before ion sputtering) of a thermally evaporated tungsten oxide film prepared on unheated substrate at oxygen partial pressure = 6 mTorr. XRD results illustrate that the film is amorphous. Similar to the magnetron-sputtered samples, the W 4f spectrum of this film mainly consists of a single component associated with the W^{VI} tungsten atoms. The O 1s spectrum is still dominant, whereas the O/W ratio is 3.3. The surface contamination by carbon is remarkable. Sputtering processes render the W², W³ and W⁴ components to emerge (Fig. 4.11 (b) - (c)), and at the same time suppress the O² components and the C 1s spectrum. The O/W ratio decreases and is finally stabilized at 1.3 (Table 4.7).

	W ¹ (at. %)	W ² (at. %)	W ³ (at. %)	W ⁴ (at. %)	O ¹ (at. %)	O ² (at. %)	C (at. %)	O/W (at. %)
As deposited	16.6	1.2	---	---	49.4	8.6	24.2	3.3
200 eV, 5 min (5th min)	17.1	1.8	---	---	50.4	9.4	21.2	3.2
2 k eV, 36 min (41th min)	15.0	10.8	9.0	8.3	51.7	5.2	---	1.3

Table 4.7 Atomic concentration of tungsten atoms associated with the W¹, W², W³ and W⁴ components, and the oxygen atoms associated with the O¹ and O² components for the thermally evaporated tungsten oxide films deposited on unheated substrate at oxygen partial pressure = 6 mTorr.

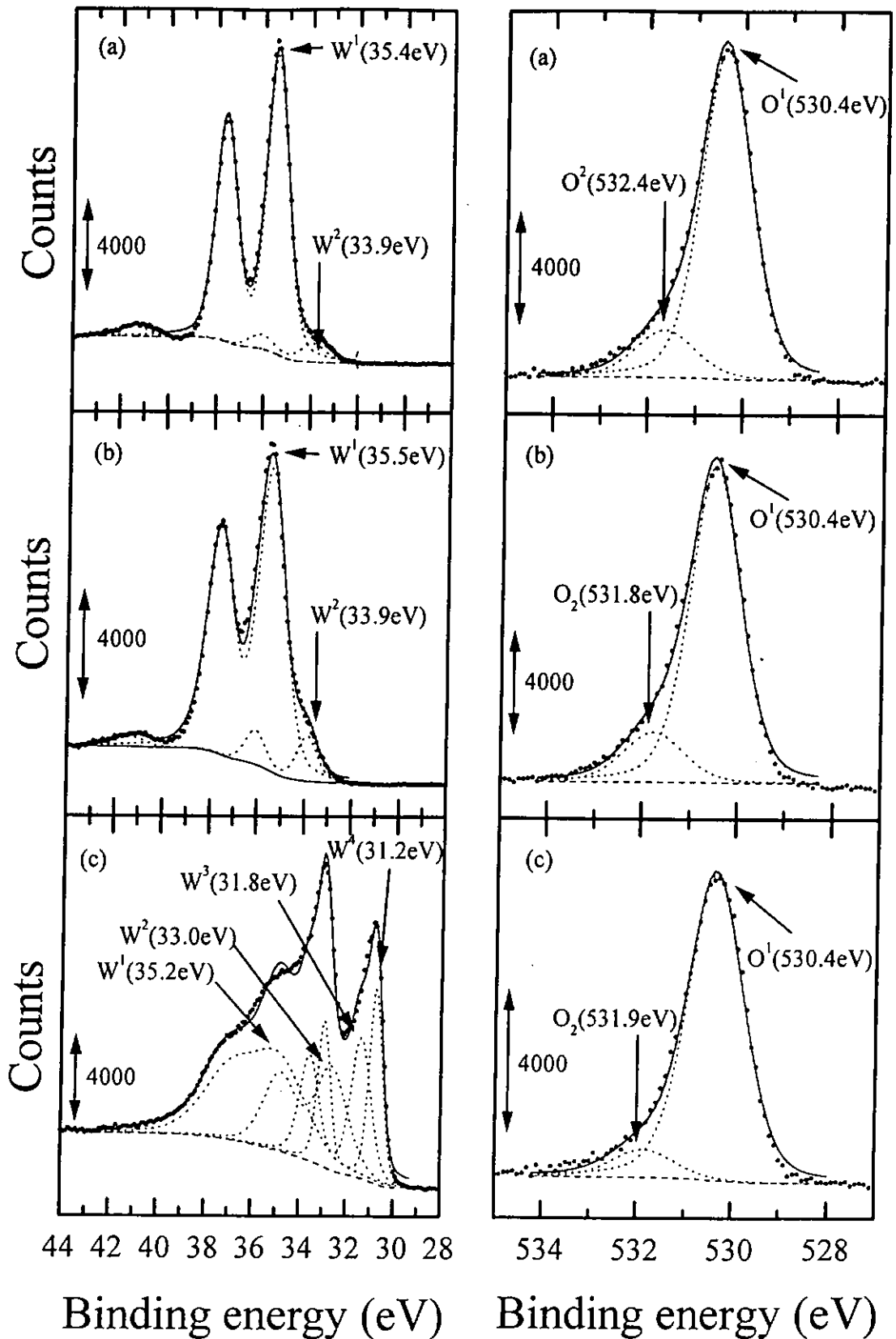


Fig. 4.11 The W 4f and O 1s photoelectron spectra of thermally evaporated tungsten oxide film deposited on unheated substrate at oxygen partial pressure = 6 mTorr.

(a) Before surface cleaning,

(b) After surface cleaning by 200 eV Ar^+ ions for 5 minutes,

(c) After surface cleaning by 2k eV Ar^+ ions for 36 minutes.

4.5.4 Profiles of W, O and O/W Ratio with Increasing Sputtering Time

Fig. 4.12 summarizes the measured O and W concentrations as functions of sputtering time. The data associated with zero sputtering time are those obtained before ion irradiation. The next sets of data were obtained after 5 min sputtering by 200 eV Ar^+ ions. Other sets of data were collected after additional sputtering processes with 2 keV Ar^+ ion, each lasting for 10 min. One can see that the trends of O and W are opposite, where the former drops and the latter rises when the accumulated sputtering time increases. In particular, after sputtering for longer than 20 min, the apparent compositions of O and W recorded are stabilized and no further change is observed. The behavior is identical for all tungsten oxide films fabricated in this study, including those deposited by magnetron-sputtering and thermal evaporation at various oxygen partial pressures, with or without substrate heating. It is no matter whether the film is amorphous or crystalline, the onsets of accumulated sputtering time beyond which O/W ratio starts to be stabilized are almost identical, namely about 20 - 30 min. The feature can also be presented by the O/W ratio as shown in the inset, where the O/W ratio decreases from a value around 3, and then drops to a value just above 1 with increasing sputtering time, and then become unchanged for longer sputtering period. It is therefore reasonably to claim soundly that the drop in the O/W ratio is mainly due to the preferential sputtering of oxygen. Preferential sputtering of oxygen has already occurred even by the first step of ion sputtering process, where the ion energy is set to be rather low (200 eV) and the sputtering time is set to be short. Furthermore, one may reason that after sufficient long sputtering period, the surface of the film is at such a state that the loss rate of W and O atoms are practically the same and kept equilibrium. This explains why the

final O/W value of all the samples after experiencing sufficiently long sputtering time are finally stabilized at rather similar levels [Feldman and Mayer 1986].

We compare the level of preferential sputtering of oxygen between the films prepared by different methods. The stabilized O/W ratio of magnetron-sputtered film obtained after prolonged sputtering is around 1.5, whether the substrate is heated or not during deposition. After experiencing 10000 times c/b cycles, the corresponding stabilized O/W ratio is as high as 2, indicating that more oxygen is incorporated into the WO_3 atomic network. On the other hand, the oxygen in the thermally evaporated sample is most readily sputtered, where the stabilized O/W ratio is as low as 1.3.

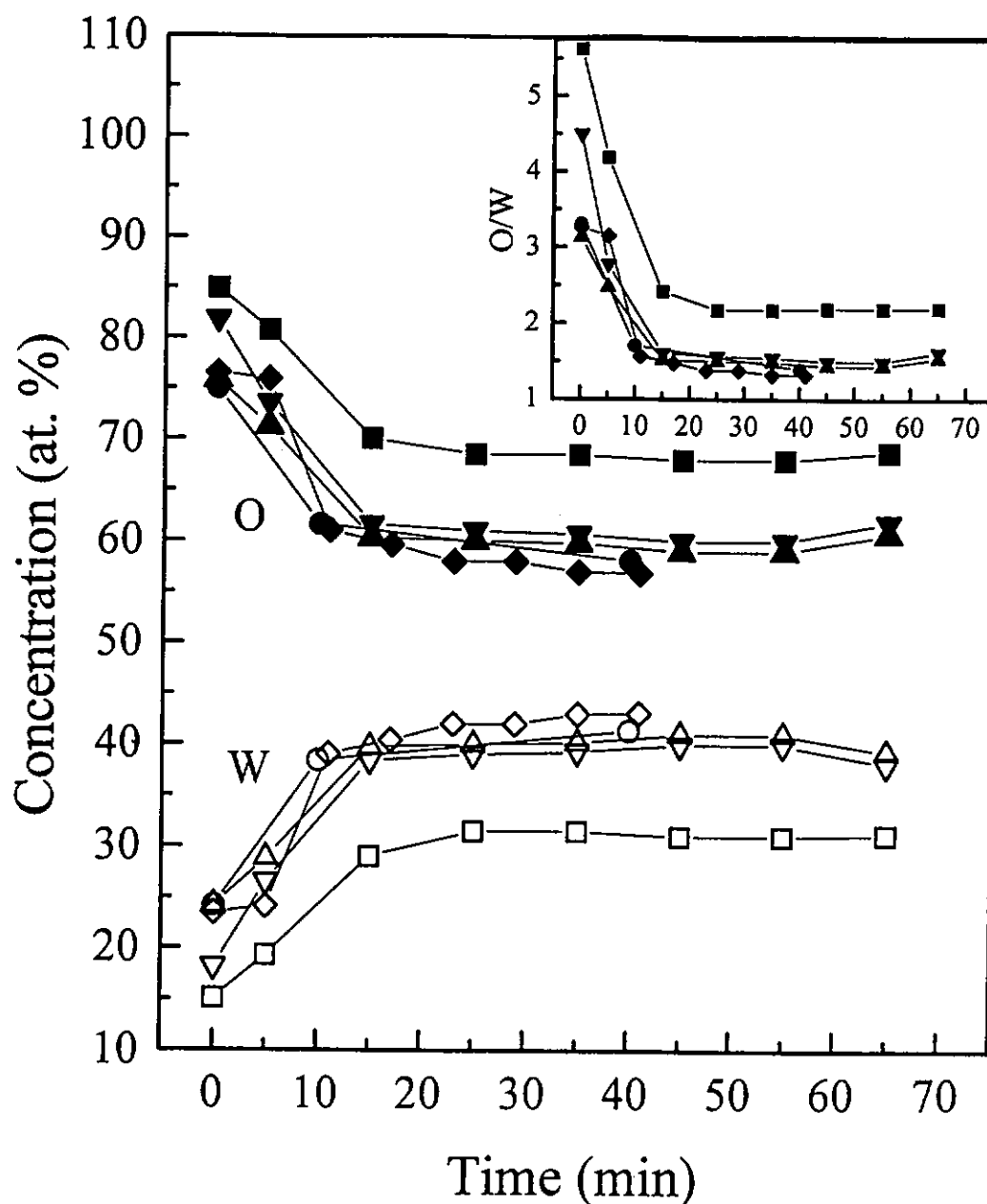


Fig. 4.12 The atomic concentration of O and W concentration as functions of sputtering time. Inset: O to W ratio.

- ▲ Magnetron-sputtered tungsten oxide films deposited on unheated substrate at $R_f=2$, as deposited.
- ▼ Magnetron-sputtered tungsten oxide films deposited on unheated substrate at $R_f=2$, after experienced 1000 c/b cycles.
- Magnetron-sputtered tungsten oxide films deposited on unheated substrate at $R_f=2$, after experienced 10000 c/b cycles.
- Magnetron-sputtered tungsten oxide films deposited at $R_f=2$ and $T_s=500^\circ\text{C}$.
- ◆ Thermally evaporated tungsten oxide films deposited on unheated substrate at oxygen partial pressure = 6 mTorr.

4.5.5 Angle-resolved XPS Analysis

Angle-resolved XPS analysis was also performed to further verify the preferential sputtering of oxygen from tungsten oxide films by under ion irradiation. In this experiment, a magnetron-sputtered tungsten oxide film (MSC2), after experiencing 10,000 times coloring/bleaching cycles, was first sputtered by 200 eV for 5 min and then by 2 keV for 60 min. For this sputtered surface, the electron detector was placed at two different positions, at each the W 4f and O 1s photoelectron spectra were collected respectively. The first position is right above the film surface, and the other is to make an angle of 45° with the film normal. For the first configuration, photoelectrons generated at a deeper level can still be able to enter the detector, so that this setting was used to probe the composition deeper beneath the film surface. For the second configuration, photoelectrons generated more near the film surface were collected, giving compositional information of a very thin layer at the film surface. Results of two repetitive measurements are summarized in Table 4.8, which shows that the oxygen-to-tungsten ratio detected by the right angle setting (probing deeper layer) is higher than that detected by the 45°-setting (probing more surface layer), indicating that the surface layer experienced more significant ion bombardment contains less oxygen, further supporting the conjecture that ion bombardment induce preferentially sputtering of oxygen from tungsten oxide films.

Detector position	O/W (1st measurement)	O/W (2nd measurement)
Normal	2.17	2.4
45°	2.05	2.2
% change	-5.5%	-8.3%

Table 4.8 O/W ratio of tungsten oxide film obtained by angle-resolved XPS analysis.

Chapter 5

Structural Analysis

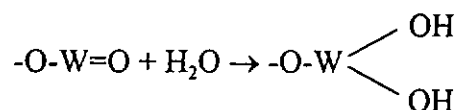
In this chapter, the results of IR absorption and XRD experiments of tungsten oxide films deposited at various deposition conditions are described and discussed.

5.1 Infrared Absorption Spectroscopy

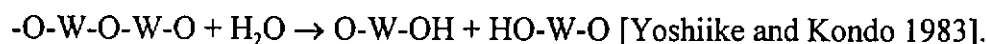
5.1.1 Effects of Oxygen-to-Argon Flow Ratio on the Structure of Magnetron-Sputtered Films

In Section 4.1 we mention that the oxygen-to-tungsten ratio (O/W) in the magnetron-sputtered films decreases from 3.1 to 2.6 when the R_f in the reactant gas admixture decreases from 2 to 1.36. Fig. 5.1 shows the corresponding change in the IR absorption spectra of the as-deposited samples (before experiencing colorating/bleaching cycles). For all the films, four absorption bands are observed (*I* - *IV*). Band *I* is the strongest, and is broad to cover a range of 500 - 1100 cm^{-1} . This indicates that the film structure is highly disordered. Band *I* has a dip at 650 cm^{-1} , and so is attributable to the vibrational modes of W-O bonds. Table 5.1 and 5.2 summaries the IR peaks of amorphous WO_3 . These peaks are commonly located in the range of 600 – 650 cm^{-1} consistent with that of the band *I*. [Azens *et al.* 1995, Salje 1975, Shigesato 1988, Yoshiike and Kondo 1983].

Band *II* and *III* are at 1400 and 1600 cm^{-1} . Band *II* is not observed by other group (Table 5.2), but is possibly originated from some oxygen-related bonds such as the O-H bending mode given an IR peak at 1400 - 1440 cm^{-1} . Band *III* may be related to the H-O-H stretching mode. The oxygen atoms may come from the some surface sorbed water molecules on the film surface [Shigesato *et al.* 1991]. Band *IV* is broad, and ranges from ~2700 to 3600 cm^{-1} . The band is originated from the O-H stretching vibration, which contains three absorption peaks at ~3000, ~3200 and ~3400 cm^{-1} . The appearance of those lines is the evidence of the presence of intermolecular bonding [Socrates 1980] such as hydroxylation according to



or hydrolysis according to



Band *II* to *IV* are believed to come from the incorporation of water molecules into the film structure during deposition.

We note in particular that, for sample MS13 $R_f = 1.36$ where the tungsten content high, and the film is optically opaque. However, band *I* still appears with rather strong intensity, indicating that the film, though oxygen deficient, still contains a rather large fraction of a WO_3 - like structure.

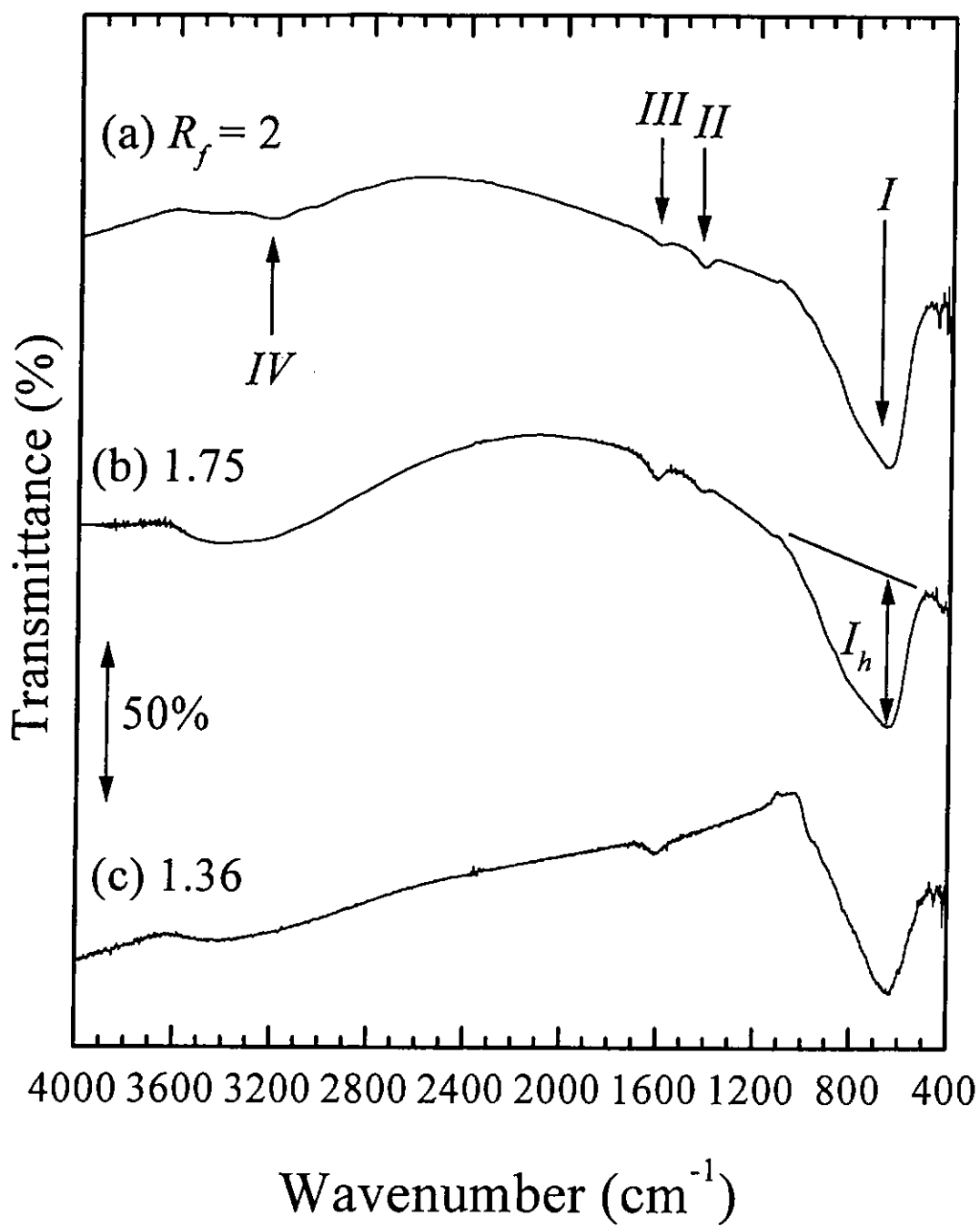


Fig. 5.1 FTIR spectra of the tungsten oxide films deposited by magnetron sputtering at various R_f .

Magnetron-sputtered samples						Thermal evaporated samples				
T_s (°C)	rm. temp.			110	300	500	O ₂ partial pressure			
R_f	1.36	1.75	2	2			Bkg.	0.4	4	6
Band I (width) (cm ⁻¹)	650 (500-1100)			650 (500-1100)	650 (500-900)	700, 800 (500-900)	600 (500-1100)		600, 800, 900 (500-1100)	
Band II (cm ⁻¹)	---	1400	1400	---			1400			
Band III (cm ⁻¹)	1600			---			1600			
Band IV (cm ⁻¹)	2700-3600	2700-3600	2800, 3050, 3200, 3600	---			2800, 3050, 3200, 3600			

Table 5.1 Summary of the IR peak positions of tungsten oxide films deposited by magnetron sputtering and thermal evaporation.

Reported data in the literature				
	Crystalline		Amorphous	
	c-WO ₃ (Raman)	c-WO ₃ (IR)	a-WO ₃ (Raman)	a-WO ₃ (IR)
Band I (width) (cm ⁻¹)	719, 807 ² (W-O)	700, 800 ¹ ; 765, 825 ² (W-O)	700, 807 ³ (W-O), 960 ³ (W=O)	600 ¹ (500-1100); 665 ² , 920 ² (W=O); 650 ⁴ (500-1100)
Band II (cm ⁻¹)	---	---	---	---
Band III (cm ⁻¹)	---	---	---	1600 ⁴ H-O-H
Band IV (cm ⁻¹)	---	---	---	3400 ⁴ O-H

Table 5.2 Summary of the peak positions observed in the IR and Raman spectra of tungsten oxide film [1. Azens *et al.* 1995, 2. Salje 1975, 3. Shigesato 1988, 4. Yoshiike and Kondo 1983]. Some corresponding assignments are labeled.

5.1.2 Effects of Substrate Temperature on the Structure of Magnetron-Sputtered Films

When the substrate temperature (T_s) is increased to 110°C, band *II* to *IV* disappear. This is because at elevated temperature, the film material is packed closer and have less defects. Therefore, it is less probably for the water vapour molecules to be absorbed and react with the materials. Since band *II* to *IV* are related to bond associated with oxygen from physisorbed water molecules [Yoshiike and Kondo 1983], their intensity would become small as T_s is risen. In addition, with increasing T_s , the absorption at around 850 to 1100 cm^{-1} become weaker. This is because band *I* of the samples deposited at lower T_s may include some W=O bonds, which absorbs IR at a wavenumber of 950 cm^{-1} (Table 5.1). As T_s increases, the film structure tends to approach that of crystalline WO_3 , such that the concentration of W=O bonds decreases. This result in a weaker IR absorption at the range between 850 and 1100 cm^{-1} . As a consequence, band *I* seems to become slimmer. Furthermore, band *I* of the film deposited at 500 °C appears to contain two dips, roughly having a dip position at 700 and 800 cm^{-1} respectively. The peak positions of these peaks correspond to those of crystalline WO_3 . These dip positions are consistent with those of the IR absorption from crystalline WO_3 sample (Table 5.2). This is because the film deposited at 500 °C has been crystallized, as will be further discussed in Section 5.2.

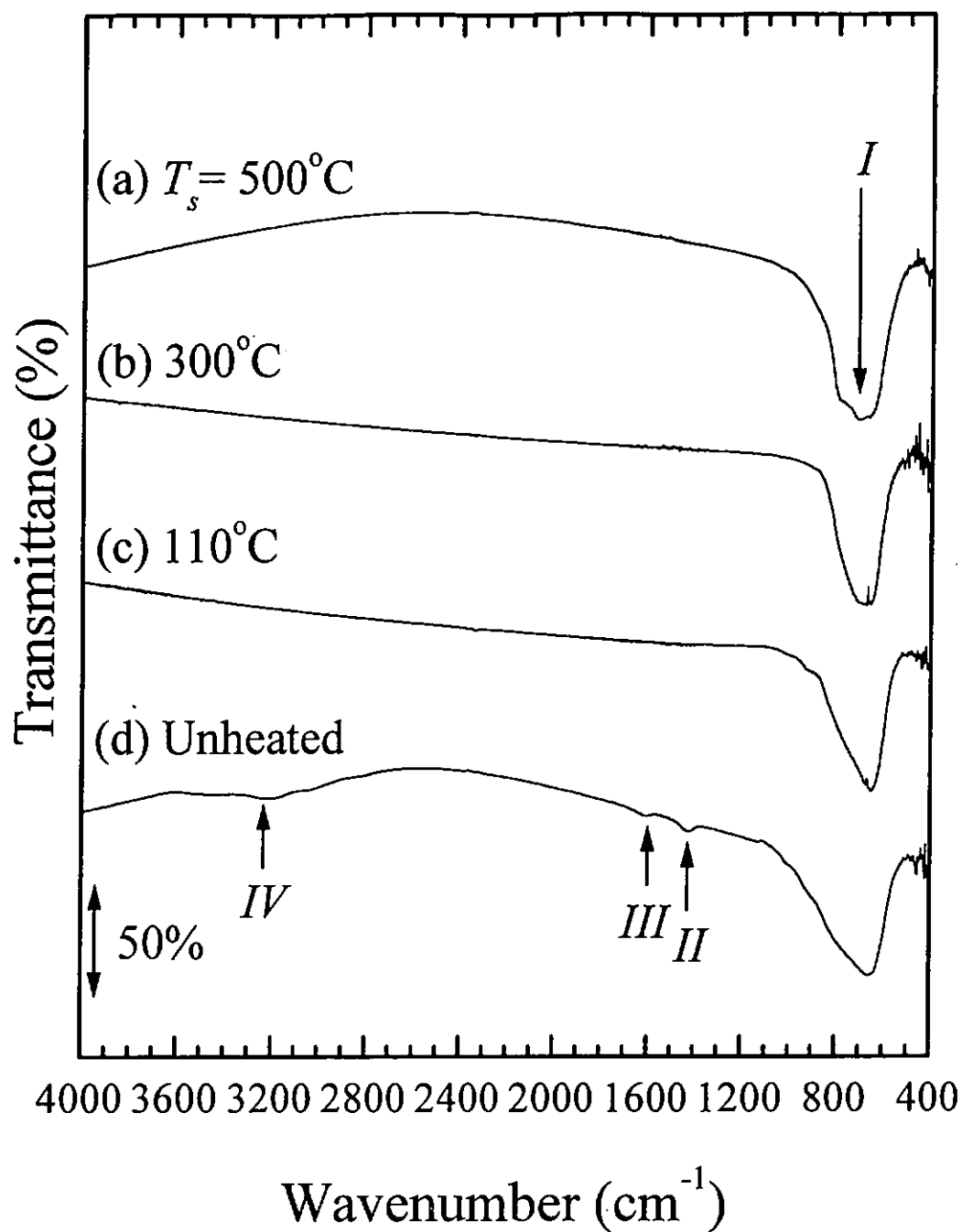


Fig. 5.2 FTIR spectra of the tungsten oxide films deposited by magnetron sputtering at various T_s .

5.1.3 Effect of Oxygen Partial Pressure on the Structure of Thermally Evaporated Films

The IR absorption spectra of the W oxide films deposited by reactive thermal evaporation at different oxygen partial pressures are shown in Fig. 5.3. Band I of the film deposited at the background pressure of 2×10^{-6} Torr has a sharp peak at 600 cm^{-1} . Some another absorption band superimpose on this sharp dip, generating a broad absorption band from $500 - 1100 \text{ cm}^{-1}$. The sharp dip at 600 cm^{-1} may be due to the fact that thermal evaporation of WO_3 powder at low ambient pressure may involve the evaporation of atomic clusters. These clusters retain some short of atomic ordering as in some tungsten oxide phases, such that they condense at the substrate to generate such a characteristic IR absorption signal. However, when the oxygen ambient pressure starts to increase, the mean free path of the species in the vacuum chamber is shortened. Interactions between the oxygen molecules and the evaporated species becomes very frequent. This may result in an atomic network with high randomness. So that band I becomes broader. Furthermore, a small peak is merely observable at 950 cm^{-1} , which coincides with the position of the IR peak associated with the W=O bonds, as marked in Fig. 5.3. The appearance of this peak shows that the clusters arriving the substrate are randomly packed. The surface of and the boundary regions between these clusters, are full of defects, such that W=O bonds are formed to give this peak. Shigesato et al. Suggested that the W=O stretching bonds at 960 cm^{-1} are mainly located at the surface of the clusters [Shigesato *et al.* 1991].

Furthermore, the peaks associated with oxygen (band *II* to *IV*) are noticeably strong. It is because as observed by atomic force microscopy imaging, the films deposited at higher oxygen pressure are very rough, such that more water molecules are trapped and react with the film material [Yoshiike and Kondo 1983]. This leads to the appearance of the high intensity of the oxygen related bands as shown.

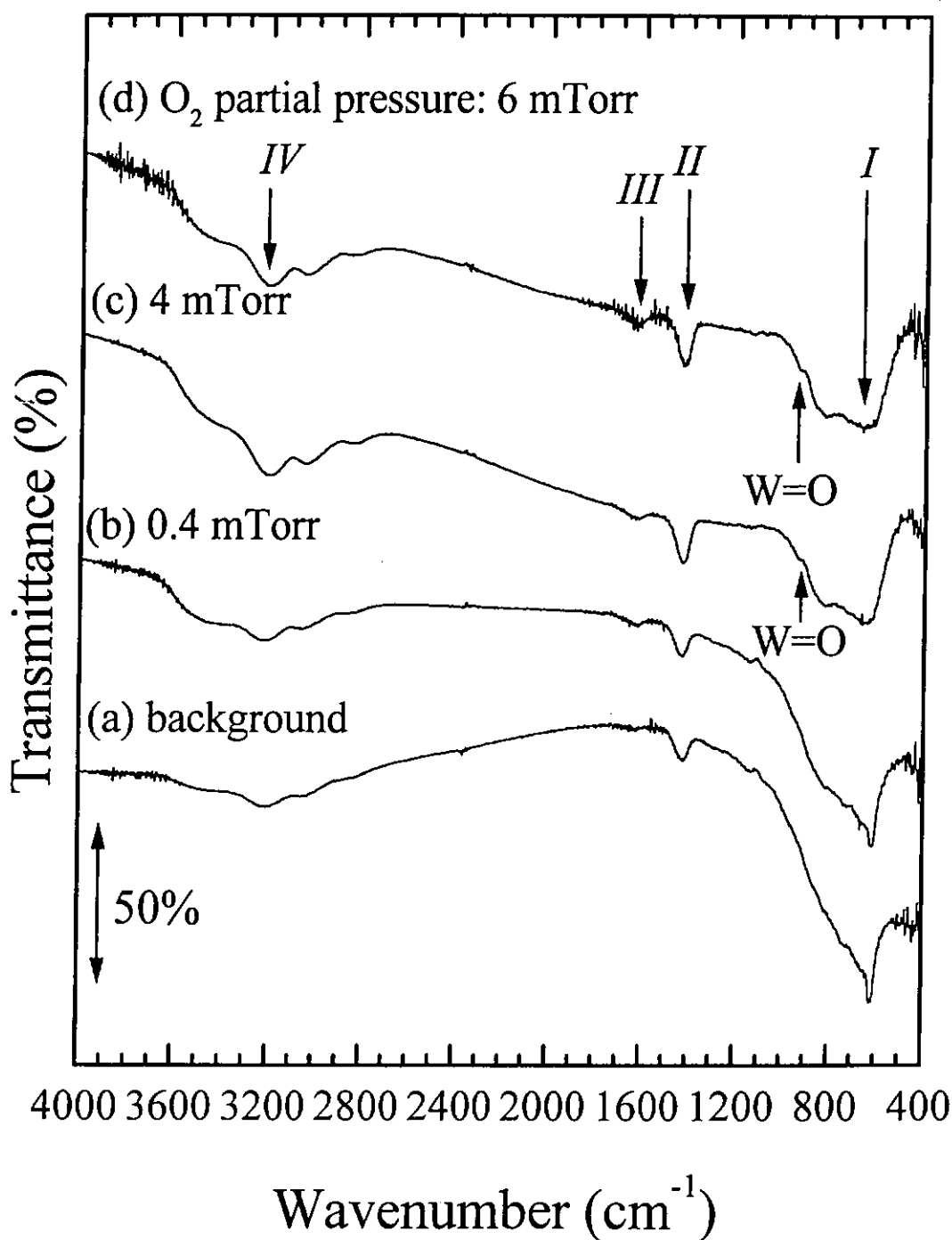


Fig. 5.3 FTIR spectra of the tungsten oxide films deposited by reactive thermal evaporation at different oxygen partial pressures.

5.2 X-ray Diffraction

The XRD spectra of the tungsten oxide films made by reactive magnetron sputtering on ITO coated glass in various reactant gas flow ratios (R_p) were collected and shown in Fig. 5.4. The spectra show that the films are amorphous, independent of the oxygen-to-argon gas flow ratio admitted into the chamber during deposition.

For $T_d \geq 300$ °C, the films start to be crystallized. Characteristic peaks are recorded at $2\theta = 24^\circ, 26.5^\circ, 29^\circ, 34^\circ, 41.5^\circ, 50^\circ$ and 55° (Fig. 5.5). These peaks can be identified with the Miller indices by referring to the corresponding spectrum of polycrystalline WO_3 [Zhong *et al.* 1992 and Kaneko *et al.* 1980]. Different from the sample deposited at 500 °C, the spectrum of the sample that deposited at 300 °C only contains two peaks, which are relatively weak compared with that of the sample deposited at 500 °C. These small peaks associate with small grain size. We note that the temperature range for the crystallization of tungsten oxide films is basically consistent with that report by Matsuihiro *et al.* They showed that sign of crystallization of amorphous tungsten oxide is observable by annealing at temperatures higher than 370 °C [Matsuihiro and Masuda 1980].

Fig. 5.6 shows the spectra of films made by reactive thermal evaporation at various O_2 partial pressures on unheated substrate. A broad peak in the range of $2\theta \sim 20^\circ - 28^\circ$ is observed. This indicates that these samples are amorphous. No observable change is produced to the XRD spectra by increasing the oxygen partial pressure from 0.4 to 10 mTorr, although significant change in the IR absorption spectra are found and analyzed in Section 5.1.

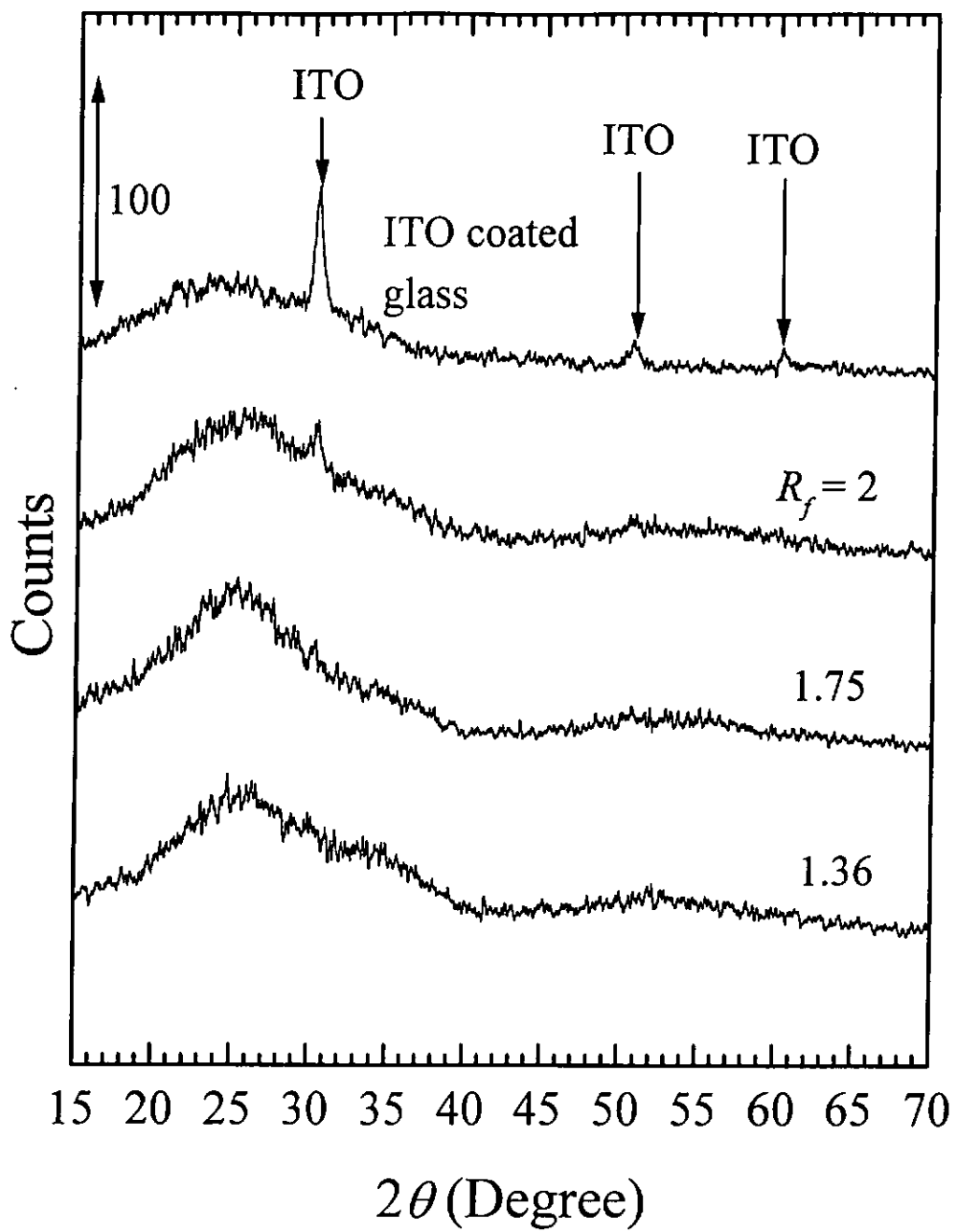


Fig. 5.4 XRD spectra of magnetron-sputtered tungsten oxide films deposited in various R_f .

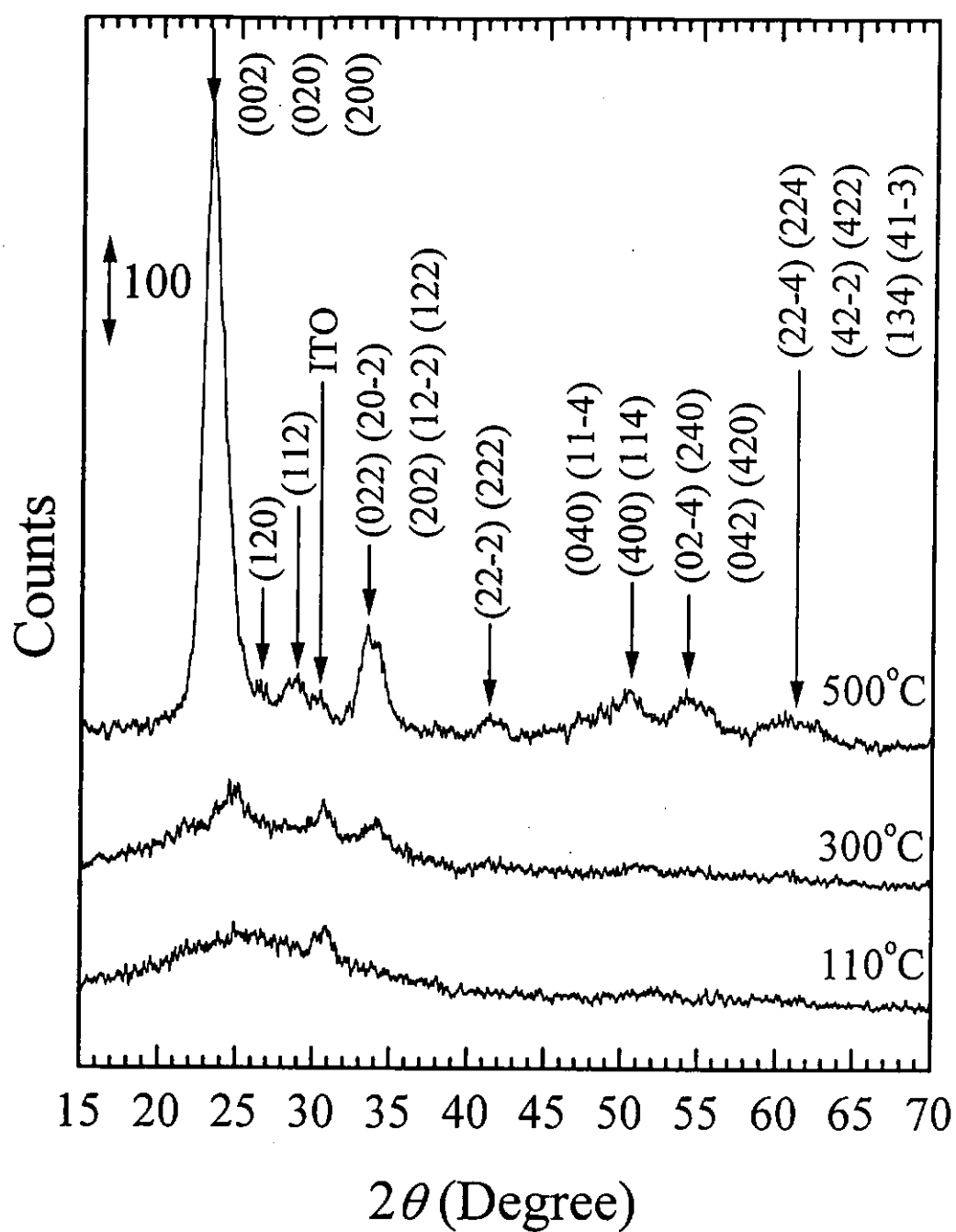


Fig. 5.5 XRD spectra of magnetron-sputtered tungsten oxide films deposited at fixed $R_f=2$, and various substrate temperatures.

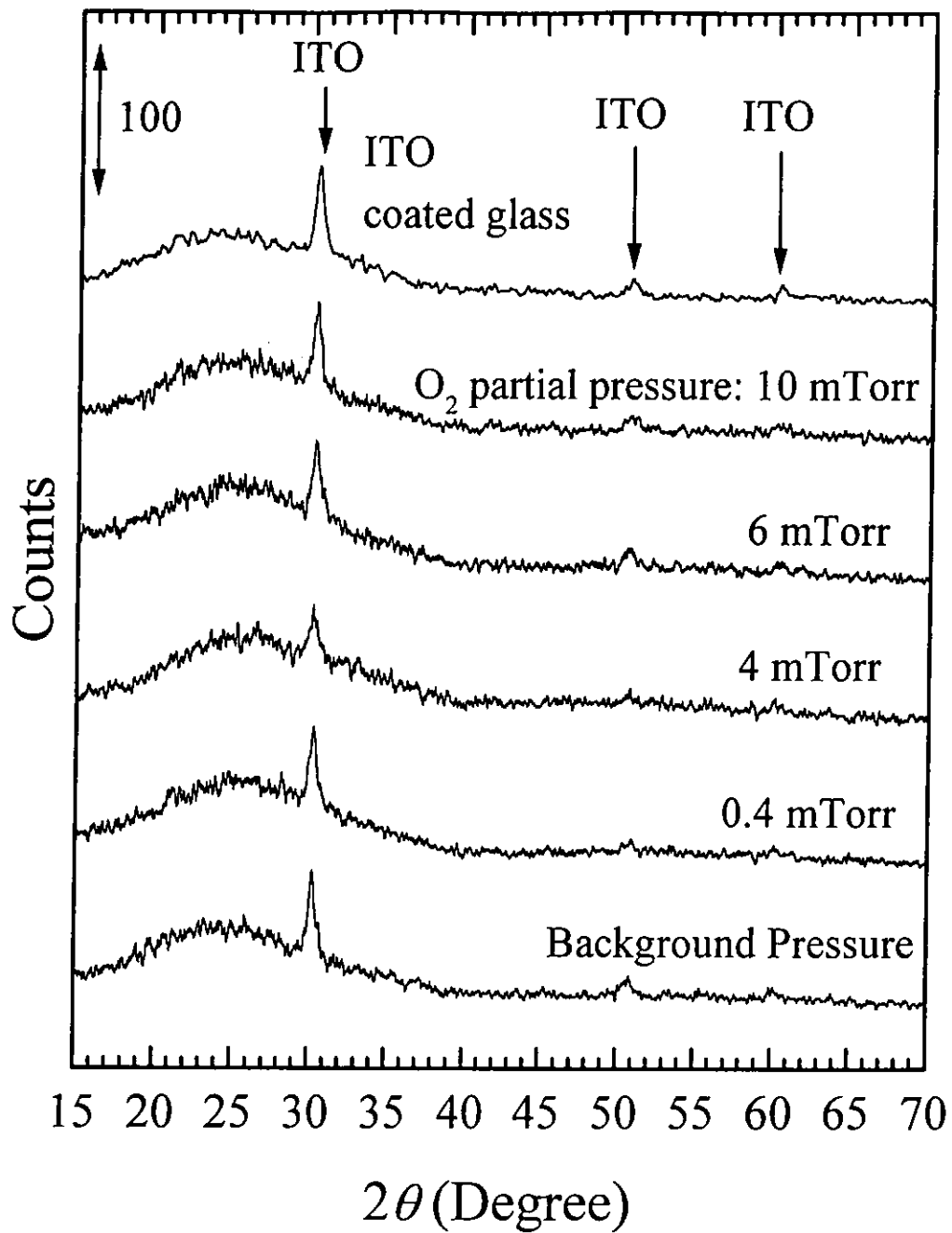


Fig. 5.6 XPS spectra of thermally evaporated tungsten oxide films deposited on unheated substrates at various oxygen partial pressures.

Chapter 6

Electrochromic and Mechanical Properties

In Section 6.1, the electrochromic properties of the tungsten (W) oxide films deposited by magnetron sputtering and thermal evaporation are presented. Results of multicyclic voltammetry, optical absorption at the wavelength of He-Ne laser and coloration efficiency are discussed. The stability of the performance of electrochromism of the films is investigated. In Section 6.2, results of the mechanical properties of the films examined by nanoindentation experiments are presented.

6.1 Electrochromic Properties

A magnetron-sputtered and a thermally evaporated tungsten oxide films were selected for multicyclic voltammetry experiments. Total number of color-bleach cycles was set to be 10000 cycles (Table 6.1). The scan rate of the voltage applied between the working (ITO) and reference (SCE) electrodes is fixed at 400 mV s^{-1} . Fig. 6.1(a) and (b) show the cyclic voltammograms (current-voltage characteristic) of those two samples during Li^+ intercalation/deintercalation in films, where the measured current is in terms of current density and the area of the working electrode is normalized to 1 cm^2 . The cathodic and anodic currents are the currents flowing out and injected into the sample during the coloring and bleaching processes, respectively. The cathodic current is assigned to be negative and anodic current is positive. Considering that the thermally evaporated films are thinner, in order to

prevent from injecting excessive charge into the sample, the range of the potential scan is set to be narrower than that used for the magnetron sputtered films, such that the maximum electric fields experienced by the two samples are approximately identical [Hashimoto *et al.* 1990].

The current-voltage response of the magnetron-sputtered sample (MS11) is more stable and durable than that of the thermally evaporated sample (TE4). This can be seen by referring to the cathodic EMF of the cyclic current-voltage loops of the two samples. The cathodic EMF is the voltage at which the current during intercalation of ions starts to rise. Comparing Fig. 6.1(a) and (b), the cathodic EMF of the magnetron-sputtered films is basically not shifted, and remains stable at 0.3 V (Fig 6.1(a)). However, the cathodic EMF of the thermally evaporated film starts at 0 V for the 1st cycle, and then gradually shifts to -0.6 V after at the 10⁴th cycle. This is possibly because that some Li⁺ ions are accumulated in the films or the film is dissolving into the electrolyte, such that the cathodic EMF of the film is moved to more cathodic voltage [Kamimori *et al.* 1987, Nagai *et al.* 1986]. The phenomenon reduces the total amount of ions that can be inserted in the successive cycles, causing the following current-voltage loops become smaller.

As an example Fig. 6.2 shows the first current-time curve of the magnetron-sputtered film as well as its corresponding optical absorption curve [Reichman *et al.* 1979]. From 0 to 8 s, Li⁺ is inserted into the film (intercalation), so that the film is changed to the Li_xWO₃ state, with x being increased. In the film, some tungsten atoms are reduced to have low valances. As a consequence, the optical absorption increases (coloring). From the 8th to 19th sec, the current flows in the opposite

direction so the Li^+ ions are extracted to leave the sample. Meanwhile, the optical absorption decreases and finally reaches a minimum value before the next cycle starts [Greef *et al.* 1985].

Sample (on ITO coated glass)	Potential range of scanning (V)	Scan rate (mV s^{-1})	R_f	O_2 partial pressure (mTorr)	Thickness (nm)
MS11	-/+ 2	400	2	N/A	330
TE4	-/+ 1.14	400	N/A	6	188

Table 6.1 Parameters used in the cyclic voltammetry experiments for the magnetron-sputtered and thermally evaporated tungsten oxide films.

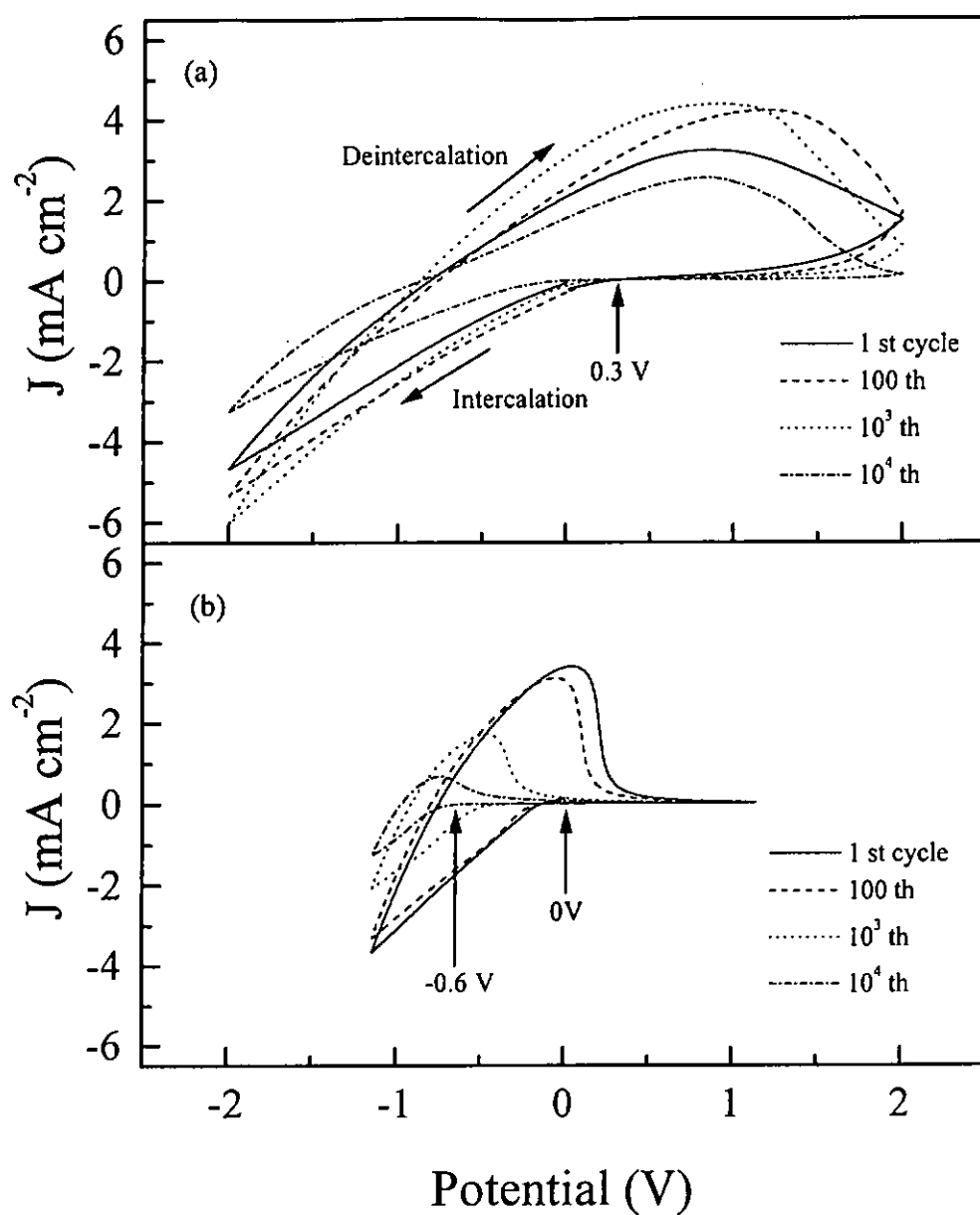


Fig. 6.1 Cyclic voltammograms of the tungsten oxide films deposited by (a) magnetron sputtering on unheated substrate at fixed $R_f = 2$, and (b) thermal evaporation on unheated substrate at O_2 partial pressure of 6 mTorr. The voltage scan rate was set at 400 mV s^{-1} . Arrows indicate the direction of scan.

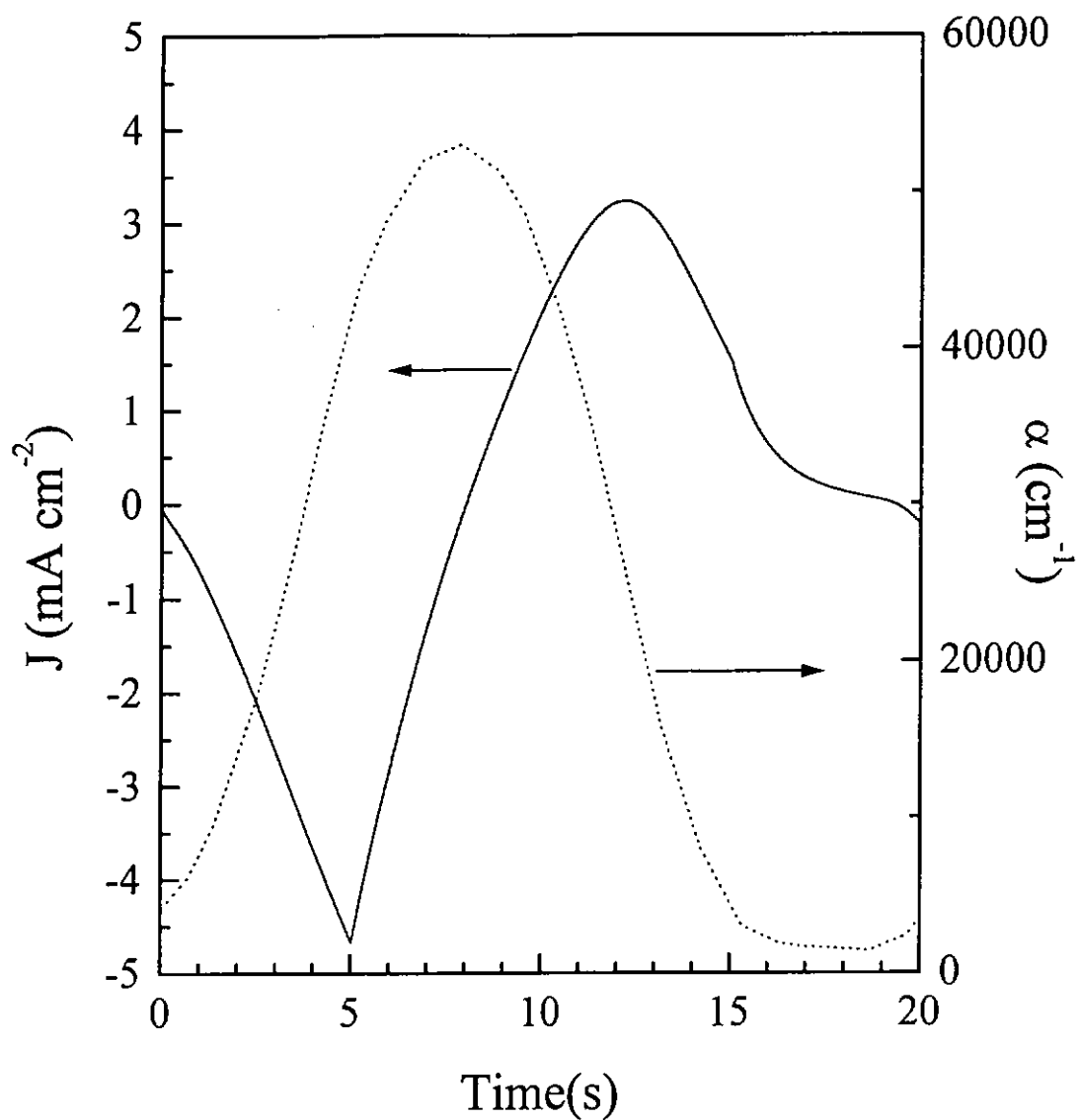


Fig. 6.2 A typical plot of optical transmittance during a coloring/bleaching cycle and the corresponding variation of current for a magnetron-sputtered sample.

Fig. 6.3 shows the change of the volume density of Li^+ ions intercalated and deintercalated charge into the magnetron-sputtered and thermally evaporated films for each cycle when coloring/bleaching experiment proceeds. The magnetron-sputtered film is more stable, such that the total charge inserted into and extracted from the film for each cycle changes only mildly up to ten thousand cycles. However, from the 100th to the 10^3 th cycle, the volume density of the intercalated ions during the coloration process of the thermally evaporated film drops prominently. This reflects that the thermally evaporated film has already degraded considerably within the first 10^3 cycles. Therefore, the lifetime of the thermally evaporated film is too short for it to have any practical use. This is possibly due to the loose film structure, which is less stable subjected to the accumulation of Li^+ ions or dissolution of the film in the liquid electrolyte.

The maximum intercalated/deintercalated charge density and maximum optical absorption of the magnetron-sputtered sample occur at the 10^3 th cycle which corresponds to the optical density (OD) of 1.05 at maximum absorption coefficient (α_{max}) $\sim 73,000$ (Fig. 6.3 and 6.4). The increase in α with charge density from the first cycle to the 10^3 th cycle reveals that the film structure has experienced some sort of structural change due to incorporation of some amount of Li^+ ions.

Fig. 6.4 shows the optical α of the film in the colored and bleached states. The trend of α can be correlated to the change in the intercalated/deintercalated charge density. The value of α of the bleached state is negligibly small, where the film is transparent. The optical modulation of the magnetron-sputtered film is at least two times larger than that of the thermally evaporated film. The thermally

evaporated film exhibits a maximum OD of 0.25 at the 100th cycle. This result reflects that the magnetron-sputtered film has better performance for light intensity modulation.

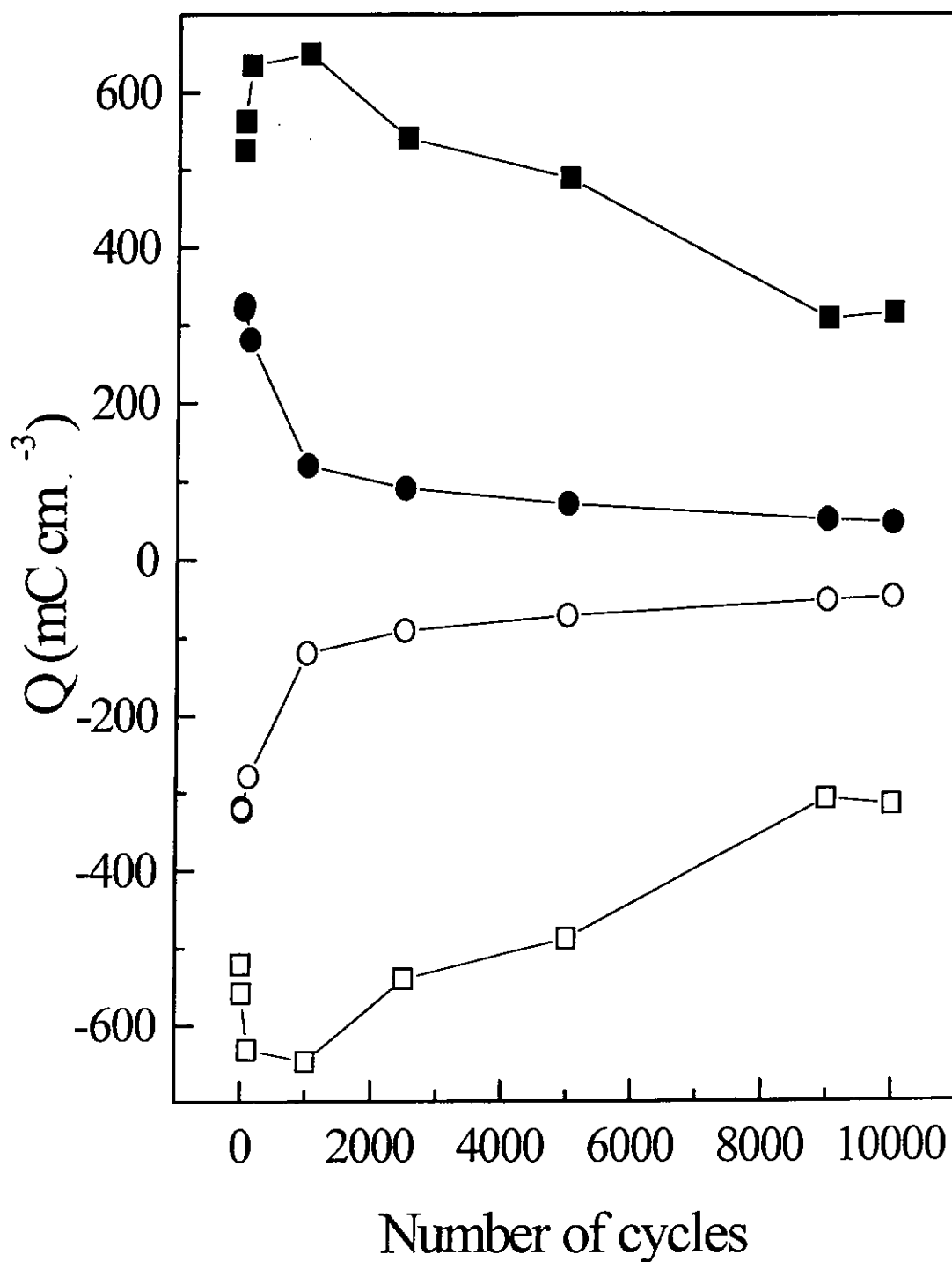


Fig. 6.3 The volume density of Li^+ ions intercalated and deintercalated charge into the magnetron-sputtered film (■ colored, □ bleached) and thermally evaporated film (● colored, ○ bleached) for each cycle when coloring/bleaching experiment proceeds.

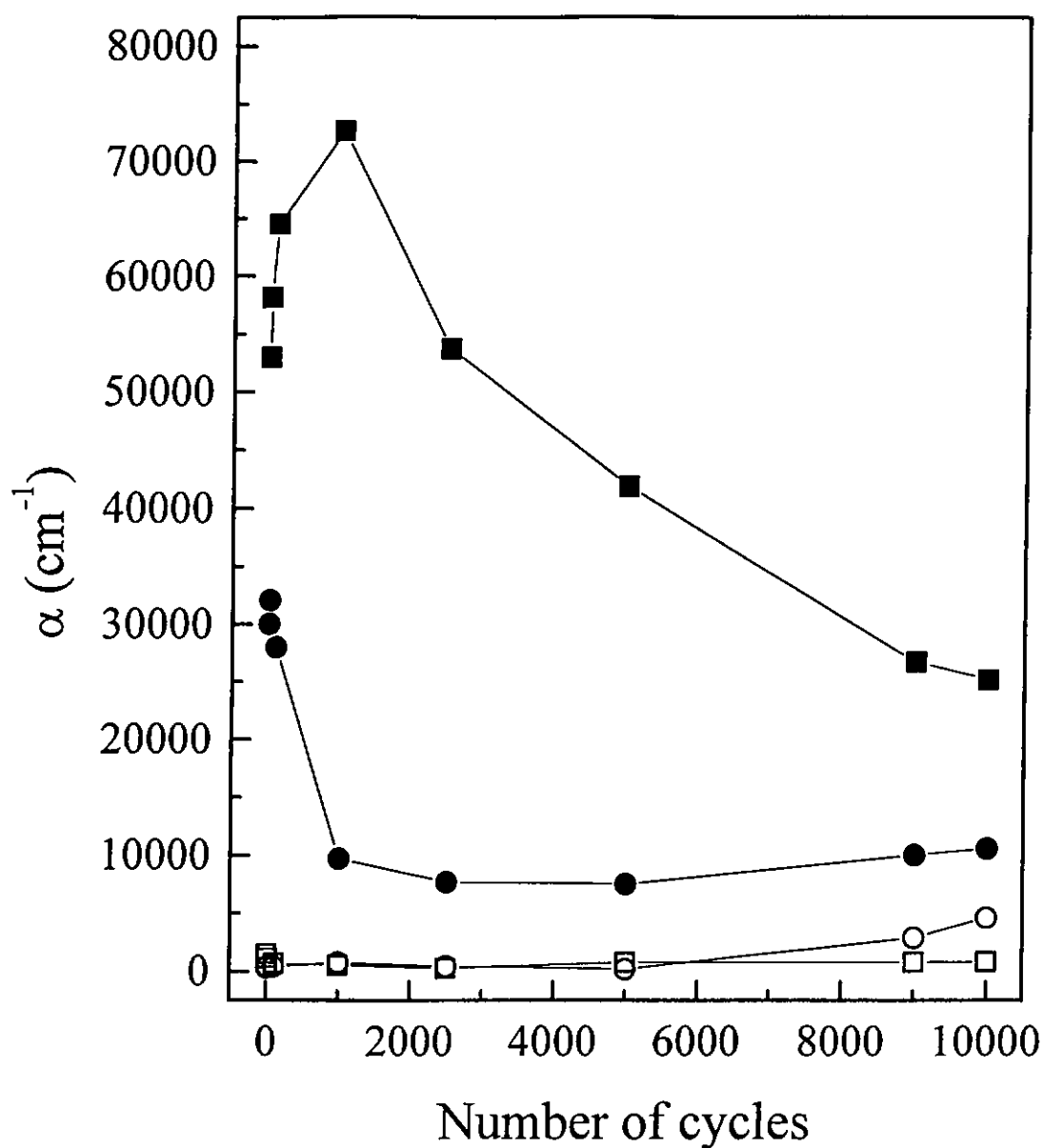


Fig. 6.4 The optical absorption coefficient of the magnetron-sputtered film (■ colored, □ bleached) and thermally evaporated film (● colored, ○ bleached).

The coloration efficiency (η) of the two samples can be evaluated by the following equation:

$$\eta = \frac{(\alpha_{\max} - \alpha_{\min})t}{Q_{in}}$$

where α_{\max} and α_{\min} are the optical absorption coefficients of the colored and bleached states, Q_{in} is the intercalated charge density, and t the thickness. The change of η with increasing number of c/b cycles is plotted in Fig. 6.5. The maximum η of the magnetron-sputtered film is $0.11 \text{ cm}^2 \text{ mC}^{-1}$, occurring at the 1000th cycle. It then drops to $0.078 \text{ cm}^2 \text{ mC}^{-1}$ after 10000 times of coloring/bleaching cycles. The film remains working very well. For the thermally evaporated film, the maximum value of η is $0.098 \text{ cm}^2 \text{ mC}^{-1}$, corresponding to the 100th cycles. The η of the thermally evaporated sample drops to a minimum at 5×10^3 cycles, accompanied by degradation of the electrochromic properties. Although η seems to rapidly rise after 1000 cycles, however, it does not mean that the optical switching ability become better on the contrary, α_{\max} becomes so large that the film could not be completely bleached and remains in blue color. As such, the apparent value of η obtained from the definition seems to become large are layer within the 2500th and 9000th (Fig. 6.5). In fact, the large absorption coefficient in the range reflects that, a great amount of ions have been incorporated irreversibly into the film and stay in the film permanently. From this point of view, the film has already significantly degraded after 1000 times of c/b cycles.

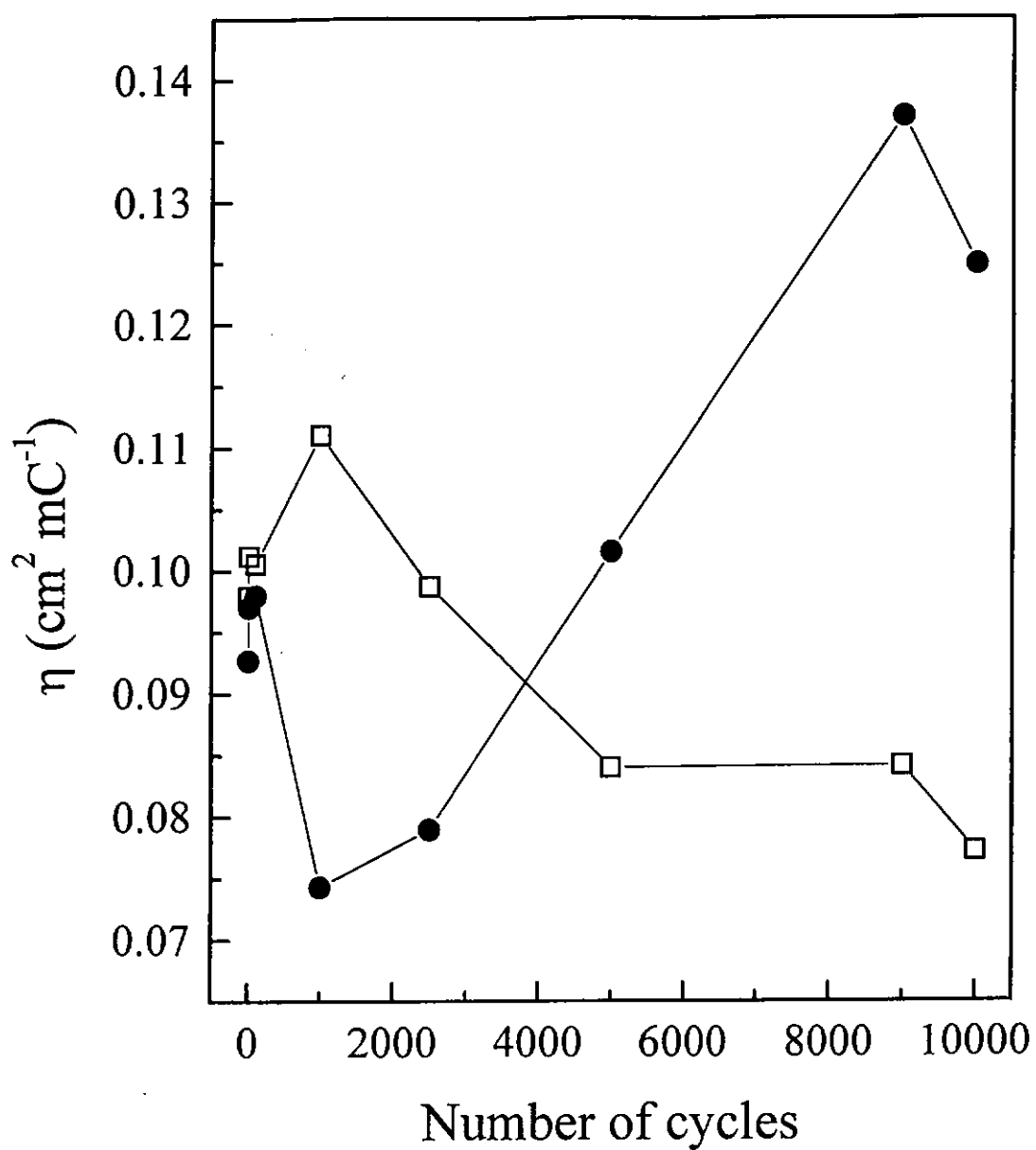


Fig. 6.5 The change of coloration efficiency of the magnetron-sputtered film (\square) and thermally evaporated film (\bullet).

6.2 Mechanical Properties

6.2.1 Mechanical Properties of Magnetron-Sputtered Tungsten Oxide Films

Considering the influence of the gas flow ratio $[O_2]/[Ar]$, denoted as R_f , on the mechanical properties of the magnetron-sputtered tungsten oxide films deposited on unheated substrates first (sample MS11 - MS13 as listed in Table 6.2). When R_f is equal to 2 (sample MS11), the O/W ratio in the film is close to 3, indicating that the film structure is very close to that of crystalline WO_3 . When R_f decrease to 1.36 (sample MS13), the O/W ratio drops to 2.6, showing that the film is oxygen deficient compared to crystalline WO_3 . The drops in oxygen content results in the rise of film density from a low value of 7.7 to 10.5 g cm⁻³ (Table 6.2). We note that the density of film MS11 is close 7.16 g cm⁻³ of crystalline WO_3 , consistent with its WO_3 -like structure observed [Gerand *et al.* 1981]. For the oxygen deficient sample MS13, the tungsten content is high such that the hardness increased by a factor of more than 2; compared to sample MS11.

Sample	R_f	T_s (°C)	Thickness (nm)	O/W ratio	Density (g cm ⁻³)	H (GPa)	E (GPa)
MS11	2	Unheated	420	3.1	7.7	2.69	79.83
MS12	1.75	Unheated	485	3.2	8.7	4.32	79.69
MS13	1.36	Unheated	638	2.6	10.5	5.98	111.86
MS21	2	110	117	3.4	7.3	5.57	95.81
MS22	2	300	152	3.3	7.5	4.91	92.22
MS23	2	500	406	3.2	7.7	5.44	86.31

Table 6.2 Hardness and elastic modulus of samples made by reactive magnetron sputtering.

If we consider the structure of the high-oxygen containing samples MS11. XRD result illustrates that the film is amorphous. Considering that its density is close to that of crystalline WO_3 , one may assume that the film is actually constructed of an amorphous WO_3 -like random network, in which the short-range order of crystalline WO_3 is retained. Porosity of the film is also supposed to be low.

Associated with such an atomic network, the indentation depth dependence of hardness and elastic modulus of samples MS11-MS13 are presented in Fig. 6.6(a) and 6.6(b). Each point in the figures is an average of the results of five identical repetitive measurements, where the representative error bar attached on the first point reflects the divergence of the data. The depth dependence of the data in the range below 1000 nm seems to be prominent. However, a closer look presented by the inset, magnifying the region below 100 nm, shows that the variation of the data points at shallow depths are actually very mild such that the average in the range of 20 - 40 nm is used to reflect the mechanical properties of the film material where the substrate effect could be negligible.

With this criterion, the data of hardness and elastic modulus are summarized in Table 6.2. The high-oxygen containing sample MS11 has the lowest hardness of 2.69 GPa, which is expected to reflect the mechanical response of WO_3 -like continuous random network under indentation. It is because the film is amorphous, there are no crystalline grains to contribute to the film hardness. The AFM image of MS11 (Fig. 6.7(a)) shows that the film is smooth (note the large magnification), where the roughness obtaining from averaging the height in an area of $2 \times 2 \mu\text{m}^2$

2.08 nm, indicating that film is rather dense with very low pores. Sample MS13 has the highest hardness of 5.98 GPa (close to 7 GPa of metal tungsten) [Clemens *et al.* 1999] because of its high tungsten content.

X-ray diffraction data of sample MS21 deposited at 110 °C illustrate that the film is still amorphous. Regarding the oxygen content in the film and the density are very close to those of crystalline state, the film is therefore proposed to have a dense WO₃-like random network, as if that proposed for sample MS11. However, the hardness of MS21 is about two times higher than that of sample MS11 (Table 6.2), leading one to infer that the hardness of MS11 is actually affected by the presence of some voids. The presence of small defects make sample MS11 to have weaker resistance against mechanical interactions such as indentation, such that a much lower hardness is resulted. As AFM image of MS21 (Fig. 6.7(b)) shows that it is slightly smoother than MS11. This results reflects that temperature of 110 °C is already sufficiently high to remove many small defects in an amorphous atomic network of tungsten oxide, leading to great increase in film hardness, though the atomic network remains to be amorphous.

Sample MS23 which deposited at 500 °C, has been crystallized. The average grain size of MS23 estimated from the full width at half maximum of the peak at $2\theta \approx 23^\circ$ is about 10 nm. It has a hardness of 5.44 GPa. The result illustrates that the grain growth does not contribute to the hardness of the films. The corresponding AFM micrograph is shown in Fig 6.7 (c). Different from sample MS11 to MS13 deposited on unheated substrates, Fig. 6.8(a) shows that the hardness of MS21 to MS23 are sensitive to indentation depth down to very shallow indents. This may

imply that the grain size is not uniform, but shows a distribution along the direction of the film normal, which is possibly due to existence of a slight temperature gradient for the substrate surface to the growing front of the film Fig. 6.8(b) shows that the elastic modulus is less dependent on depth, implying the uniformity mentioned above affects very little on elastic deformation, but mainly on plastic deformation induced during indentation.

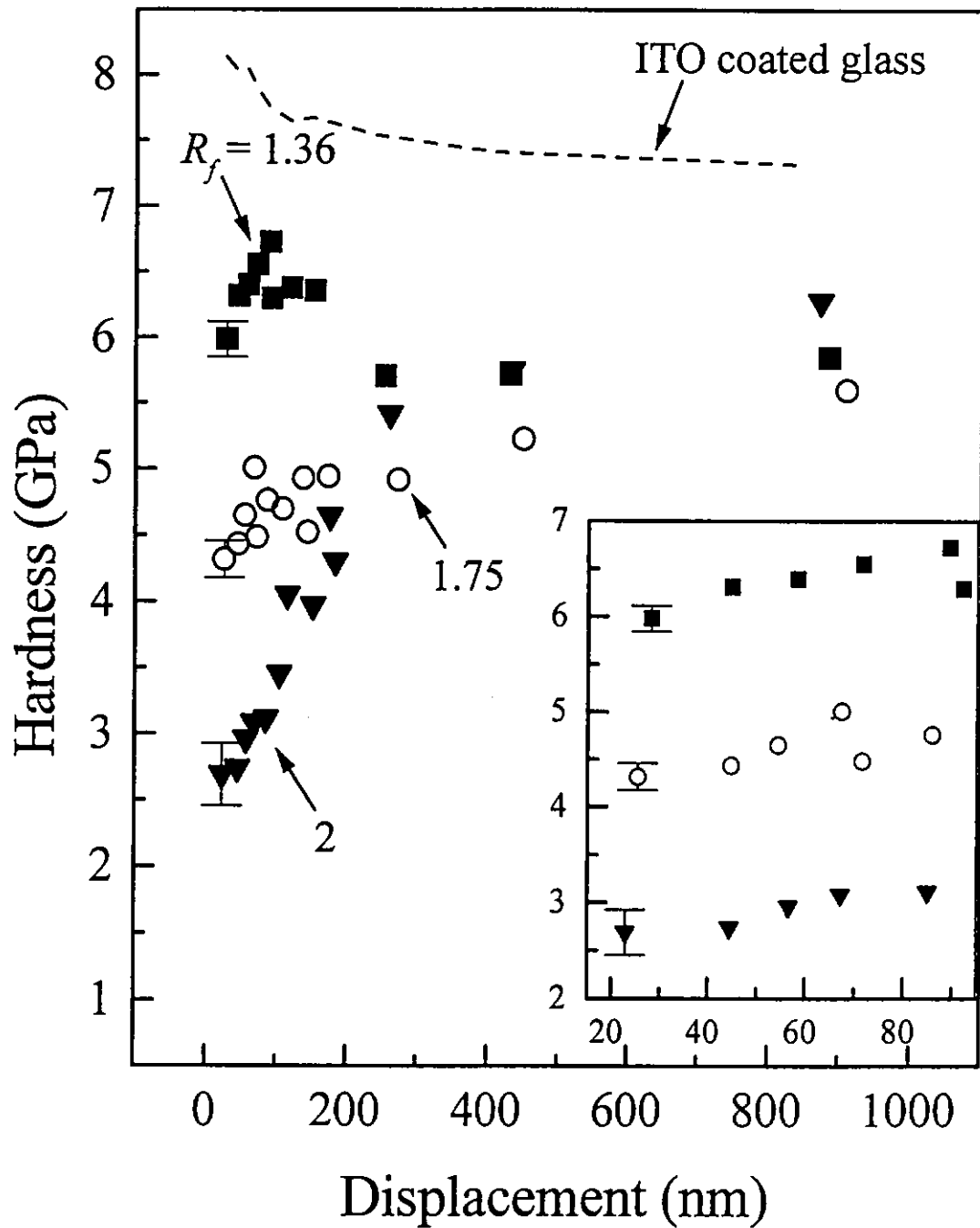


Fig. 6.6(a) Hardness of films deposited by magnetron sputtering film against indentation depth. Films were deposited at fixed pressure =10 mTorr and on unheated substrates. The inset magnifies details below 100 nm.

▼: MS11, $R_f=2$,
 ○: MS12, $R_f=1.75$,
 ■: MS13, $R_f=1.36$.

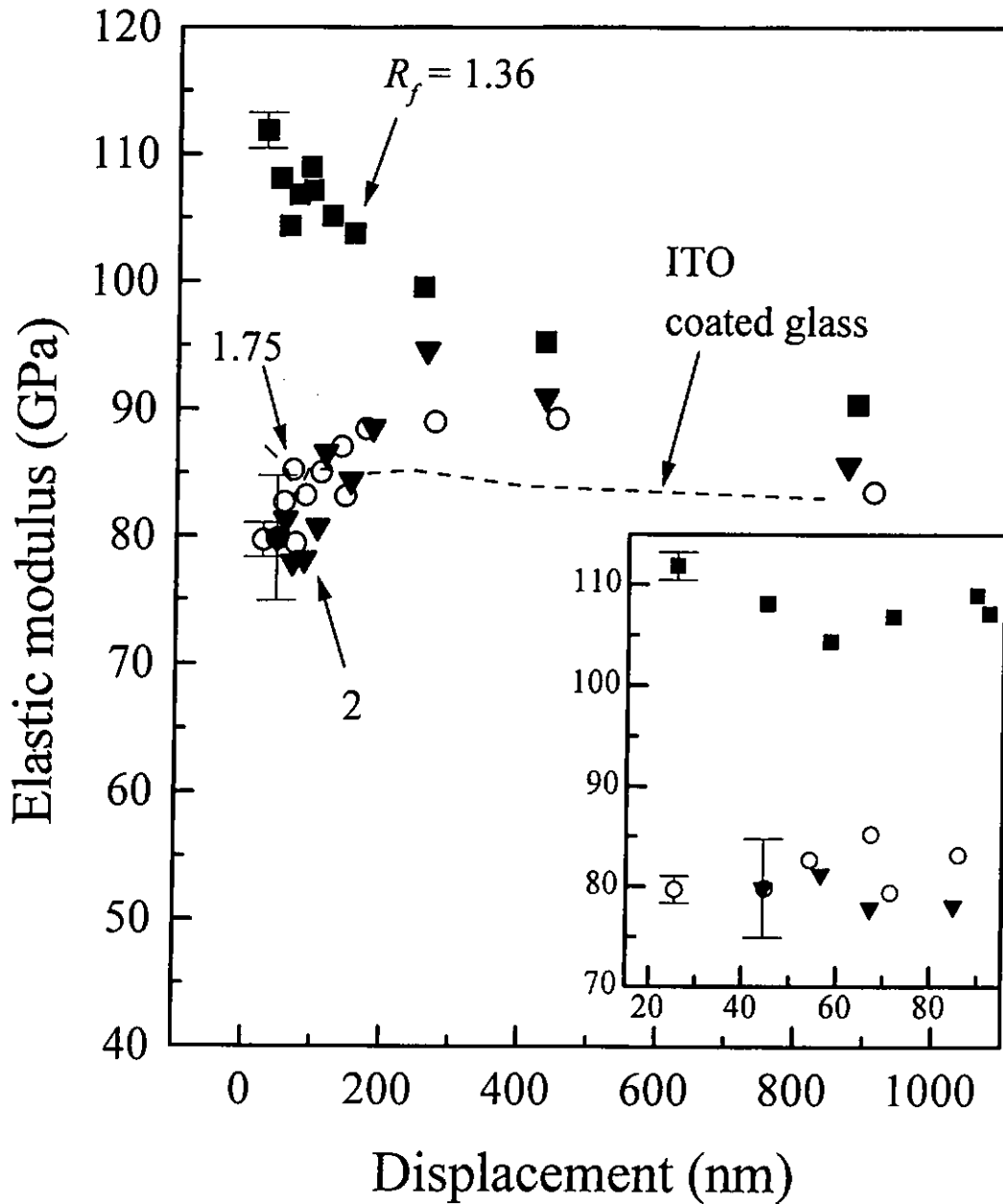


Fig. 6.6(b) Elastic modulus of films deposited by magnetron sputtering film against indentation depth. Films were deposited at fixed pressure =10 mTorr and on unheated substrates. The inset magnifies details below 100 nm.

▼: MS11, $R_f=2$,
 ○: MS12, $R_f=1.75$,
 ■: MS13, $R_f=1.36$.

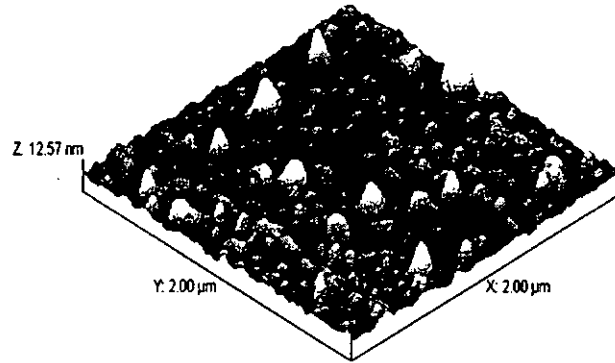


Fig. 6.7(a) MS11, magnetron sputtered sample deposited at $R_f = 2$ on unheated substrate with roughness of 2.08 nm in $(2 \times 2) \mu\text{m}^2$.

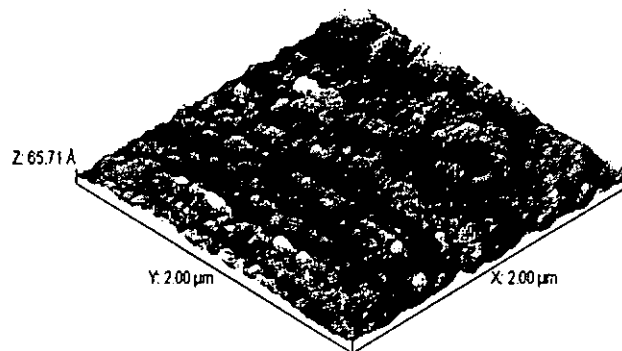


Fig. 6.7(b) MS21, magnetron sputtered sample deposited at $R_f = 2$ and $T_s = 110^\circ\text{C}$ with roughness of 1.14 nm in $(2 \times 2) \mu\text{m}^2$.

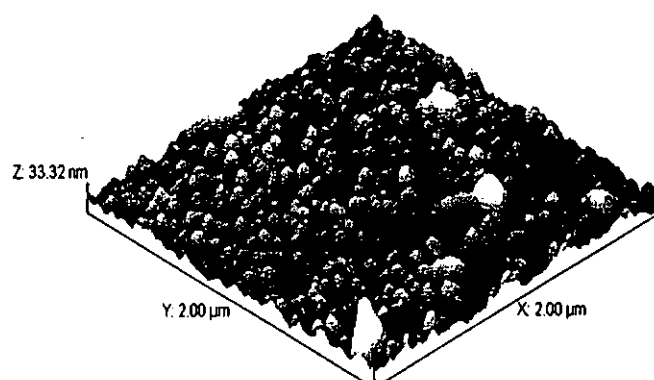


Fig. 6.7(c) MS23, magnetron sputtered sample deposited at $R_f = 2$ and $T_s = 500\text{ }^\circ\text{C}$ with roughness of 5.57 nm in $(2 \times 2)\text{ }\mu\text{m}^2$.

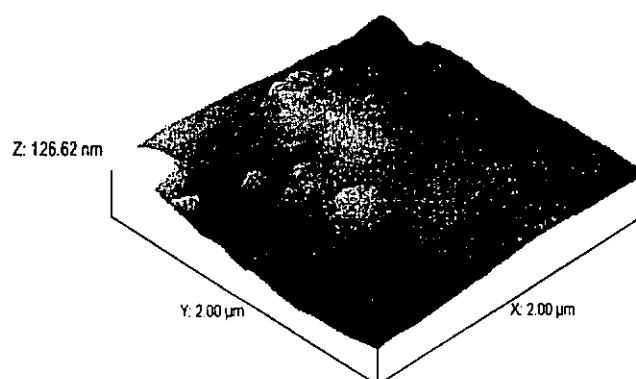


Fig. 6.7(d) TE4, thermally evaporated sample deposited at O_2 partial pressure = 4 mTorr with roughness of 21.07 nm in $(2 \times 2)\text{ }\mu\text{m}^2$.

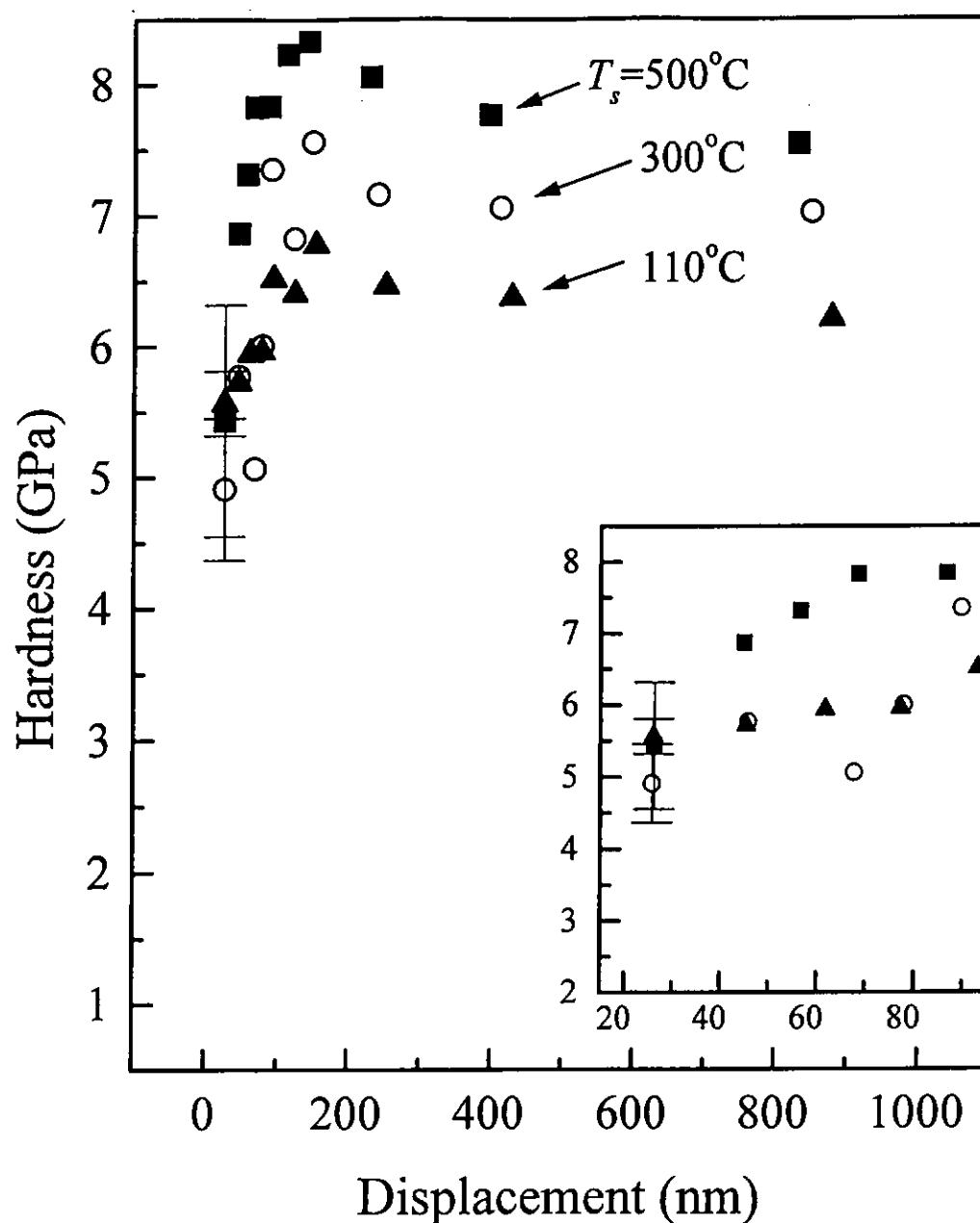


Fig. 6.8(a) Hardness of films deposited by magnetron sputtering against indentation depth. Films were deposited at fixed pressure = 10 mTorr and $R_f = 2$. The inset magnifies details below 100 nm.

▲: MS21, $T_s = 110^\circ\text{C}$,
 ○: MS22, $T_s = 300^\circ\text{C}$,
 ■: MS23, $T_s = 500^\circ\text{C}$.

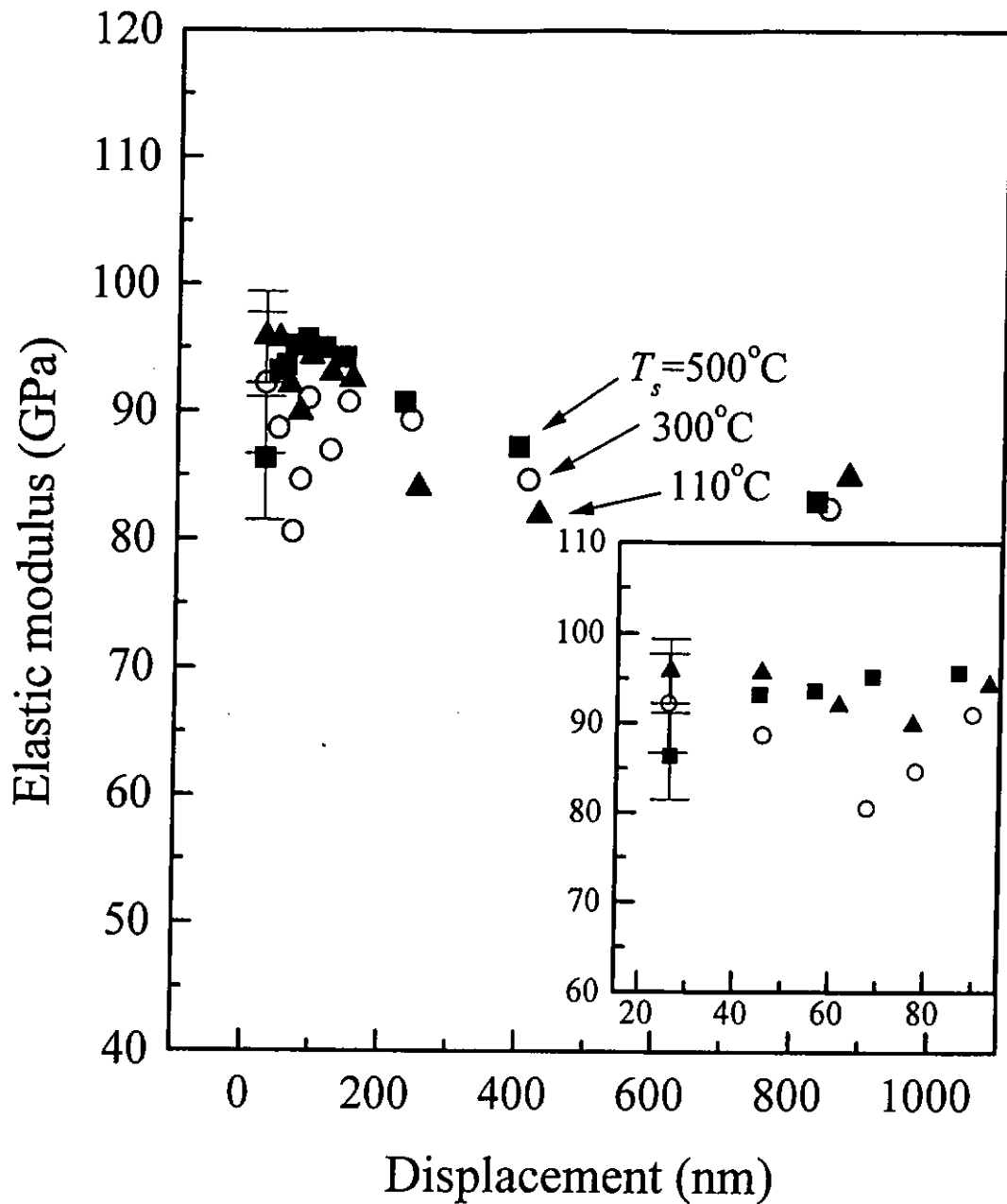


Fig. 6.8(b) Elastic modulus of films deposited by magnetron sputtering against indentation depth. Films were deposited at fixed pressure =10 mTorr and $R_f=2$. The inset magnifies details below 100 nm.

▲: MS21, $T_s = 110^\circ\text{C}$,
 ○: MS22, $T_s = 300^\circ\text{C}$,
 ■: MS23, $T_s = 500^\circ\text{C}$.

6.2.2 Mechanical Properties of Thermally Evaporated Tungsten Oxide Films

Table 6.3 summarizes the results of tungsten oxide films prepared by reactive thermal evaporation on unheated substrates. The ambient pressure was varied from a high vacuum background of 2×10^{-6} Torr (no oxygen admission), up to oxygen partial pressure of 10 mTorr. All the films are transparent, with the O/W ratio close to 3. The XRD data show that all the thermally evaporated tungsten oxide films are amorphous. The film density is lower than that of crystalline WO_3 , and continuously drops with higher O_2 partial pressure. For example, the density of sample TE4 is just 60 % of that of the crystalline state. The AFM image of TE4 shown in Fig. 6.7(d) further verifies that the film is very rough. The statistical roughness is 21.07 nm in an area of $2 \times 2 \mu\text{m}^2$. Such a scenario proposes that the film is extremely porous, while the framework of the film material is very loose. These features are closely related to the deposition mechanism associated with thermal evaporation [Deshpandey and Bunshah 1990]. Tungsten oxide film prepared by thermal evaporation with induced oxygen is therefore intrinsically low dense, differing from a magnetron sputtered process in which species involved in condensation of film are mostly on atomic scale. Associated with such a porous film structure, the hardness and elastic modulus drop significantly from 2.94 to 0.96 GPa and 78.53 to 43.57 GPa respectively, with the O_2 partial pressure increasing from the background pressure of 2×10^{-6} Torr to an oxygen ambient pressure of 10 mTorr (Table 6.3). Furthermore, Fig. 6.9(a) and 6.9(b) illustrate that either hardness or elastic modulus of a sample in this group may exhibit depth dependence, suggesting that the films are nonuniform at the surface.

Sample	O ₂ partial pressure (mTorr)	Thickness (nm)	O/W ratio	Density (g cm ⁻³)	<i>H</i> (GPa)	<i>E</i> (GPa)
TE1	2×10^{-6} Torr (background pressure)	210	3.6	6.9	2.94	78.53
TE3	4	214	3.6	4.7	2.09	51.03
TE4	6	184	3.4	4.5	1.25	39.25
TE5	10	177	3.5	4.1	0.96	43.57

Table 6.3 Hardness and elastic modulus of samples made by thermal evaporation.

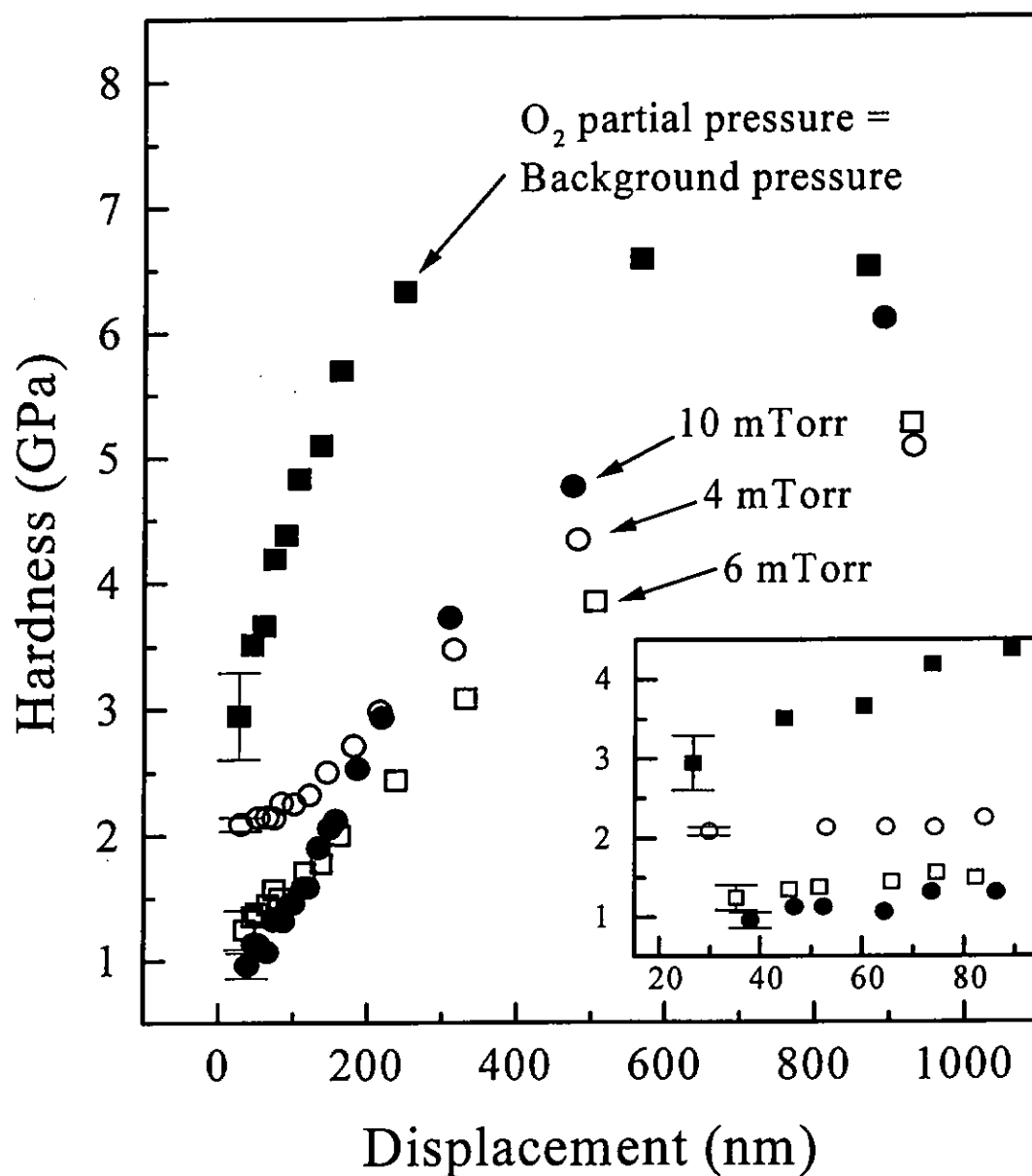


Fig. 6.9(a) Hardness of thermally evaporated films deposited at various oxygen partial pressures against indentation depth. The inset magnifies details below 100 nm.

- : TE1, background pressure of 2×10^{-6} Torr,
- : TE3, 4 mTorr,
- : TE4, 6 mTorr,
- : TE5, 10 mTorr.

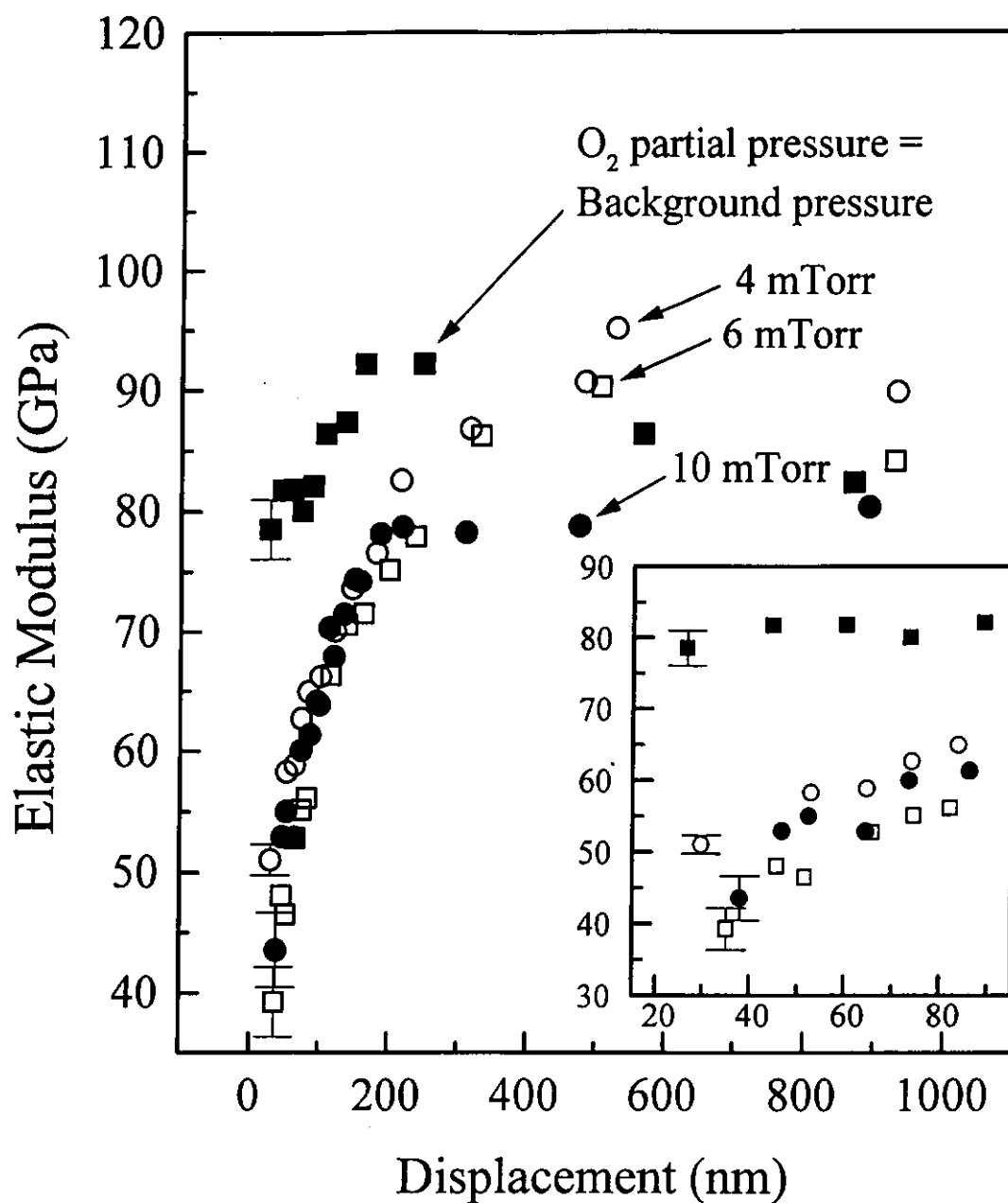


Fig. 6.9(b) Elastic modulus of thermally evaporated films deposited at various oxygen partial pressures against indentation depth. The inset magnifies details below 100 nm.

- : TE1, background pressure of 2×10^{-6} Torr,
- : TE3, 4 mTorr,
- : TE4, 6 mTorr,
- : TE5, 10 mTorr.

Chapter 7

Conclusions

Tungsten oxide is an important inorganic electrochromic material because of its high coloration efficiency. However, the long term stability and fast switching response are also very essential for the material to be applicable in electrochromic devices (ECDs). To date, ECDs available in the market have not satisfied these two basic requirements. In this project, we aimed at getting more understandings of the composition, structure, mechanical and electrochromic properties of WO_3 films deposited by magnetron sputtering and thermal evaporation of various conditions, and the correlation between the film structure and the properties.

For the reactive magnetron sputtering, the flow ratio of oxygen-to-argon (R_f) of the reactant gases and substrate temperature were varied as preparation parameters. For reactive thermal evaporation, the oxygen partial pressure is used as the preparation parameter. W 4f and O 1s and C 1s photoelectron spectra were collected to examine the film composition. When R_f or oxygen partial pressure is sufficiently high, the W 4f spectrum mainly consists of an orbit-spin split, containing W 4f_{7/2} and W 4f_{5/2} lines. W 4f_{7/2} appears around 35.6 eV, and is attributed to WO_3 . The presence of defects generates some O vacancies around tungsten atoms, such that at those local regions the structure is analogous to that of some WO_x phases, with $x < 3$. When R_f used in the magnetron sputtering process is low, the film would become oxygen deficient with O/W ratio below 3. Because of the lack of oxygen, tungsten

atoms in W^V , W^{IV} , W^{III} , W^{II} states and metallic tungsten states are shown to exist in the film according to the XPS analysis of W 4f. XRD and IR data illustrate magnetron-sputtered tungsten oxide films deposited on unheated substrates are amorphous and are constructed of a WO_3 -like random network with a fraction of terminal W=O bonds. R_f is therefore recognized to be an important factor to control the composition of tungsten oxide films. As the R_f optimised, substrate temperature (T_s) is applied during film deposition. The structure of the films is improved by T_s . When substrate temperature increases to 110 °C, the density of small defect decreases, and the concentration of W=O bonds drops. Crystallization is observed when temperature is risen to above 300 °C.

Thermally evaporated tungsten oxide films are amorphous and highly porous. The films also contain oxygen terminal stretching W=O bonds. IR data illustrate the films contain oxygen terminal stretching W=O bonds. The evaporation tungsten oxide condensed as cluster on the substrate.

A magnetron-sputtered film and a thermally evaporated tungsten oxide film were selected for characterizing the electrochromic properties of the films. The samples were driven to experience ten thousand times of c/b cycles. The magnetron-sputtered film was more stable and worked well after 10000 coloring/bleaching (c/b) cycles. However, the thermally evaporated film degraded quickly during the first 1000 cycles proceed. The coloration efficiency of the magnetron-sputtered film is at least two times larger than that of the thermally evaporated film. In fact, the density of the thermally evaporated films is around 4.5 g cm⁻³ but that of magnetron

sputtered film is up to 7 g cm^{-3} . The short lifetime of the thermally evaporated film may be due to its loose structure and low packing density.

Tungsten oxide films prepared by thermal evaporation with induced oxygen are intrinsically amorphous and highly porous. The hardness of thermally evaporated film drops from 2.94 to 0.96 GPa with increasing induced O_2 partial pressure. This shows that the films are soft, simply because the film structure is highly porous. The hardness of the magnetron-sputtered film deposited on heated substrate ($T_s \geq 110^\circ\text{C}$) increases from 2.69 GPa to 5.57 GPa. Such an increase in hardness comes from the removal of defects in the film structure. Further rise in T_s results in crystallization and subsequent growth in grain size. Though with prominent change in crystallinity, it is found that there is no significant change in the O/W ratio, density, hardness and elastic modulus. This suggests that appearance of grains does not affect the response of the crystallinity film samples against nanoindentation.

Another important finding in this study is that ion sputtering of tungsten oxide films for investigating the depth profile information by XPS would alter the original film composition, because oxygen is readily preferentially sputtered, such that the O/W ratio drops significantly. Meanwhile, the sputtering processes render the W^{V} , W^{IV} , W^{III} , W^{II} states and metallic tungsten state to appear in the W 4f photoelectron spectrum. Results of angle-resolved (45° and normal) XPS analysis also show that after experiencing ion irradiation the oxygen content near the sputtered surface is small, further supporting the conjecture that some oxygen is preferentially sputtered by the ion beam.

Publications

Ong, C.W., Wong, A.H.Y. and Choy, C.L. "Nanoindentation study of thermally evaporated and magnetron-sputtered tungsten oxide films" (submitted)

Wong, A.H.Y., Ong, C.W. and Choy, C.L. "Effects of ion beam bombardment on tungsten oxide films" (submitted)

References

- Ageev, V.N. and Ionov, N.I. "Investigation of the chemisorption of oxygen on polycrystalline tungsten by the flash method". *Soviet Physics-Technical Physics*, Vol. 10(11), pp.1614-1620 (1966).
- Akram, H., Kitao, M. and Yamada, S. "Electrochromic properties of rf-sputtered tungstic oxide film prepared from a W metal target". *Journal of Applied Physics*, Vol. 66(9), pp.4364-4367 (1989).
- Azens, A., Granqvist, C.G., Pentjuss, E., Gavrusenoks, J. and Barczynska, J. "Electrochromism of fluorinated and electron-bombarded tungsten oxide films". *Journal of Applied Physics*, Vol. 78 (3), pp.1968-1973 (1995).
- Bechinger, C., Bullock, J.N., Zhang, J.G., Tracy, C.E., Benson, D.K., Deb, S.K. and Branz H.M. "Low-voltage electrochromic device for photovoltaic-powered smart windows". *Journal of Applied Physics*, Vol. 80 (2), pp.1226-1232 (1996).
- Bechinger, C. and Gregg, B.A. "Development of a new self-powered electrochromic device for light modulation without external power supply". *Solar Energy Materials and Solar Cells*, Vol. 54, pp.405-410 (1998).
- Beni, G. and Shay, J. L. "Ion-insertion electrochromic displays". In *Advances in Image Pickup and Display*, Academic Press, New York, pp.83-136 (1982).
- Bohnke, O., Bohnke, C., Donnadiou, A. and Davazoglou, D. "Electrochromic properties of polycrystalline thin films of tungsten trioxide prepared by chemical vapour deposition". *Journal of Applied Electrochemistry*, Vol. 18, pp.447-453 (1988).
- Bohnke, O., Bohnke, C., Robert, G. and Carquille, B. "Electrochromism in WO_3 thin films. I LiClO_4 -propylene carbonate-water electrolyte". *Solid State Ions*, Vol. 6, pp.121-128 (1982).
- Chapman, B. and Mangano, S. "Introduction to sputtering". In Schuegraf, K.K., ed., *Handbook of Thin-Film Deposition Processes and Techniques, Principles, Methods, Equipment and Applications*, Noyes Publications, Park Ridge, pp.291-317 (1988).
- Clemens, B.N., Kung, H., Barnett, S.A. "Structure and strength of multilayers". *Materials Research Bulletin*, Vol. 24, pp.20-26 (1999).
- Colton, R.J., Guzman, A.M. and Rabalais, J.W. "Electrochromism in some thin-film transition-metal oxides characterized by x-ray electron spectroscopy". *Journal of Applied Physics*, Vol. 49(1), pp.409-416 (1978).
- Davazoglou, D. and Donnadiou, A. "Structure and optical properties of WO_3 thin films prepared by chemical vapour deposition". *Thin Solid Films*, Vol. 147, pp.131-142 (1987).

- Davazoglou, D. and Donnadieu, A. "Electrochromism in polycrystalline WO_3 thin films prepared by chemical vapour deposition at high temperature". *Thin Solid Films*, Vol. 164, pp.369-374 (1988).
- Deb, S.K. "A novel electrophotographic system". *Applied Optics Supplement*, Vol. 3, pp.192-195 (1969).
- Delichere, P., Falaras, P., Forment, M., Hugot-le Goff, A. and Agius, B. "Electrochromism in anodic WO_3 films I: preparation and physicochemical properties of films in the virgin and coloured states". *Thin Solid Films*, Vol. 161, pp.35-46 (1988).
- Depero, L.E., Groppelli, L., Natali-Sora, I., Sangaletti, L., Sberveglieri, G. and Tondello, E. "Structural studies of tungsten-titanium oxide thin films". *Journal of Solid State Chemistry*, Vol. 121, pp.379-387 (1996).
- Deshpandey, C.V. and Bunshah, R.F. "The activated reactive evaporation (ARE) process". In Rossnagel, S.M., Cuomo, J.J. and Westwood, W.D., eds., *Handbooks of Plasma Processing Technology Fundamentals, Etching, Deposition, and Surface Interactions*, Noyes Publications, Park Ridge, pp.370-383 (1990).
- Dickens, P.G. and Whittingham, M. S. "The tungsten bronzes and related compounds". *Quarterly Reviews Chemical Society*, Vol. 22, pp.30-44 (1968).
- Faughana, B.W., Crandall, R.S. and Heyman, P.M. "Electrochromism in WO_3 amorphous films". *RCA Review*, Vol. 36, pp.177-197 (1975).
- Faughnan, B.W. and Crandall, R.S. "Electrochromic displays based on WO_3 ". In Pankove, J.I. ed., *Topic in Applied Physics Volume 40: Display Devices*, Springer-Verlag, New York, pp.181-211 (1980).
- Feldman, L.C. and Mayer, J.W. "X-ray Photoelectron Spectroscopy (XPS)". In *Fundamentals of Surface and Thin Film Analysis*, Elsevier Science Publishing Co., Inc., New York, pp.213-231 (1986).
- Feldman, L.C. and Mayer, J.W. "Sputter Depth Profiles and Secondary Ion Mass Spectrometry". In *Fundamentals of Surface and Thin Film Analysis*, Elsevier Science Publishing Co., Inc., New York, pp.89-91 (1986).
- Fraser, D.B. and Westwood, W.D. "Techniques for IC processing". In Rossnagel, S.M., Cuomo, J.J. and Westwood, W.D., eds., *Handbooks of Plasma Processing Technology Fundamentals, Etching, Deposition, and Surface Interactions*, Noyes Publications, Park Ridge, pp.2-12 (1990).
- Gerand, B., Nowogrocki, G. and Figlarz, M. "A new tungsten trioxide hydrate, $\text{WO}_3 \cdot 1/3\text{H}_2\text{O}$; preparation, characterization, and crystallographic study". *Journal of Solid State Chemistry*, Vol. 38, pp.312-320 (1981).
- Granqvist, C.G. "Electrochromism and smart window design". *Solid State Ionics*, Vol. 53, pp.479-489 (1992).

- Granqvist, C.G. *Handbook of Inorganic Electrochromic Materials*, Elsevier Science B.V., The Netherlands, 633pp (1995).
- Greef, R., Peat, R., Peter, L.M., Pletcher, D. and Robinson, J. "Chapter 6 Potential sweep techniques and cyclic voltammetry". In *Instrusmental Methods in Electrochemistry*, Ellis Horwood Limited, West Sussex, England, pp.178-228 (1985).
- Greenberg, C.B. "Invited Review Optical switchable thin films: a review". *Thin Solid Films*, Vol. 251, pp.81-93 (1994).
- Hashimoto, S., Matsuoka, H., Kagechika, H., Susa, M., and Goto, K. S. "Degradation of electrochromic amorphous WO_3 film in lithium-salt electrolyte". *Journal of Electrochemical Society*, Vol. 137 (4), pp.1300-1304 (1990).
- Hashimoto, S. and Matsuoka, H. "Lifetime of electrochromism of amorphous WO_3 - TiO_2 Films". *Journal of Electrochemical Society*, Vol. 138 (8), pp.2403-2408 (1991).
- Kamimori, T., Nagai, J. and Mizuhashi, M. "Electrochromic devices for transmissive and reflective light control". *Solar Energy Materials* Vol. 16, pp.27-38 (1987).
- Kaneko, H., Nishimoto, S., Miyake, K., and Suedomi, N. "Physical and electrochemichromic properties of rf sputtered tungsten oxide films". *Journal of Applied Physics*, Vol. 59 (7), pp.2526-2534 (1986).
- Matsuhiro, K. and Masuda, Y. "Transmissive electrochromic display using a porous crystalline WO_3 counter electrode". *Proceedings of the SID*, Vol. 21/2, pp.101-105 (1980).
- Monk, P.M.S. and Chester, S.L. "Electro-deposition of films of electrochromic tungsten oxide containing additional metal oxides". *Electrochimica Acta*, Vol. 38(11), pp.1521-1526 (1993).
- Monk, P.M.S., Mortimer R.J. and Rosseinsky D.R. *Electrochromism Fundamentals and Application*, VCH Verlagsgesellschaft mbH, Weinheim, 216pp (1995).
- Monk, P.M.S., Partridge, R.D., Janes, R. and Parker, M.J. "Electrochromic tungsten oxide: Doping with two or three other metal oxides". *Journal of Materials Chemistry*, Vol. 4(7), pp.1071-1074 (1994).
- Morita, H. and Washida, H. "Electrochromism of atmospheric evaporated tungsten oxide films (AETOF)". *Japanese Journal of Applied Physics*, Vol. 23(6), pp.754-759 (1984).
- Moulder, J.F., Stickle, W.F., Sobol, P.E. and Bomben, K.D. In Chastain, J. ed., *Handbook of X-ray Photoelectron Spectroscopy*, Perkin-Elmer Corp., Minnnesota, pp.213-248 (1992).
- Nagai, J., Kamimori, T. and Mizuhashi, M. "Electrochromism in amorphous lithium tungsten oxide films". *Solar Energy Materials*, Vol. 13, pp.279-295 (1986).

- Nyquist, R.A. and Kagel, R.O. *Infrared Spectra of Inorganic Compounds (3800-45cm⁻¹)*, Academic Press, Inc. Orlando, 495pp (1971).
- Oliver, W.C. and Pharr, G.M. "An improved technique for determining hardness and elastic modulus using load and displacement sensing indentation experiments". *Journal of Materials Research*, Vol. 7 (6), pp.1564-1583 (1992).
- Ptushinskii, Yu.G. and Chuikov, B.A. "Mass spectrometric investigation of the interaction of oxygen with a tungsten surface". *Surface Science*, Vol. 6, pp.42-56 (1967).
- Reichman, B. and Bard, A.J. "The electrochromic process at WO₃ electrodes prepared by vacuum evaporation and anodic oxidation of W". *Journal of Electrochemical Society: Electrochemical Science and Technology*, Vol. 126 (4), pp.583-591 (1979).
- Sabbatini, L., Sherwood, P.M.A. and Zamboni, P.G. "Characterization of films formed on tungsten electrodes in molten nitrates using electrochemical and X-ray photoelectron spectroscopic studies". *Journal of Electrochemical Society: Electrochemical Science and Technology*, Vol. 130 (11), pp.2199-2205 (1983).
- Salje, E. "Lattice dynamics of WO₃". *Acta Cryst.*, Vol. A31, pp.360-363 (1975).
- Schissel, P.O. and Trulson, O.C. "Mass-spectrometric study of the oxidation of tungsten". *The Journal of Chemical Physics*, Vol. 43(2), pp.737-743 (1965).
- Schlotter, P. "High contrast electrochromic tungsten oxide layers". *Solar Energy Materials*, Vol. 16, pp.39-46 (1987).
- Shen, P.K. and Tseung, A.C.C. "Study of electrodeposited tungsten trioxide thin films". *Journal of Materials Chemistry*, Vol. 2(11), pp.1141-1147 (1992).
- Shigesato, Y., Hayashi, Y., Masui, A. and Haranou, T. "The structural changes of indium-tin oxide and α -WO₃ films by introducing water to the deposition process". *Japanese Journal of Applied Physics*, Vol. 30 (4), pp.814-819 (1991).
- Shigesato, Y., Murayama, A., Kamimori, T. and Matsui, K. "Characterization of evaporated amorphous WO₃ films by Raman and FTIR spectroscopies". *Applied Surface Science*, Vol. 33/34, pp.804-811 (1988).
- Shirley, D.A. "High-resolution x-ray photoemission spectrum of the valence bands of gold". *Physical Review B*, Vol. 5, pp.4709-4714 (1972).
- Smith, B.C. *Fundamentals of Fourier Transform Infrared Spectroscopy*, CRC Press, Inc., the United States of America, 202pp (1996).
- Socrates, G. "Hydroxyl Group Compounds: O-H Group". In *Infrared Characteristic Group Frequencies*, John Wiley & Sons Ltd., Great Britain, pp.45-47 (1980).

Yamanaka, K. "Electrodeposited films from aqueous tungstic acid-hydrogen peroxide solutions for electrochromic display devices". *Japanese Journal of Applied Physics*, Vol. 26(11), pp.1884-1890 (1987).

Yoshiike, N. and Kondo, S. "Electrochemical properties of $\text{WO}_3 \cdot x(\text{H}_2\text{O})$ I. The influences of water adsorption and hydroxylation". *Journal of Electrochemical Society: Solid-State Science and Technology*, Vol. 130 (11), pp.2283-2287 (1983).

Zhong, Q., Dahn, J.R. and Colbow, K. "Lithium intercalation into WO_3 and the phase diagram of Li_xWO_3 ". *Physical Review B*, Vol. 46 (4), pp.2554-2560 (1992)^a.

Zhong, Q., Dahn, J.R. and Colbow, K. "Dependence of the intercalation of Li in WO_3 on the preparation of the WO_3 host". *Journal of Electrochemical Society*, Vol. 139 (4), pp.2406-2409 (1992)^b.